# Density functional and spin fluctuation theory based study for iron-based and organic superconductors

（密度汎関数理論およびスピンゆらぎの理論に基づく鉄系・有機系超伝導体の研究）

SHIMIZU Makoto

Division of Interdisciplinary Science
Okayama University

A thesis submitted for the degree of
Doctor of Philosophy in Science

March 2023

Abstract

In this thesis, iron-based and organic superconductors are studied based on density functional theory (DFT) and spin fluctuation theory. These superconducting materials belong to unconventional superconductors where strong electronic correlations play an important role. Such superconductors show varied physical properties like spin ordering, charge ordering, Mott insulating, anisotropic superconducting order parameters and so on. Our aim in this study is to explain and predict such properties in the materials.

The first topic is superconducting dome in an electron doped FeSe intercalate both from itinerant electron and localized moment perspectives. The van-der-Waals gap of iron chalcogenide superconductors can be intercalated with a variety of inorganic and organic compounds that modify the electron doping level of the iron layers. Parts of these electron-doped FeSe-based materials show high-$T_c$ superconductivity, for instance, $T_c = 55$ K in $Li_{0.36}(NH_3)_yFe_2Se_2$ under pressure and $T_c = 32$ K in $Rb_xFe_{2-y}Se_2$. The mechanism of such high-$T_c$ superconductivity in electron-doped FeSe-based superconductors has been controversial; whether it is spin fluctuations, nematic fluctuations or combinations of them. It is not obvious whether spin fluctuations are developed since absence of hole pockets which are essential for the common spin fluctuations in iron-based superconductors is reported. In $Li_x(C_3N_2H_{10})_{0.37}FeSe$, a dome in the superconducting transition temperature $T_c$ has been reported to occur in the doping range of $x = 0.06$ to $x = 0.68$. $T_c$ increases as $x$ increases in the low doping region ($x \leq 0.37$) and reaches $T_c = 46$ K at $x = 0.37$. On the other hand, $T_c$ decreases in the high doping region ($x \geq 0.37$). We search the microscopic mechanisms of the change of $T_c$ both from itinerant electron and localized moment perspectives. Recent nuclear magnetic resonance (NMR) experiments for FeSe intercalates support the spin fluctuations scenario. It is meaningful to investigate superconductivity mediated by spin fluctuations in the wide range of the electron doping in this material. In this study, we simplify the FeSe intercalate to $Li_x(C_3N_2H_{10})_{0.5}FeSe$. We have studied the electronic structure as a function of doping in the range $0.06 \leq x \leq 0.68$ by performing a series of density functional theory (DFT) calculations. We have analyzed the superconductivity both from itinerant electron and localized moment perspectives. In the itinerant electron perspective, we have constructed five-band tight-binding models based on the DFT electronic structures and

calculated spin susceptibility and superconducting instability within the random phase approximation (RPA). In the localized moment perspective, we have mapped the DFT energy to Heisenberg models, and we have analyzed changes of the exchange couplings. We have made the analysis for a dense mesh of doping level $x$ and discussed changes of superconductivity. We have studied the electronic structure as a function of doping in the range $0.06 \leq x \leq 0.68$ by performing a series of density functional theory (DFT) calculations. We have analyzed the superconductivity both from itinerant electron and localized moment perspectives. In the itinerant electron perspective, we have constructed five-band tight-binding models based on the DFT electronic structures and calculated spin susceptibility and superconducting instability within the random phase approximation (RPA). In the localized moment perspective, we have mapped the DFT energy to Heisenberg models, and we have analyzed changes of the exchange couplings We have made the analysis for a dense mesh of doping level $x$ and discussed changes of superconductivity. As results, we reveal the following points.

1. Sign-changing $s$-wave is enhanced by spin fluctuations on the low doping side.
2. The growing $T_{\rm c}$ on the low doping side is understood with growing Fermi surfaces and densities of states at the Fermi level.
3. Suppression of $T_{\rm c}$ at the high doping side is not captured with the itinerant electron analysis within RPA.
4. The stripe type antiferromagnetic fluctuations are destabilized toward bicollinear antiferromagnetic, which explains why $T_{\rm c}$ decreases on the high-doping side.

The second topic is superconducting symmetry of $\kappa$-type BEDT-TTF charge transfer salts. BEDT-TTF charge transfer salts, which is quasi two-dimensional materials composed of bis(ethylenedithio)tetrathiafulvalene abbreviated as BEDT-TTF or ET have variations of molecular structure like $\alpha$-, $\beta$-, $\gamma$-, $\kappa$- and $\theta$-types. Especially, $\kappa$-type has the largest number of superconducting materials with the $T_{\rm c}$ from a few Kelvins to a dozen Kelvin. Antiferromagnetic ordering states exists next to the superconducting states, therefore antiferromagnetic spin fluctuations are suggested as mechanism of the superconductivity. Spin fluctuation theory suggested $d_{x^2-y^2}$-wave gap function, and experiments agreed with it in the initial studies for the charge transfer salts. However, recent detailed experimental studies suggest other possibilities of gap functions like anisotropic $s$-wave, sign changing $s$-wave, and $s_{\pm}+d_{x^2-y^2}$-wave. Theoretical studies sug-

gest that such variations of gap functions result from variations of hopping transfers in molecular models corresponding to the materials. Identification of gap functions has not been achieved. It is necessary to investigate the electronic structures with considering the spin fluctuations in specific models for the materials. In this study, we apply fluctuation exchange (FLEX) approximation to specific models and fully solve the linearized Eliashberg equation. As results, we reveal the following points.

1. An anisotropic $s$-wave gap functions is obtained in $X = (\mathrm{ET})_2\mathrm{CuN}(\mathrm{CN})_2\mathrm{Br}$, and a $s_\pm + d_{x^2-y^2}$-wave gap functions is obtained in $X = (\mathrm{ET})_2\mathrm{Cu}(\mathrm{NCS})_2$. This difference results from in-plane anisotropy of the hopping parameters.
2. In the low-$T_\mathrm{c}$ group, anisotropic $s$-wave superconductivity is overestimated within FLEX. This result implies that factors, for example, intra-dimer inter-molecule Coulomb interactions not considered in the FLEX should play an important role in the group.

# Contents

# Chapter 1

# Introduction to superconductivity

## 1.1 Discovery of superconductivity

The first discovery of superconductivity is on mercury by H. Kamerlingh Onnes in 1919 [1]. At the time, he pursued lower temperature around a few Kelvins to verify the Van der Waals equation at low temperature. It was also controversial whether electrical conductivity is enhanced or suppressed at low temperature at the time. He finally succeeded in the first liquefaction of helium in 1908, and in 1911, he measured the electrical conductivity of pure metals at low temperature. Surprisingly, the electrical resistivity of mercury suddenly vanished at 4.2K. He found the superconducting phase transition.

## 1.2 Properties of superconductivity

*Zero electrical resistance* — Electrical resistance of superconductors is exactly zero, which means superconductors show infinite electrical conductivity. When we apply electrical current to a superconducting ring, the current flows persistently (persistent current) while the current decays in a metal ring because of the finite resistivity.

*Jump of specific heat* — When we measure it as temperature is lowered, the specific heat jumps at the temperature where the state changes from normal to superconducting. Therefore, the change from normal state to superconducting state is a second-order phase transition. We call the temperature where the superconducting transition occurs superconducting critical temperature, $T_c$.

*Meissner effect* — The most fundamental phenomenon of superconductivity is the Meissner effect, which is perfect diamagnetism, expulsion of a magnetic field from a

superconductor. This is evidence that superconductivity is a macroscopic quantum phenomenon not just zero resistivity. The perfect diamagnetism is realized in the bulk. The magnetic field can penetrate the superconductor only up to $\lambda \sim$100Å. This length $\lambda$ is a characteristic parameter, called the London penetration depth.

*Critical field* — When the external magnetic field $H$ larger than a critical value, $H_{\rm c}$, is applied to a superconductor, the superconducting state breaks down, and the magnetic field penetrates the sample. The field $H_{\rm c}$ is called the critical field. The critical field $H_{\rm c}(T)$ decreases as temperature $T$ increases, and it is zero at $T = T_{\rm c}$. It is possible to classify superconductors with the critical field. Type I superconductors show one critical field, $H_{\rm c}$. When $H < H_{\rm c}$ is applied, the whole field is excluded. When $H > H_{\rm c}$ is applied, the field penetrates and the superconducting state is completely broken. Typical type I superconductors are simple substance superconductors like Al, Sn, Hg, Pb and so on. On the other hand, Type II superconductors show two critical fields, $H_{\rm c1}$ and $H_{\rm c2}$. When a small magnetic field is applied ($H_{\rm c1} < H < H_{\rm c2}$), a part of the external field penetrates. When $H > H_{\rm c2}$, the whole field penetrates, and the superconducting state is broken.

*Isotope effect* — $T_{\rm c}$ sometimes changes when an element of the superconductor is replaced by its isotope. If the weight $M$ dependence of the critical temperature $T_{\rm c}$ is given by

$$T_{\rm c} \propto M^{-\beta}, \tag{1.1}$$

typical superconductors show $\beta \sim 0.5$. The fact that $T_{\rm c}$ depends on $M$ implies that the motion of atoms, which means lattice vibrations play an important role in one kind of superconductivity.

*Energy gap* — In the excitation of quasiparticles in superconductors around the Fermi level, there is a gap, an energy range where the density of states of quasiparticles is zero. The magnitude of the gap $\Delta$ is small compared to the band scale. It grows as temperature decreases. Within the BCS theory, it is estimated with the critical temperature as

$$\Delta(T = 0) = 1.764 k_{\rm B} T_{\rm c} \tag{1.2}$$

where $k_{\rm B}$ is the Boltzman constant.

*Josephson effect* — Cooper pairs are condensed and in coherent states, and thus the wave functions of the cooper pairs have a universal phase in a superconductor. The Josephson effect is a fundamental effect by such a coherent phase. Let us consider a junction called a Josephson junction, which is constructed with two superconductors and

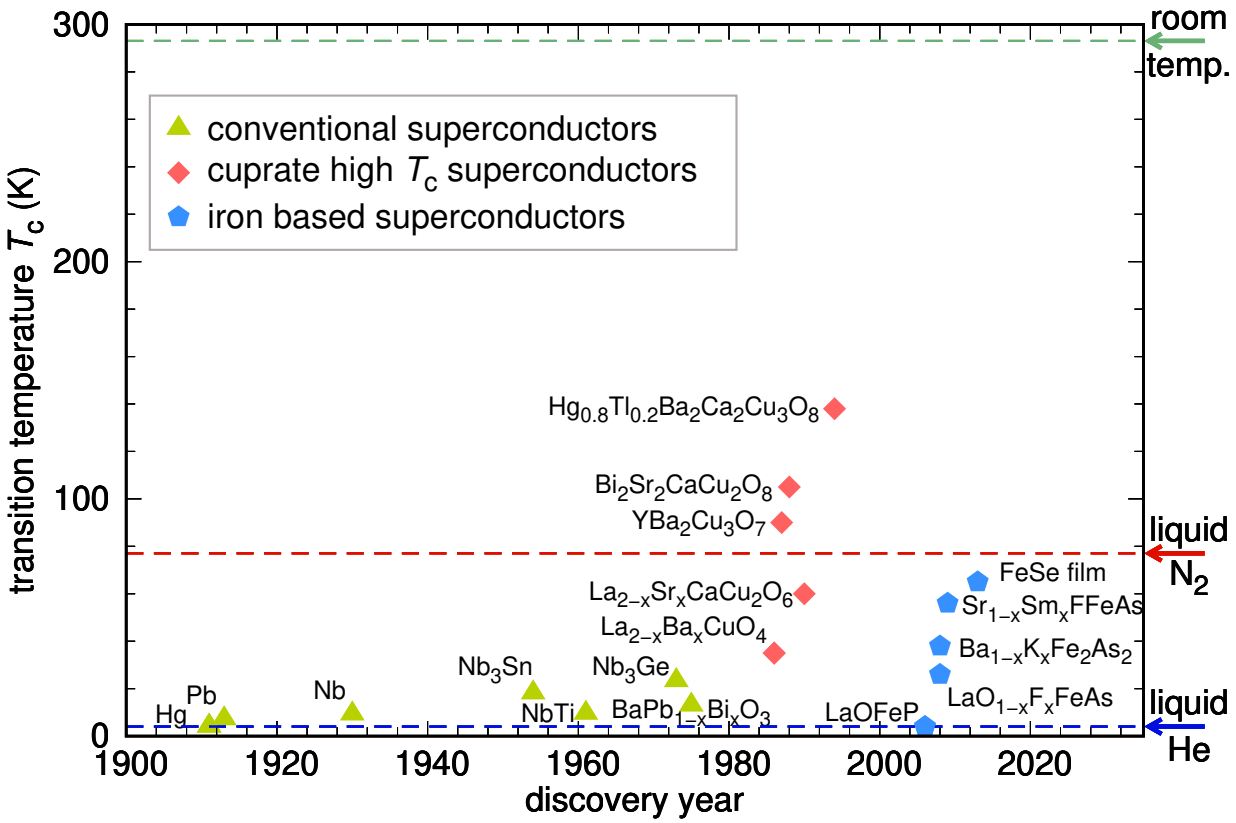


Fig.1.1: Timeline of superconductivity from 1990 to 2020. Values of the transition temperature are from Ref. [1, 2]

a thin film of insulator between them. Electrons can flow through the insulating film by way of quantum tunneling. The electric current depends on the phase difference of the superconductors.

*Exploration of superconductors* — Fig 1.1 is the timeline of superconductors. In studies covering a century, superconductivity was discovered in many materials. Mainly from the end of the 1970s, new families of superconductors are discovered. They are heavy fermion superconductors, which are compounds of rare-earth or actinide ions, cuprate superconductors, which are made of layers of copper oxides ($CuO_2$), and iron-based superconductors, which are compounds of iron.

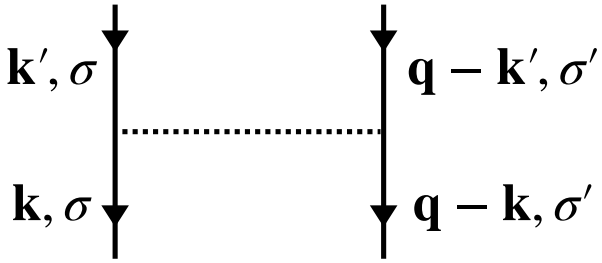


Fig.1.2: Diagram of electron-electron interaction. It shows a electron scattering, $\boldsymbol{k}' \to \boldsymbol{k}$. When we put the center $\boldsymbol{q}$, scattering of the other electron is $\boldsymbol{q} - \boldsymbol{k}' \to \boldsymbol{q} - \boldsymbol{k}$.

## 1.3 BCS theory

In this section, we give an overview of BCS theory [3]. The Hamiltonian of an electron system with correlations is given by

$$H = \sum_{\boldsymbol{k}} \sum_{\sigma} \xi(\boldsymbol{k}) c^{\dagger}_{\boldsymbol{k},\sigma} c_{\boldsymbol{k},\sigma} + \frac{1}{2} \sum_{\boldsymbol{r},\boldsymbol{r}'} V(\boldsymbol{r} - \boldsymbol{r}') n(\boldsymbol{r}) n(\boldsymbol{r}') \tag{1.3}$$

where $\xi(\boldsymbol{k}) = \epsilon(\boldsymbol{k}) - \mu$ is the kinetic energy including the chemical potential, $V(\boldsymbol{r} - \boldsymbol{r}')$ is the interaction between two electrons. In BCS theory, an attractive interaction $V < 0$ is assumed. $c^{\dagger}_{\boldsymbol{k},\sigma}$ and $c_{\boldsymbol{k},\sigma}$ are creation and annihilation operators for an electron with wave vector $\boldsymbol{k}$ and spin $\sigma$, and $n(\boldsymbol{r}) = \sum_{\sigma} c^{\dagger}_{\boldsymbol{r},\sigma} c_{\boldsymbol{r},\sigma}$ is the electron number operator. By taking the Fourier transform, we obtain

$$H = \sum_{\boldsymbol{k}} \sum_{\sigma} \xi(\boldsymbol{k}) c^{\dagger}_{\boldsymbol{k},\sigma} c_{\boldsymbol{k},\sigma} + \frac{1}{2} \sum_{\boldsymbol{k},\boldsymbol{k}',\boldsymbol{q}} \sum_{\sigma,\sigma'} V(\boldsymbol{k} - \boldsymbol{k}') c^{\dagger}_{\boldsymbol{k},\sigma} c^{\dagger}_{\boldsymbol{q}-\boldsymbol{k},\sigma'} c_{\boldsymbol{q}-\boldsymbol{k}',\sigma'} c_{\boldsymbol{k}',\sigma} \tag{1.4}$$

where we chose $\boldsymbol{q}$ as the center of the two electrons (see also Fig. 1.2). We consider the more general interaction, $V(\boldsymbol{k}, \boldsymbol{k}')$, here.

$$H = \sum_{\boldsymbol{k}} \sum_{\sigma} \xi(\boldsymbol{k}) c^{\dagger}_{\boldsymbol{k},\sigma} c_{\boldsymbol{k},\sigma} + \frac{1}{2} \sum_{\boldsymbol{k},\boldsymbol{k}',\boldsymbol{q}} \sum_{\sigma,\sigma'} V(\boldsymbol{k}, \boldsymbol{k}') c^{\dagger}_{\boldsymbol{k},\sigma} c^{\dagger}_{\boldsymbol{q}-\boldsymbol{k},\sigma'} c_{\boldsymbol{q}-\boldsymbol{k}',\sigma'} c_{\boldsymbol{k}',\sigma} \tag{1.5}$$

The essence of BCS theory is to take a mean field approximation for correlations,

$\left\langle c^\dagger_{\boldsymbol{k},\sigma} c^\dagger_{\boldsymbol{q}-\boldsymbol{k},\sigma'} \right\rangle$ and $\langle c_{\boldsymbol{q}-\boldsymbol{k}',\sigma'} c_{\boldsymbol{k}',\sigma} \rangle$. Then, the Hamiltonian becomes

$$\begin{aligned} H =& \sum_{\boldsymbol{k}} \sum_{\sigma} \xi(\boldsymbol{k}) c^\dagger_{\boldsymbol{k},\sigma} c_{\boldsymbol{k},\sigma} \\ &+ \frac{1}{2} \sum_{\boldsymbol{k},\boldsymbol{k}',\boldsymbol{q}} \sum_{\sigma,\sigma'} V(\boldsymbol{k},\boldsymbol{k}') \left[ c^\dagger_{\boldsymbol{k},\sigma} c^\dagger_{\boldsymbol{q}-\boldsymbol{k},\sigma'} \langle c_{\boldsymbol{q}-\boldsymbol{k}',\sigma'} c_{\boldsymbol{k}',\sigma} \rangle + \left\langle c^\dagger_{\boldsymbol{k},\sigma} c^\dagger_{\boldsymbol{q}-\boldsymbol{k},\sigma'} \right\rangle c_{\boldsymbol{q}-\boldsymbol{k}',\sigma'} c_{\boldsymbol{k}',\sigma} \right] \\ &- \frac{1}{2} \sum_{\boldsymbol{k},\boldsymbol{k}',\boldsymbol{q}} \sum_{\sigma,\sigma'} V(\boldsymbol{k},\boldsymbol{k}') \left\langle c^\dagger_{\boldsymbol{k},\sigma} c^\dagger_{\boldsymbol{q}-\boldsymbol{k},\sigma'} \right\rangle \langle c_{\boldsymbol{q}-\boldsymbol{k}',\sigma'} c_{\boldsymbol{k}',\sigma} \rangle . \end{aligned} \tag{1.6}$$

In BCS theory, we apply three more assumption in addition to the mean field approximation.

1. Center-of-mass momentum of Cooper pair is zero. ($\boldsymbol{q} = \boldsymbol{0}$)
2. Total spin of Cooper pair is zero. (Spin singlet)
3. Symmetry of Cooper pair is isotropic. ($s$-wave)

The theory with the three assumptions is called BCS theory in a narrow sense, and superconductors which are subject to the narrow BCS theory are called "BCS-type" or "conventional" superconductors. On the other hand, superconductors which are not subject to the three assumptions are called "unconventional" or "exotic" superconductors.

We apply the first approximation to the Hamiltonian (1.6). The term with $\boldsymbol{q} = 0$ remains, and we obtain

$$\begin{aligned} H =& \sum_{\boldsymbol{k}} \sum_{\sigma} \xi(\boldsymbol{k}) c^\dagger_{\boldsymbol{k},\sigma} c_{\boldsymbol{k},\sigma} \\ &+ \frac{1}{2} \sum_{\boldsymbol{k},\boldsymbol{k}'} \sum_{\sigma,\sigma'} V(\boldsymbol{k},\boldsymbol{k}') \left[ c^\dagger_{\boldsymbol{k},\sigma} c^\dagger_{-\boldsymbol{k},\sigma'} \langle c_{-\boldsymbol{k}',\sigma'} c_{\boldsymbol{k}',\sigma} \rangle + \left\langle c^\dagger_{\boldsymbol{k},\sigma} c^\dagger_{-\boldsymbol{k},\sigma'} \right\rangle c_{-\boldsymbol{k}',\sigma'} c_{\boldsymbol{k}',\sigma} \right] \\ &- \frac{1}{2} \sum_{\boldsymbol{k},\boldsymbol{k}'} \sum_{\sigma,\sigma'} V(\boldsymbol{k},\boldsymbol{k}') \left\langle c^\dagger_{\boldsymbol{k},\sigma} c^\dagger_{-\boldsymbol{k},\sigma'} \right\rangle \langle c_{-\boldsymbol{k}',\sigma'} c_{\boldsymbol{k}',\sigma} \rangle \\ =& \sum_{\boldsymbol{k}} \sum_{\sigma} \xi(\boldsymbol{k}) c^\dagger_{\boldsymbol{k},\sigma} c_{\boldsymbol{k},\sigma} \\ &+ \frac{1}{2} \sum_{\boldsymbol{k},\boldsymbol{k}'} \sum_{\sigma,\sigma'} \left[ \Delta_{\sigma\sigma'}(\boldsymbol{k}) c^\dagger_{\boldsymbol{k},\sigma} c^\dagger_{-\boldsymbol{k},\sigma'} + c.c. \right] - \frac{1}{2} \sum_{\boldsymbol{k},\boldsymbol{k}'} \sum_{\sigma,\sigma'} \Delta_{\sigma\sigma'}(\boldsymbol{k}) \left\langle c^\dagger_{\boldsymbol{k},\sigma} c^\dagger_{-\boldsymbol{k},\sigma'} \right\rangle , \end{aligned} \tag{1.7}$$

where the superconducting order parameter,

$$\Delta_{\sigma\sigma'}(\boldsymbol{k}) = \sum_{\boldsymbol{k}'} V(\boldsymbol{k},\boldsymbol{k}') \langle c_{-\boldsymbol{k}',\sigma'} c_{\boldsymbol{k}',\sigma} \rangle \tag{1.8}$$

is defined. It is defined by including $V(\boldsymbol{k},\boldsymbol{k}')$, and therefore it corresponds to the energy gap.

We apply the second approximation; we assume $\Delta(\boldsymbol{k}) = \Delta_{\uparrow\downarrow}(\boldsymbol{k}) = -\Delta_{\downarrow\uparrow}(\boldsymbol{k})$ and $\Delta_{\uparrow\uparrow}(\boldsymbol{k}) = \Delta_{\downarrow\downarrow}(\boldsymbol{k}) = 0$. For spin-singlet superconductivity,

$$\begin{aligned}
\Delta(-\boldsymbol{k}) &= \Delta_{\uparrow\downarrow}(-\boldsymbol{k}) \\
&= \sum_{\boldsymbol{k}'} V(-\boldsymbol{k},\boldsymbol{k}') \left\langle c_{-\boldsymbol{k}',\downarrow} c_{\boldsymbol{k}',\uparrow} \right\rangle \\
&= \sum_{\boldsymbol{k}''} V(-\boldsymbol{k},-\boldsymbol{k}') \left\langle c_{\boldsymbol{k}',\downarrow} c_{-\boldsymbol{k}',\uparrow} \right\rangle \\
&= \sum_{\boldsymbol{k}''} V(\boldsymbol{k},\boldsymbol{k}') \left(- \left\langle c_{-\boldsymbol{k}',\uparrow} c_{\boldsymbol{k}',\downarrow} \right\rangle\right) \\
&= -\Delta_{\downarrow\uparrow}(\boldsymbol{k}) \\
&= \Delta(\boldsymbol{k}),
\end{aligned} \tag{1.9}$$

where we used the fermionic anti-commutation relations and the interaction has inversion symmetry. On the other hand, for spin-triplet superconductivity, $\Delta(-\boldsymbol{k}) = -\Delta(\boldsymbol{k})$ because $\Delta_{\uparrow\downarrow}(\boldsymbol{k}) = \Delta_{\downarrow\uparrow}(\boldsymbol{k})$. The Hamiltonian of spin-singlet superconductors is

$$\begin{aligned}
H &= \sum_{\boldsymbol{k}} \sum_{\sigma} \xi(\boldsymbol{k}) c^{\dagger}_{\boldsymbol{k},\sigma} c_{\boldsymbol{k},\sigma} + \frac{1}{2} \sum_{\boldsymbol{k},\boldsymbol{k}'} \left[ \Delta_{\uparrow\downarrow}(\boldsymbol{k}) c^{\dagger}_{\boldsymbol{k},\uparrow} c^{\dagger}_{-\boldsymbol{k},\downarrow} + \Delta_{\downarrow\uparrow}(\boldsymbol{k}) c^{\dagger}_{\boldsymbol{k},\downarrow} c^{\dagger}_{-\boldsymbol{k},\uparrow} + c.c. \right] \\
&\qquad - \frac{1}{2} \sum_{\boldsymbol{k},\boldsymbol{k}'} \Delta_{\uparrow\downarrow}(\boldsymbol{k}) \left\langle c^{\dagger}_{\boldsymbol{k},\uparrow} c^{\dagger}_{-\boldsymbol{k},\downarrow} \right\rangle + \Delta_{\downarrow\uparrow}(\boldsymbol{k}) \left\langle c^{\dagger}_{\boldsymbol{k},\downarrow} c^{\dagger}_{-\boldsymbol{k},\uparrow} \right\rangle \\
&= \sum_{\boldsymbol{k}} \sum_{\sigma} \xi(\boldsymbol{k}) c^{\dagger}_{\boldsymbol{k},\sigma} c_{\boldsymbol{k},\sigma} + \frac{1}{2} \sum_{\boldsymbol{k},\boldsymbol{k}'} \left[ \Delta(\boldsymbol{k}) c^{\dagger}_{\boldsymbol{k},\uparrow} c^{\dagger}_{-\boldsymbol{k},\downarrow} - \Delta(\boldsymbol{k}) c^{\dagger}_{\boldsymbol{k},\downarrow} c^{\dagger}_{-\boldsymbol{k},\uparrow} + c.c. \right] \\
&\qquad - \frac{1}{2} \sum_{\boldsymbol{k},\boldsymbol{k}'} \Delta(\boldsymbol{k}) \left\langle c^{\dagger}_{\boldsymbol{k},\uparrow} c^{\dagger}_{-\boldsymbol{k},\downarrow} \right\rangle - \Delta(\boldsymbol{k}) \left\langle c^{\dagger}_{\boldsymbol{k},\downarrow} c^{\dagger}_{-\boldsymbol{k},\uparrow} \right\rangle \\
&= \sum_{\boldsymbol{k}} \sum_{\sigma} \xi(\boldsymbol{k}) c^{\dagger}_{\boldsymbol{k},\sigma} c_{\boldsymbol{k},\sigma} + \frac{1}{2} \sum_{\boldsymbol{k},\boldsymbol{k}'} \left[ \Delta(\boldsymbol{k}) c^{\dagger}_{\boldsymbol{k},\uparrow} c^{\dagger}_{-\boldsymbol{k},\downarrow} - \Delta(-\boldsymbol{k}) \left( -c^{\dagger}_{\boldsymbol{k},\uparrow} c^{\dagger}_{-\boldsymbol{k},\downarrow} \right) + c.c. \right] \\
&\qquad - \frac{1}{2} \sum_{\boldsymbol{k},\boldsymbol{k}'} \Delta(\boldsymbol{k}) \left\langle c^{\dagger}_{\boldsymbol{k},\uparrow} c^{\dagger}_{-\boldsymbol{k},\downarrow} \right\rangle - \Delta(-\boldsymbol{k}) \left\langle -c^{\dagger}_{\boldsymbol{k},\uparrow} c^{\dagger}_{-\boldsymbol{k},\downarrow} \right\rangle \\
&= \sum_{\boldsymbol{k}} \sum_{\sigma} \xi(\boldsymbol{k}) c^{\dagger}_{\boldsymbol{k},\sigma} c_{\boldsymbol{k},\sigma} + \sum_{\boldsymbol{k},\boldsymbol{k}'} \left[ \Delta(\boldsymbol{k}) c^{\dagger}_{\boldsymbol{k},\uparrow} c^{\dagger}_{-\boldsymbol{k},\downarrow} + c.c. \right] - \sum_{\boldsymbol{k},\boldsymbol{k}'} \Delta(\boldsymbol{k}) \left\langle c^{\dagger}_{\boldsymbol{k},\uparrow} c^{\dagger}_{-\boldsymbol{k},\downarrow} \right\rangle
\end{aligned} \tag{1.10}$$

This Hamiltonian can be written in a matrix format.

$$H = \sum_{\boldsymbol{k}} \begin{pmatrix} c^{\dagger}_{\boldsymbol{k},\uparrow} & c_{-\boldsymbol{k},\downarrow} \end{pmatrix} \begin{pmatrix} \xi(\boldsymbol{k}) & \Delta(\boldsymbol{k}) \\ \Delta^{*}(\boldsymbol{k}) & -\xi(\boldsymbol{k}) \end{pmatrix} \begin{pmatrix} c_{\boldsymbol{k},\uparrow} \\ c^{\dagger}_{-\boldsymbol{k},\downarrow} \end{pmatrix} + const. \tag{1.11}$$

We now diagonalize the matrix. Namely, we consider a unitary transformation expressed by $\hat{U}(\boldsymbol{k})$, which makes

$$\hat{U}^\dagger(\boldsymbol{k}) \begin{pmatrix} \xi(\boldsymbol{k}) & \Delta(\boldsymbol{k}) \\ \Delta^*(\boldsymbol{k}) & -\xi(\boldsymbol{k}) \end{pmatrix} \hat{U}(\boldsymbol{k}) = \begin{pmatrix} E_1(\boldsymbol{k}) & 0 \\ 0 & E_2(\boldsymbol{k}) \end{pmatrix}. \tag{1.12}$$

The trace of the matrix,

$$\begin{cases} \mathrm{Tr} \begin{pmatrix} \xi(\boldsymbol{k}) & \Delta(\boldsymbol{k}) \\ \Delta^*(\boldsymbol{k}) & -\xi(\boldsymbol{k}) \end{pmatrix} = \xi(\boldsymbol{k}) - \xi(\boldsymbol{k}) = 0 \\ \mathrm{Tr} \begin{pmatrix} E_1(\boldsymbol{k}) & 0 \\ 0 & E_2(\boldsymbol{k}) \end{pmatrix} = E_1(\boldsymbol{k}) + E_2(\boldsymbol{k}), \end{cases} \tag{1.13}$$

does not change under a unitary transformation, therefore $E_1(\boldsymbol{k}) + E_2(\boldsymbol{k}) = 0$, and thus we can write the eigenenergies as $E_1(\boldsymbol{k}) = E(\boldsymbol{k})$ and $E_2(\boldsymbol{k}) = -E(\boldsymbol{k})$ with $E(\boldsymbol{k}) \leq 0$. The Hamiltonian becomes

$$\begin{aligned} H &= \sum_{\boldsymbol{k}} \begin{pmatrix} c^\dagger_{\boldsymbol{k},\uparrow} & c_{-\boldsymbol{k},\downarrow} \end{pmatrix} \hat{U}(\boldsymbol{k})\hat{U}^\dagger(\boldsymbol{k}) \begin{pmatrix} \xi(\boldsymbol{k}) & \Delta(\boldsymbol{k}) \\ \Delta^*(\boldsymbol{k}) & -\xi(\boldsymbol{k}) \end{pmatrix} \hat{U}(\boldsymbol{k})\hat{U}^\dagger(\boldsymbol{k}) \begin{pmatrix} c_{\boldsymbol{k},\uparrow} \\ c^\dagger_{-\boldsymbol{k},\downarrow} \end{pmatrix} \\ &= \sum_{\boldsymbol{k}} \begin{pmatrix} a^\dagger_{\boldsymbol{k},\uparrow} & a_{-\boldsymbol{k},\downarrow} \end{pmatrix} \begin{pmatrix} E(\boldsymbol{k}) & 0 \\ 0 & -E(\boldsymbol{k}) \end{pmatrix} \begin{pmatrix} a_{\boldsymbol{k},\uparrow} \\ a^\dagger_{-\boldsymbol{k},\downarrow} \end{pmatrix} \end{aligned} \tag{1.14}$$

In this format, the Hamiltonian is diagonalized. Therefore, excitations expressed by annihilation operators, $a_{\boldsymbol{k},\uparrow}$ and $a_{-\boldsymbol{k},\downarrow}$, follow the Fermi distribution, $\left\langle a^\dagger_{\boldsymbol{k},\uparrow} a_{\boldsymbol{k},\uparrow} \right\rangle = \left\langle a^\dagger_{-\boldsymbol{k},\downarrow} a_{-\boldsymbol{k},\downarrow} \right\rangle = f(E(\boldsymbol{k}))$. We call particles expressed by the operators Bogoliubov quasi-particles. Unitary transformation also conserves the determinant of the matrix.

$$\begin{aligned} \det \begin{pmatrix} \xi & \Delta \\ \Delta^* & -\xi \end{pmatrix} &= -\xi^2 - |\Delta|^2 \\ \det \begin{pmatrix} E & 0 \\ 0 & -E \end{pmatrix} &= -E^2 \end{aligned} \tag{1.15}$$

Therefore, the absolute value of the energy is

$$E(\boldsymbol{k}) = \sqrt{\xi^2(\boldsymbol{k}) + |\Delta(\boldsymbol{k})|^2} \geq |\Delta(\boldsymbol{k})|, \tag{1.16}$$

which means that the energy gap exists if $\Delta(\boldsymbol{k}) \neq 0$. This is the reason why we call $\Delta(\boldsymbol{k})$ superconducting gap. It is possible to calculate $\langle c_{-\boldsymbol{k}',\sigma'} c_{\boldsymbol{k}',\sigma} \rangle$, and we put it on Eq. 1.8. We obtain

$$\Delta(\boldsymbol{k}) = -\sum_{\boldsymbol{k}'} V(\boldsymbol{k},\boldsymbol{k}') \frac{\Delta(\boldsymbol{k}')}{2E(\boldsymbol{k}')} \tanh \frac{E(\boldsymbol{k}')}{2k_\mathrm{B}T}, \tag{1.17}$$

which is called a gap equation in BCS theory. To realize superconductivity, it is necessary that the equation have non-trivial solutions, $\Delta(\boldsymbol{k}) \neq 0$.

Finally, we apply the third approximation ($\Delta(\boldsymbol{k}) = \Delta$). This is justified in a case where the interaction $V(\boldsymbol{k}, \boldsymbol{k}')$ is given by

$$V(\boldsymbol{k}, \boldsymbol{k}') = \begin{cases} -V & \text{for } |\xi(\boldsymbol{k})|, |\xi(\boldsymbol{k}')| < \hbar\omega_{\mathrm{D}} \\ 0 & \text{otherwise} \end{cases}, \tag{1.18}$$

where we assume electron-lattice interaction, and thus $\omega_{\mathrm{D}}$ is the Debye frequency. We put $V(\boldsymbol{k}, \boldsymbol{k}')$ in the gap equation, and we obtain

$$\begin{cases} \Delta(\boldsymbol{k})|_{|\xi(\boldsymbol{k})>\hbar\omega_{\mathrm{D}}|} = -\sum_{\boldsymbol{k}'} 0 \times \frac{\Delta(\boldsymbol{k}')}{2E(\boldsymbol{k}')} \tanh \frac{E(\boldsymbol{k}')}{2k_{\mathrm{B}}T} = 0 \\ \Delta(\boldsymbol{k})|_{|\xi(\boldsymbol{k})<\hbar\omega_{\mathrm{D}}|} = V \underbrace{\sum_{\boldsymbol{k}'} \frac{\Delta(\boldsymbol{k}')}{2E(\boldsymbol{k}')} \tanh \frac{E(\boldsymbol{k}')}{2k_{\mathrm{B}}T}}_{\text{no dependence of } \boldsymbol{k}} = \Delta (= const.) \end{cases} \tag{1.19}$$

Therefore, the gap equation becomes

$$\Delta = V \sum_{\boldsymbol{k}' \text{ for } |\xi(\boldsymbol{k}')|<\hbar\omega_{\mathrm{D}}} \frac{\Delta}{2E(\boldsymbol{k}')} \tanh \frac{E(\boldsymbol{k}')}{2k_{\mathrm{B}}T} \tag{1.20}$$

where $E(\boldsymbol{k}) = \sqrt{\xi^2(\boldsymbol{k}) + |\Delta|^2}$. To calculate this equation, we replace the summation over $\boldsymbol{k}'$ by an energy integral $\int_{-\hbar\omega_{\mathrm{D}}}^{\hbar\omega_{\mathrm{D}}} d\xi \rho(\xi)$ with density of states $\rho(\xi)$, and usually we approximate $\rho(\xi) \sim \rho(0)$ since $\hbar\omega_{\mathrm{D}}$ is far smaller than the energy band width.

$$\Delta = V\rho(0) \int_{-\hbar\omega_{\mathrm{D}}}^{\hbar\omega_{\mathrm{D}}} d\xi \rho(\xi) \frac{\Delta}{2\sqrt{\xi^2 + |\Delta|^2}} \tanh \frac{\sqrt{\xi^2 + |\Delta|^2}}{2k_{\mathrm{B}}T} \tag{1.21}$$

It is easy to calculate the order parameter at $T = 0$ since $\tanh \frac{\sqrt{\xi^2+|\Delta|^2}}{2k_{\mathrm{B}}T} \to 1$ for $T \to 0$.

$$\begin{aligned} \Delta(T=0) &= V\rho(0) \int_{-\hbar\omega_{\mathrm{D}}}^{\hbar\omega_{\mathrm{D}}} d\xi \frac{\Delta(T=0)}{2\sqrt{\xi^2 + |\Delta(T=0)|^2}} \\ &= \frac{\Delta(T=0)V\rho(0)}{2} \int_{-\hbar\omega_{\mathrm{D}}/|\Delta|}^{\hbar\omega_{\mathrm{D}}/|\Delta|} \frac{dx}{\sqrt{x^2+1}} \\ &= \Delta(T=0)V\rho(0) \left[ \ln\left( x + \sqrt{x^2+1} \right) \right]_0^{\hbar\omega_{\mathrm{D}}/|\Delta|} \\ &\sim \Delta(T=0)V\rho(0) \ln\left( \frac{2\hbar\omega_{\mathrm{D}}}{|\Delta(T=0)|} \right) \end{aligned} \tag{1.22}$$

We can easily solve the equation with respect to $\Delta(T=0)$, and we obtain

$$|\Delta(T=0)| = 2\hbar\omega_{\mathrm{D}} \exp\left(-\frac{1}{V\rho(0)}\right) \tag{1.23}$$

To obtain the critical temperature $T_{\mathrm{c}}$, we linearize the gap equation; we take the limit of $\Delta \to 0$, and we ignore quadratic terms of $\Delta$.

$$1 = V\rho(0) \int_{-\hbar\omega_{\mathrm{D}}}^{\hbar\omega_{\mathrm{D}}} d\xi \frac{1}{2\xi} \tanh \frac{\xi}{2k_{\mathrm{B}}T_{\mathrm{c}}} \tag{1.24}$$

This is called linearized gap equation. The integral is possible (see, for example, 8.3 of Ref. [4]) under the condition of $\hbar\omega_{\mathrm{D}}/k_{\mathrm{B}}T_{\mathrm{c}} \gg 1$, and we obtain the critical temperature as

$$k_{\mathrm{B}}T_{\mathrm{c}} = \frac{2e^{\gamma}}{\pi}\hbar\omega_{\mathrm{D}} \exp\left(-\frac{1}{V\rho(0)}\right) = 1.13\hbar\omega_{\mathrm{D}} \exp\left(-\frac{1}{V\rho(0)}\right) \tag{1.25}$$

where $\gamma = 0.57721\cdots$ is Euler's constant.

With Eq. 1.23 and Eq 1.25, we obtain the following relation between the critical temperature and the order parameter at $T=0$.

$$\frac{2|\Delta(T=0)|}{k_{\mathrm{B}}T_{\mathrm{c}}} = \frac{2\pi}{e^{\gamma}} = 3.53 \tag{1.26}$$

This value does not depend on material. This is one of the important conclusions of BCS theory. Surprisingly, many typical BCS-type superconductors show values close to 3.53 even if we applied a bold approximation to $V(\boldsymbol{k}, \boldsymbol{k}')$.

## 1.4 Iron-based superconductors

### 1.4.1 Discovery of iron-based superconductors

The first discovery of iron-based superconductors was in LaFePO [6] in 2006 by Proferssor Hosono's group in Tokyo Institute of Technology. Two years later, they discovered the first iron arsenide high-$T_{\mathrm{c}}$ superconductor, $\mathrm{LaFeAs(O_{1-x}F_x)}$ ($T_{\mathrm{c}} = 26$ K) [7]. The crystal structure( Fig. 1.3) is very simple but tunable, therefore variations of iron-based superconductors have started to be synthesized.

### 1.4.2 Crystal structure

Iron-based superconductors can be classified into several families based on the composition ratio of their parent materials. However, all of these systems have a common local

| | $T_c$ [K] | $\hbar\omega_D/k_B$ [K] | $2\Delta(0)/k_BT_c$ |
|---|---|---|---|
| Al | 1.2 | 375 | 3.53 |
| In | 3.4 | 109 | 3.65 |
| Zn | 0.9 | 235 | 3.44 |
| Sn | 3.75 | 195 | 3.57–3.61 |
| V | 5.3 | 338 | 3.50 |
| Nb | 9.2 | 320 | 3.65 |
| Hg | 4.16 | 79 | 3.95 |
| Pb | 7.22 | 96 | 3.95 |

Table. 1.1: Superconducting critical temperature $T_c$, Debye frequency $\hbar\omega_D$ in Kelvin and ratio $2\Delta(0)/k_BT_c$ between order parameter at $T = 0$ and $T_c$ of typical superconductors [5].

structure; the iron elements are arranged in a square lattice and surrounded by the pnictogen ($Pn$ =P, As) or chalcogen ($Ch$ =S, Se, Te) elements in a tetrahedral shape. These tetrahedra share an edge and are connected to form a Fe$Pn$ (Fe$Ch$) layer, which is the conducting layer. These conducting layers overlap either directly or through multilayers, forming a quasi-two-dimensional crystal structure (Fig. 1.3).

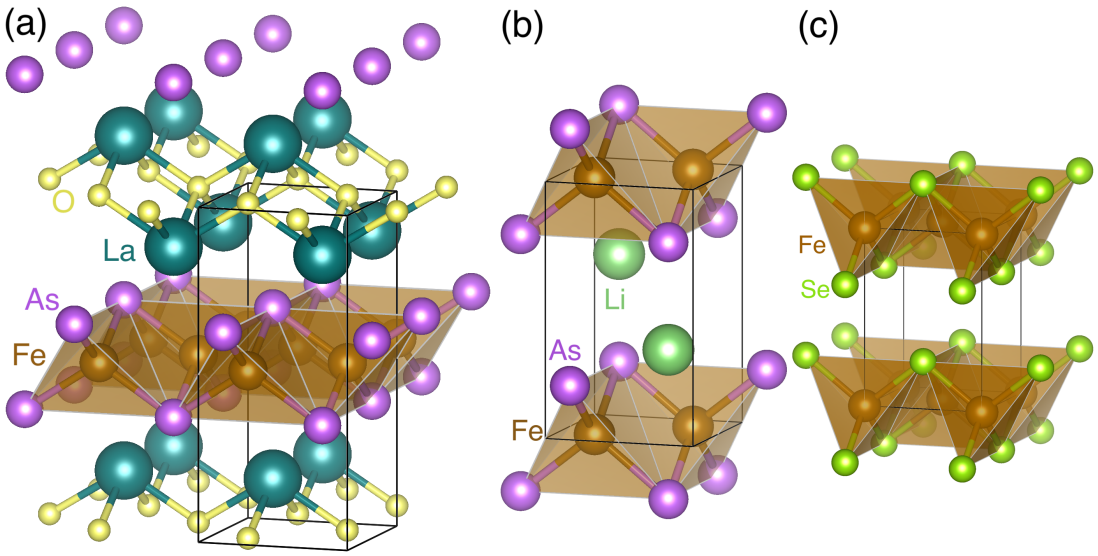


Fig.1.3: Crystal structures of (a) LaFeAsO [7], (b) LiFeAs [8] and (c) FeSe [9].

### 1.4.3 Electronic structure

The most important feature of iron-based superconductors is that they are multi-orbital systems. We summarize the electronic structures in this paragraph. In iron-based superconductors, there are orbital degrees of freedom derived from iron $d$ orbitals, and therefore inter-orbital Coulomb interactions are effective while cuprates are described by one-orbital models. Moreover, parent compounds of iron-based superconductors are mainly antiferromagnetic metals while those of cuprates are Mott insulators.

Crystal field in tetrahedral complex splits the fivefold degenerate $d$ orbitals of $Fe^{2+}$ into two $e_g$ ($d_{x^2-y^2}$ and $d_{z^2}$) and three $t_{2g}$ ($d_{xz}$, $d_{yz}$ and $d_{xy}$) orbitals in ascending order of energy (Fig. 1.4). For simplification, we assume that the tetrahedral crystal field splitting $\Delta_{\text{tetra.}}$ is enough large. Six $3d$ electrons of $Fe^{2+}$ are filled as shown in Fig. 1.4 (a). The $e_g$ orbitals are fully filled, and the $t_{2g}$ orbitals are 1/3-filled. Realistic electronic structures are not so simple (see Fig. 1.4 (b)); the crystal field splitting is not so large, however the antiferromagnetic metal ground states of parent compounds are understood by the above arguments.

When describing electronic structures of iron-based superconductors, a special unit cell is conventionally used. The typical unit cell of an iron-based superconductor is the dashed line shown in Fig. 1.4 (d), in which each unit cell contains two iron atoms. As mentioned above, $3d$ orbital of iron accounts for most of the contribution to the physical properties. Both Fe sites are located at the center of the tetrahedron whose vertex is $Pn$ or $Ch$, and there is no difference between the sites if we treat only the Fe$Pn$ or Fe$Ch$ layer. Therefore, the unit cell can be recast as a unit cell containing only one atom of iron, as shown by the solid line in Fig. 1.4 (d). Electron orbitals are often defined in the coordinate system of this new unit cell ($xy$ coordinates in Fig. 1.4 (d)). The unit cell is folded along the solid line in Fig. 1.4 (d), and the Brillouin zone is unfolded in the reciprocal lattice space. Fermi surface is also unfolded following the Brillouin zone (Fig. 1.4 (e)). This process is generally called unfolding [10]. A ten-band model (five Fe $3d$ orbitals $\times$ two sites) in the original unit cell becomes a five-band system in the unfolded Brillouin zone. In this thesis, unfolded electronic structures are used unless otherwise noted.

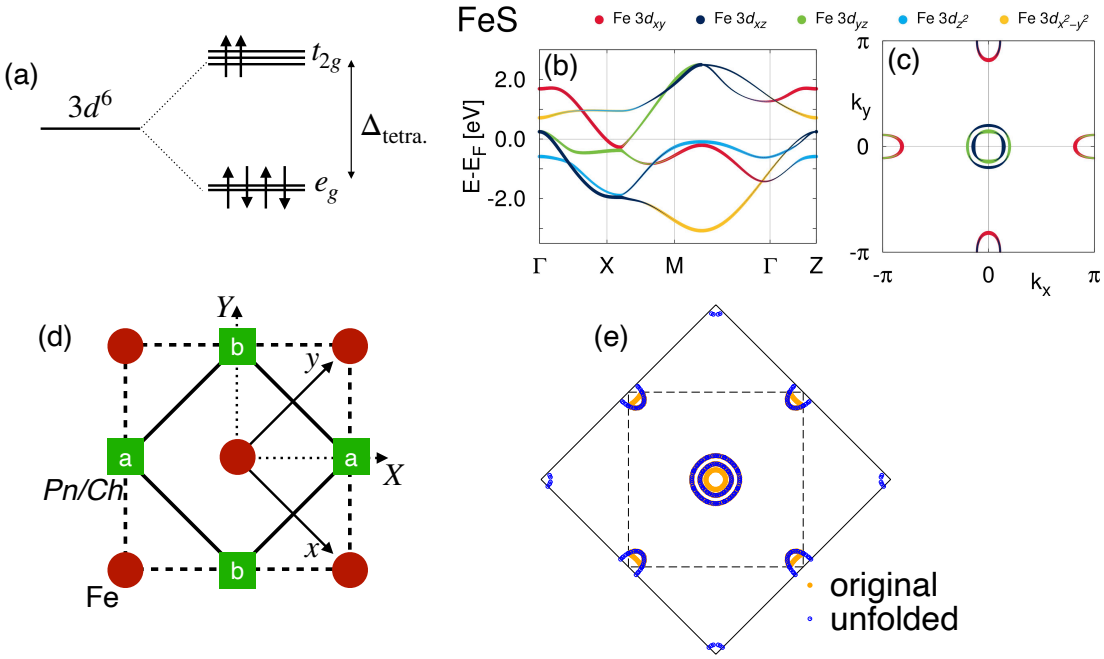


Fig.1.4: (a) Configuration of six electrons of $3d$ orbitals in $Fe^2+$. (b) Band structure and (c) Fermi surface of FeS. (d) Schematic figure of an iron layer of iron-based superconductors. (e) Typical Fermi surface of iron-based superconductors colored with blue and unfolded one colored with orange.

### 1.4.4 Superconductivity

Since the early stages of the research of iron-based superconductors, it has been pointed out that they are unconventional superconductors, not mediated by the conventional phonon mechanism [11].

Spin fluctuation has been proposed as the superconducting mechanism since the discovery of iron-based superconductors [12, 13]. In this theory, superconductivity is mediated by spin fluctuations existing in the vicinity of the antiferromagnetic ordering phase of parent materials. The spin fluctuation scenario suggests that the sign of a gap function is changed between nesting vectors corresponding to the antiferromagnetic spin fluctuations, and thus, sing-changing $s$-wave, abbreviated as $s_{\pm}$-wave hereafter and $d_{x^2-y^2}$-wave gap functions are suggested. Either of them is realized depending on topology of the Fermi surface.

Iron-based superconductors show domes in the superconducting transition temperature

$T_c$ as other unconventional superconductors do. Theoretically, superconductivity in iron-based materials has been tackled from a weak coupling perspective, describing Fermi surface instabilities that lead to superconductivity via spin fluctuations [12–14], and from a strong coupling picture by considering these materials as doped Mott insulators, where superconductivity is obtained from approximatively solved $t$-$J$ models [15–17]. However, capturing superconducting $T_c$ trends continues to be a theoretical challenge [18]. Within a spin fluctuation scenario, the $T_c$ increase with doping has been explained for lithium ammonia intercalated FeSe [19], and for FeS, a pressure induced double dome was captured [20]. The dispute between itinerant and localized electron pictures is ongoing, and while some iron-based superconductor families, like 1111, are more itinerant, others, like hole doped 122 and iron chalcogenides are more localized. In fact, superconductivity can be shown to depend both on Fermi surface shape and antiferromagnetic exchange [21]. Even in the absence of a magnetic ground state, the nature of the magnetic exchange has important implications for nematicity and superconductivity in FeSe [22] and for the differences between iron pnictides and germanides [23].

### 1.4.5 FeSe-based superconductors

The structurally simplest class of iron-based superconductors with its prime representative FeSe [24] was discovered in the same year as LaFeAsO [7]. With the establishment of a method for preparing pure single crystal FeSe by chemical vapor transport in 2013 [25], more physical property measurements in FeSe have been conducted. FeSe has been intensively studied due to its very large nematic region [26], which occurs in a very large temperature range [27], its interesting magnetism [22], and the complexity of its electronic structure [28], which is not correctly captured by any known electronic structure technique [29].

The $T_c$ of bulk FeSe is just 8 K, however it can be significantly enhanced if the van der Waals gap between the iron selenium layers is intercalated with alkali metal ions, for example by the ammonia technique [30–33] or directly in the structurally complicated $A_xFe_{2-y}Se_2$ type of compounds with $A$ = K, Rb, Cs [34, 35]. Further possibilities are completely inorganic lithium hydroxide intercalates [36, 37], and alkali metal intercalates stabilized by organic solvents [38]. Not only FeSe but also FeS [39] and $FeSe_{1-x}Te_x$ [40, 41] can be intercalated.

At least three tuning parameters have been identified that provide control over the superconducting transition temperature: Pressure can increase the $T_c$ of bulk FeSe from 8 K at ambient pressure to 36.7 K [42]. By electron doping via lithium and ammonia intercalation, $T_c$ up to 55 K can be reached [33]. The spacing between FeSe layers can be systematically increased using amines of increasing size, like ethylenediamine ($C_2H_8N_2$) [38, 43], 2-phenethylamine ($C_3H_{11}N$) [44], diaminopropane ($C_3H_{10}N_2$) [43, 45], hexamethylenediamine ($C_6H_{16}N_2$) [46, 47], and $T_c$ up to 41 K has been observed [47]. Tuning parameters can also be combined, for example by pressurizing doped FeSe intercalates [45, 48–50]. When parameters like pressure or doping, which can be varied continuously, are tuned away from their optimal values, characteristic superconducting domes are observed [45, 48–51].

The superconducting mechanism of the electron-doped FeSe-based superconductors is still controversial. It is not obvious whether spin fluctuations are developed since absence of hole pockets around $\boldsymbol{k} = (0, 0)$ which are essential for the common spin fluctuations in iron-based superconductors is reported [52–54]. On the other hand, recent nuclear magnetic resonance (NMR) experiments for FeSe intercalates support the spin fluctuations scenario [55]. Theoretically, some mechanisms are suggested in this situation. One is spin fluctuations, which mediate superconductivity with a sign-changing $s$-wave ($s_{\pm}$-wave hereafter) gap function even if the hole pockets are slightly below the Fermi level [56–58]. Another one is orbital fluctuations, which mediate a $s$-wave gap function without a sign-changing (called $s_{++}$-wave) [59, 60]. It is still controversial; whether it is spin fluctuations, nematic fluctuations or combinations of them.

### 1.4.6 FeS

Only in 2015 was it established that the isostructural FeS is also a superconductor [61]. Even though the replacement of Se by the smaller S appears to be a minor structural modification, it soon became clear that FeSe and FeS behave differently in several respects: The nematic region is absent in FeS [62], the electronic correlations appear to be significantly smaller in FeS [63], and the upper critical field is much smaller [64]. In fact, the possibility to grow high-quality mixed $FeSe_{1-x}S_x$ structures has provided opportunities to study the evolution of properties between FeSe and FeS [63, 65–68].

Superconductivity in FeS has been observed below $T_c = 5$ K [61] with some varia-

tion due to sample dependence [69]. Scanning tunneling spectroscopy points to strong-coupling superconductivity [70], and Hall conductivities can be fitted with a two-band model [71]. The symmetry of the superconducting gap in FeS has been the subject of some debate. Using scanning tunneling spectroscopy, Yang et al. [70] conclude that the superconducting gap of FeS is strongly anisotropic. Specific heat measurements [72] and quasiparticle heat transport studies [73] point to a nodal gap structure. However, muon spin rotation studies found fully gapped behavior in FeS [74, 75]. Theoretically, a $d_{x^2-y^2}$ order parameter at ambient pressure has been obtained [70].

Pressure has been shown to suppress superconductivity in FeS [76]. Surprisingly, however, Zhang et al. [51] have found that, after the initial suppression, at a pressure of $P = 5$ GPa superconductivity reemerges, and a second superconducting dome is formed, up to a pressure of $P = 22.3$ GPa. Such double-dome superconductivity is known to occur also in alkali iron selenides [48] and in FeSe intercalates [45, 49]. In fact, two superconducting domes occur in nearly all classes of unconventional superconductors [77].

In our previous study, we consider the structurally simple FeS as an instructive example system for studying the origin of double-dome superconductivity in iron-based materials. We show that, at a pressure of $P = 4.6$ GPa, a Lifshitz transition occurs, adding a hole pocket to the Fermi surface and boosting the density of states at the Fermi level. Using the spin fluctuation theory in the random phase approximation, we show that the pairing strength of the $d_{x^2-y^2}$ order parameter, which dominates within the low-pressure dome, decreases until a Lifshitz transition of the electronic structure takes place. At the transition, the superconducting order parameter switches to nodeless $s_{\pm}$, and the pairing strength grows significantly to a new maximum. Our study highlights that, also in iron chalcogenides, the spin fluctuation scenario works, and that Lifshitz transitions play an important role in electronic phase diagrams.

## 1.5 Organic superconductors

Compounds are classified into two groups, inorganic compounds and organic compounds. Atoms are arranged, and they directly construct the compounds. Therefore, variations of inorganic compounds are based on variations of atoms. On the other hand, almost all the organic compounds consist of molecules. Atoms constitute molecules, and the molecules are arranged in the compounds. Millions of molecules in the world makes

organic compounds much more variable than inorganic compounds.

In addition to the variations of molecules, organic compounds have variations of crystal structure. One of the main interactions constructing crystals is the van-der-Waals force, which is a weak interaction between molecules. Therefore, small change of molecules and compositions make the crystal structure different.

Organic compounds are usually insulating. In 1954, Akamatsu *et al.* discovered the first organic conductor, perylene bromide [78]. Bromine removes some of the electrons in perylene, holes become mobile, and thus it becomes conducting (halogen doping).

### 1.5.1 Discovery of organic superconductors

The first organic superconductor [79], $(TMTSF)_2PF_6$ where TMTSF stands for tetramethyltetraselenafulvalene, with the superconducting critical temperature $T_c = 0.9$ K at 11kbar was discovered in 1979. After that, superconductivity was found also in other TMTSF charge transfer salts. In TMTSF charge transfer salts, $(TMTSF)_2X$, TMTSF molecules and anion $X^-$ form salts, and they form crystals. The $\pi$-orbitals, which are perpendicular to the molecules, of the TMTSF have a larger overlap, and they form a quasi-one-dimensional structure. These TMTSF complexes shows a large ($\sim 1000$) anisotropy of electronic conductivity, which is an evidence of the quasi-one-dimensionality. The one-dimensionality is a disadvantage for conductivity and superconductivity since it tends to cause a Peierls transition.

### 1.5.2 $\kappa$-type BEDT-TTF charge transfer salts

To avoid the Peierls transition, a donor molecule, BEDT-TTF, which stands for bis(ethylenedithio)tetrathiafulvalene and abbreviated ET hereafter, was designed so that the molecular orbitals spread to the transverse sections. In $(ET)_2X$, ET donor molecules construct two-dimensional planes, and the donor ET planes and the acceptor $X$ planes are alternately stacked. The outer rings of ET have a larger thickness than the inner rings. They interrupt the arrangements, and therefore the synthesis tends to be more difficult than other molecules like TMTSF. As a result, various arrangements of the molecules are realized, and they are classified into $\alpha, \beta, \kappa, \theta, \cdots$. With small modifications, we put a prime symbol to the original arrangements, for example, $\beta, \beta', \beta'', \ldots$. Especially, $\kappa$-type salts have most superconducting materials in the ET

charge transfer salts. Let us focus on $\kappa$-type in this thesis.

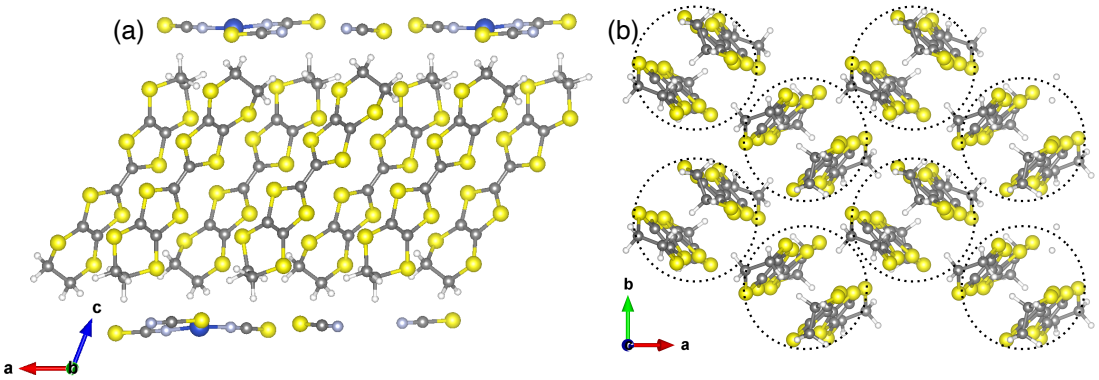


Fig.1.5: Crystal structure of $\kappa$-$(ET)_2X$: (a) side view and (b) top view of the BEDT-TTF(ET) layer. Dashed-line circles show the dimerization in (b).

### Electronic structure

Electronic structures of organic charge transfer salts are understood well with molecular orbitals. While the highest occupied molecular orbitals (HOMO) of isolated neutral ET molecules are fully filled, the monovalent ions $X^{-1}$ provide 0.5 hole per ET molecule to the ET conducting layers in $\kappa$-$(ET)_2X$. Therefore the HOMO orbitals are 3/4 filled by electrons, or 1/4 filled by holes. Note that the ions $X^{-1}$ have a closed shell and therefore are not responsible for electronic conduction and magnetism. It has been suggested that $\kappa$-type in particular have a strong tendency for molecules to form dimers, and dimers form almost a square lattices. The ions $X^{-1}$ provide a hole per dimer, and therefore they are half-filled in dimer models.

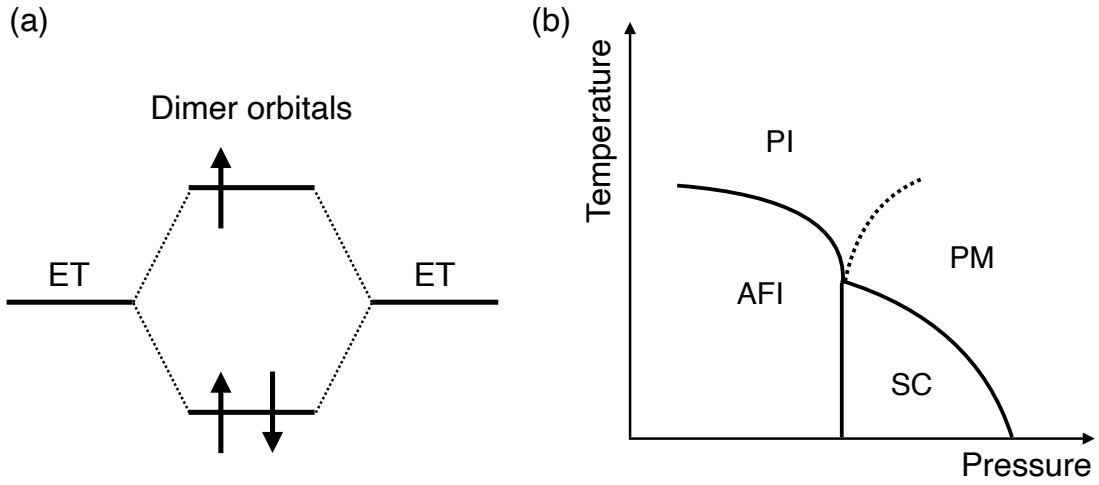


Fig.1.6: (a) electronic configurations in the dimer model. (b) Schematic phase diagram of $\kappa$-$(ET)_2X$ with paramagnetic insulating (PI), antiferromagnetic insulating (AFI) paramagnetic metal (PM) and superconducting (SC) states.

### Superconductivity

It is strongly implied that the superconductivity is related to electron correlations by the fact that it is in the vicinity of the Mott insulating state. Spin fluctuation of the antiferromagnetism has been proposed as a mechanism of the superconductivity, however, it is still controversial.

To understand microscopic mechanism of superconductivity, identification of a superconducting gap function plays an important role. Initial NMR experiments [80–83] below $T_c$ have shown (1) no coherence peak, (2) decrease of Knight shift and (3) $T^3$-law of the $1/T_1$ in the low temperature region. These results suggest that the superconducting gap has nodes, and a $d$-wave gap function rather than fully gapped $s$-wave has been suggested. Theoretically, such a gap function with nodes has been understood by spin fluctuation theory on an effective dimer model, for example, with Hartree-Fock approximation [84], with FLEX approximation [85] and with quantum Monte Carlo [86]. They have concluded that superconductivity with $d_{xy}$-wave gap function is enhanced by the same mechanism with the high-$T_c$ cuprate superconductors. The suggested $d_{xy}$-wave gap function has been soon supported by a millimeter-wave transmission experiment [87].

However, a few years later, different interpretations on this experiment are proposed [88, 89], and moreover, $d_{x^2-y^2}$-wave rather than $d_{xy}$-wave gap function has

been suggested by STS [90] and thermal conductivity [91] measurements. They have cast doubt on the spin fluctuation scenario based on the dimer model. Based on the experimental results, Kuroki *et al.* has studied corresponding molecular models within FLEX [92], which has suggested that $d_{xy}$- and $d_{x^2-y^2}$-wave gap functions are nearly degenerate, and the $d_{x^2-y^2}$-wave gap function is realized when the dimerization is not so strong. Strength of dimerization in $\kappa$-(BEDT-TTF) charge transfer salts is characterized by magnitude of hopping transfers, $t_1$ hereafter, between ET molecules in a dimer; limit of large $t_1$ corresponds to strong dimerization. Recent *ab-initio* DFT calculations suggest that $t_1$ is not so strong in every $\kappa$-$(\mathrm{ET})_2X$, in fact. After that, four-site molecular models become standard in study of $\kappa$-$(\mathrm{ET})_2X$.

Developments in experimental techniques have enabled more detailed observations of the superconducting gap function. Surprisingly, $s$-wave [93–97] and $s_{\pm}+d_{x^2-y^2}$-wave [97–99] are also suggested. Gap function is not settled. Detailed study based on the spin fluctuation theory suggests that such superconducting symmetries result from degree of freedom in molecule models [100]. This work shows an important suggestion that it is necessary to consider a specific molecule model for each $\kappa$-$(\mathrm{ET})_2X$.

| $i$ | Material | $T_\mathrm{c}$(K) |
|---|---|---|
| 1 | $\kappa$-$(\mathrm{ET})_2\mathrm{Ag}(\mathrm{CF_3})_4(\mathrm{TCE})$ | 2.6 |
| 2 | $\kappa$-$(\mathrm{ET})_2\mathrm{I_3}$ [101] | 3.6 |
| 3 | $\kappa$-$(\mathrm{ET})_2\mathrm{Ag}(\mathrm{CN})_2\cdot\mathrm{H_2O}$ [102] | 5.0 |
| 4 | $\kappa$-$\alpha_1'$-$(\mathrm{ET})_2\mathrm{Ag}(\mathrm{CF_3})_4(\mathrm{TCE})$ | 9.5 |
| 5 | $\kappa$-$(\mathrm{ET})_2\mathrm{Cu}(\mathrm{NCS})_2$ | 10.4 |
| 6 | $\kappa$-$\alpha_2'$-$(\mathrm{ET})_2\mathrm{Ag}(\mathrm{CF_3})_4(\mathrm{TCE})$ | 11.1 |
| 7 | $\kappa$-$(\mathrm{ET})_2\mathrm{Cu}[\mathrm{N}(\mathrm{CN})_2](\mathrm{CN})$ | 11.2 |
| 8 | $\kappa$-$(\mathrm{ET})_2\mathrm{Cu}[\mathrm{N}(\mathrm{CN})_2]\mathrm{Br}$ [103] | 11.6 |

Table. 1.2: $T_\mathrm{c}$ values of $\kappa$-$(\mathrm{ET})_2X$.

## 1.6 Motivations of this thesis

We have followed from typical BCS superconductors to unconventional superconductors like iron-based superconductors and organic superconductors. Variation of materials,

pressure and carrier doping level make rich phase diagrams and different superconducting critical temperature and symmetry, especially. Motivation of this thesis is to access such variation of $T_c$ and superconducting symmetry and to find the key parameters to control them.

Specifically, the following two subjects are studied in this thesis.

First is a superconducting $T_c$ dome shown in the $x$–$T$ phase diagram where $T$ is temperature, and $x$ is electron doping level of $Li_x(C_3N_2H_{10})_{0.37}FeSe$. $Li_x(C_3N_2H_{10})_{0.37}FeSe$ is a FeSe-based superconductor intercalated with lithium and diaminopropane ($C_3N_2H_{10}$), where wide range ($0.06 \leq x \leq 0.68$) of electron-doping is realized. $T_c$ is enhanced in the low doping ($x < 0.37$) up to $T_c = 46$ K ($x = 0.37$), and suppressed in the high doping ($x > 0.37$). This material is unique since the electron-doping covers a wide region from the weak to strong coupling, where the weak and strong coupling limits are $x = 0$ and $x = 1$ respectively. Therefore, it is important to understand the electronic phase diagram in this material.

Second is superconducting symmetry of $\kappa$-type (BEDT-TTF) charge transfer salts. The family, which has the largest number of superconducting materials in organic charge transfer salts has been studied since the first synthesis in the 1980s. $d$-wave superconducting gap functions have been suggested by both of experimental and theoretical studies, however other possibilities like fully gapped $s$-wave and $s_{\pm} + d_{x^2-y^2}$-wave are suggested by recent experiments. Specific theoretical calculations for the materials are needed to identify the superconducting symmetry.

This thesis is organized as follows. Chapter 2 – 4 summarize methods and formalizations. Green's function method is summarized in Chapter 2, spin fluctuation theory is summarized in Chapter 3, and microscopic theory of superconductivity with Green's functions is summarized in Chapter 4. Chapter 5 summarizes results for the lithium and diaminopropane intercalated FeSe. Chapter 6 summarizes results for $\kappa$-type (BEDT-TTF) charge transfer salts.

# Chapter 2

# Green's function formalism in normal states

In the study of physics, especially condensed matter physics, it is the usual approach to apply an external field to a sample and measure the response. For example, we apply an electric field and measure an electric current. We apply a magnetic field and measure a magnetic susceptibility. We apply a difference of temperature and measure heat flow.

External fields take a system into a non-equilibrium state, which is difficult to deal with in theoretical physics. However, for the linear response, where the field and the response are under a linear relationship, change from the equilibrium state by the field is equivalent to the fluctuation in the equilibrium state. This is called the Kubo formula, which describes the linear response of a system. To calculate such response functions, the Green's function method is a powerful and useful approach.

## 2.1 Green's functions at finite temperature

### 2.1.1 Formalism of Green's functions at finite temperature

In general, a Green's function is defined as a statistical average of a product, $c(x)c^{\dagger}(x')$, of creation and annihilation operators. This definition implies that Green's functions show how the disturbance propagates when we create a particle as we throw a stone into a pond to test if the pond is frozen.

The electron Green's function is defined as a statistical average of a product of creation

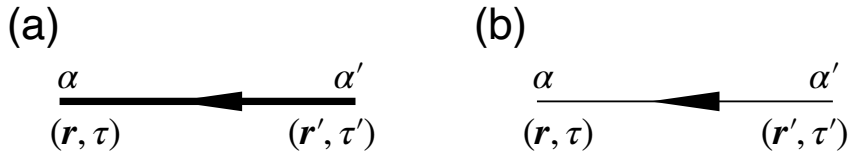


Fig.2.1: Diagrams of (a) electron Green's function $G_{\alpha\alpha'}(\boldsymbol{R},\tau;\boldsymbol{R}',\tau')$ defined in Eq. (2.1) and (b) non-interacting Green's function $G^0_{\alpha\alpha'}(\boldsymbol{R},\tau;\boldsymbol{R}',\tau')$, which is Green's function of free elements.

and annihilation operators as mentioned above, however, several kinds of definitions [*1] are used for this purpose. In this document, we use time-ordered Green's functions at finite temperature.

T. Matsubara introduced imaginary-time $\tau$ [104], and A. A. Abrikosov, L. P. Gorkov and I. E. Dzyaloshinskii established a formalism of Green's function at finite temperature [105]. Their formalism enables to use perturbation theory and the method of Feynman diagrams also at finite temperature. We call such Green's functions in imaginary-time at finite temperature Matsubara Green's functions. A time-ordered Matsubara Green's function is defined as

$$\begin{aligned} G_{\alpha\alpha'}(\boldsymbol{R},\tau;\boldsymbol{R}',\tau') &= -\left\langle T_\tau c_\alpha(\boldsymbol{R},\tau)c^\dagger_{\alpha'}(\boldsymbol{R}',\tau')\right\rangle \\ &= -\left\langle \theta(\tau-\tau')c_\alpha(\boldsymbol{R},\tau)c^\dagger_{\alpha'}(\boldsymbol{R}',\tau') - \theta(\tau'-\tau)c^\dagger_{\alpha'}(\boldsymbol{R}',\tau')c_\alpha(\boldsymbol{R},\tau)\right\rangle \end{aligned} \tag{2.1}$$

where $c_\alpha(\boldsymbol{R},\tau) = e^{\tau H}c_\alpha(\boldsymbol{R})e^{-\tau H}$ is an annihilation operator of electron with a quantum number $\alpha$ which is a combination of spin $\sigma$, orbital $l$ and so on in the Heisenberg picture, and $\theta(\tau-\tau')$ is a step function,

$$\theta(\tau-\tau') = \begin{cases} 0 & \text{for } \tau < \tau' \\ 1 & \text{for } \tau > \tau' \end{cases}. \tag{2.2}$$

$\boldsymbol{R}$ are the Bravais lattice vectors, which denote unit cells.

$\left\langle \hat{A}\right\rangle$ is the statistical average of $\hat{A}$,

$$\left\langle \hat{A}\right\rangle = \frac{\mathrm{Tr}\left\{e^{-\beta(\hat{H}-\mu\hat{N})}\hat{A(\tau)}\right\}}{\mathrm{Tr}\left\{e^{-\beta(\hat{H}-\mu\hat{N})}\right\}} \tag{2.3}$$

[*1] For instance, time-ordered, retarded, advanced, and so on.

where $\hat{A}(\tau) = e^{\hat{H}\tau}\hat{A}e^{-\hat{H}\tau}$ is in the Heisenberg picture. The advantage of the imaginary time is here; when we include a perturbation of the Hamiltonian like $\hat{H} = \hat{H}^0 + \hat{H}'$, then the exponent of the Heisenberg picture is similar to that of the statistical average. (If we had stick to the conventional real time, it would have been $e^{i\hat{H}t}$.) Therefore, the imaginary time makes safer and easier perturbation theory possible. In this document, we define $\left\langle \hat{A} \right\rangle_0$ for the statistical average with $\hat{H}^0$.

$$\left\langle \hat{A} \right\rangle_0 = \frac{\mathrm{Tr}\left\{ e^{-\beta(\hat{H}^0 - \mu\hat{N})} \hat{A(\tau)} \right\}}{\mathrm{Tr}\left\{ e^{-\beta(\hat{H}^0 - \mu\hat{N})} \right\}} \tag{2.4}$$

Matsubara Green's functions $G(\boldsymbol{R}, \tau; \boldsymbol{R}', \tau')$ depend on $\tau - \tau'$ not $\tau$ and $\tau'$ independently. Therefore, it is possible to chose the origin of imaginary time at $\tau'$, and rewrite it as $G(\boldsymbol{R}; \boldsymbol{R}', \tau) = G(\boldsymbol{R}, \tau; \boldsymbol{R}', \tau' = 0)$. Matsubara Green's functions are (anti-)periodic with period $\beta = 1/k_{\mathrm{B}}T$ as

$$G_{\alpha\alpha'}(\tau) = \begin{cases} G_{\alpha\alpha'}(\tau + \beta) & \text{for fermions} \\ -G_{\alpha\alpha'}(\tau + \beta) & \text{for bosons} \end{cases} \tag{2.5}$$

The above (anti-)periodicity makes the following Fourier transform possible.

$$\begin{aligned} G_{\alpha\alpha'}(\boldsymbol{k}, i\varepsilon_n) &= \sum_{\boldsymbol{R}, \boldsymbol{R}'} e^{-i\boldsymbol{k}\cdot(\boldsymbol{R} - \boldsymbol{R}')} \int_0^\beta d\tau e^{i\varepsilon_n \tau} G_{\alpha\alpha'}(\boldsymbol{R}; \boldsymbol{R}', \tau) \\ G_{\alpha\alpha'}(\boldsymbol{R}; \boldsymbol{R}', \tau) &= \int \frac{d\boldsymbol{k}}{(2\pi)^3} e^{i\boldsymbol{k}\cdot(\boldsymbol{R} - \boldsymbol{R}')} \frac{1}{\beta} \sum_{n=-\infty}^{\infty} e^{-i\varepsilon_n \tau} G_{\alpha\alpha'}(\boldsymbol{k}, i\varepsilon_n) \end{aligned} \tag{2.6}$$

The transform seems very common, but the frequency is unique because of the (anti-)periodicity. It is called Matsubara frequency and given by

$$\varepsilon_n = \begin{cases} \omega_n & = (2n+1)\pi k_{\mathrm{B}}T \text{ for fermions} \\ \nu_n & = 2n\pi k_{\mathrm{B}}T \text{ for bosons} \end{cases} \tag{2.7}$$

Note that $\boldsymbol{R}$, which denotes real space are the Bravais lattice vectors,

$$\{\boldsymbol{R} : \boldsymbol{R} = n_1\boldsymbol{a}_1 + n_2\boldsymbol{a}_2 + n_3\boldsymbol{a}_3\} \tag{2.8}$$

so that the wave vectors, $\boldsymbol{k} = k_1\boldsymbol{b}_1 + k_2\boldsymbol{b}_2 + k_3\boldsymbol{b}_3$, are expressed with the reciprocal lattice

vectors,

$$\begin{aligned}\boldsymbol{b}_1 &= 2\pi\frac{\boldsymbol{a}_2\times\boldsymbol{a}_3}{\boldsymbol{a}_1\cdot(\boldsymbol{a}_2\times\boldsymbol{a}_3)}\\ \boldsymbol{b}_2 &= 2\pi\frac{\boldsymbol{a}_3\times\boldsymbol{a}_1}{\boldsymbol{a}_1\cdot(\boldsymbol{a}_2\times\boldsymbol{a}_3)}\\ \boldsymbol{b}_3 &= 2\pi\frac{\boldsymbol{a}_1\times\boldsymbol{a}_2}{\boldsymbol{a}_1\cdot(\boldsymbol{a}_2\times\boldsymbol{a}_3)}\end{aligned} \tag{2.9}$$

(Also see the Appendix A.)

### 2.1.2 Green's functions of tight-binding models

We consider a tight-binding model given by the following Hamiltonian.

$$H=\sum_{\boldsymbol{R},\boldsymbol{R}'}\sum_{\alpha,\alpha'}(t_{\alpha\alpha'}(\boldsymbol{R},\boldsymbol{R}')-\mu\delta_{\alpha\alpha'}\delta_{\boldsymbol{R}\boldsymbol{R}'})c^\dagger_\alpha(\boldsymbol{R})c_{\alpha'}(\boldsymbol{R}') \tag{2.10}$$

$\mu$ is the chemical potential. For simplification of the indices, we introduce indices, $i=(\boldsymbol{R},\alpha)$ and $j=(\boldsymbol{R}',\alpha')$ which we use until we have to do the Fourier transform from $\boldsymbol{R}$ to $\boldsymbol{k}$. The Hamiltonian is written as

$$H=-\sum_{i,j}(t_{ij}+\mu\delta_{ij})c^\dagger_i c_j. \tag{2.11}$$

First, we differentiate the Green's function with respect to $\tau$.

$$\begin{aligned}&\frac{\partial}{\partial\tau}G^0_{ij}(\tau)\\ &=-\left\langle\frac{\partial\theta(\tau)}{\partial\tau}c_i(\tau)c^\dagger_j+\theta(\tau)\frac{\partial c_i(\tau)}{\partial\tau}c^\dagger_j-\frac{\partial\theta(-\tau)}{\partial\tau}c^\dagger_j c_i(\tau)-\theta(-\tau)c^\dagger_j\frac{\partial c_i(\tau)}{\partial\tau}\right\rangle\end{aligned} \tag{2.12}$$

Here, the derivative of the step functions are

$$\begin{aligned}\frac{\partial\theta(\tau)}{\partial\tau}&=\delta(\tau)\\ \frac{\partial\theta(-\tau)}{\partial\tau}&=-\delta(-\tau)=-\delta(\tau),\end{aligned} \tag{2.13}$$

and the Heisenberg equation of motion of the tight-binding model in imaginary time is

$$\begin{aligned}
\frac{\partial c_i(\tau)}{\partial \tau} &= e^{\tau H}[H, c_i]e^{-\tau H} \\
&= e^{\tau H}\left[\sum_{j,k}(t_{ij}-\mu\delta_{ij})c_i^\dagger c_j, c_i\right]e^{-\tau H} \\
&= \sum_{i,j}(t_{ij}-\mu\delta_{ij})e^{\tau H}\underbrace{\left[c_i^\dagger c_j, c_i\right]}_{=c_j^\dagger\{c_k,c_i\}-\left\{c_j^\dagger,c_i\right\}c_k=-\delta_{ij}c_k}e^{-\tau H} \\
&= -\sum_k(t_{ik}-\mu\delta_{ik})e^{\tau H}c_k e^{-\tau H} \\
&= -\sum_k(t_{ik}-\mu\delta_{ik})c_k(\tau)
\end{aligned} \tag{2.14}$$

.

Therefore, $\partial G_{ij}^0(\tau)/\partial\tau$ becomes

$$\begin{aligned}
&\frac{\partial}{\partial\tau}G_{ij}^0(\tau) \\
&= -\left\langle \delta(\tau)c_i(\tau)c_j^\dagger - \theta(\tau)\sum_k(t_{ik}-\mu\delta_{ik})c_k(\tau)c_j^\dagger + \delta(\tau)c_j^\dagger c_i(\tau) + \theta(-\tau)\sum_k(t_{ik}-\mu\delta_{ik})c_j^\dagger c_k(\tau)\right\rangle \\
&= -\sum_k(t_{ik}-\mu\delta_{ik})\underbrace{\left\{-\left\langle\theta(\tau)c_k(\tau)c_j^\dagger - \theta(-\tau)c_j^\dagger c_k(\tau)\right\rangle\right\}}_{G_{kj}^0(\tau)} - \delta(\tau)\left\langle\underbrace{\left\{c_i(\tau), c_j^\dagger\right\}}_{\delta_{ij}}\right\rangle \\
&= -\sum_k(t_{ik}-\mu\delta_{ik})G_{kj}^0(\tau) - \delta(\tau)\delta_{ij}
\end{aligned} \tag{2.15}$$

Second, we perform the Fourier transform from imaginary time $\tau$ to Matsubara frequency $i\omega_n$, which means we substitute

$$G_{ij}^0(\tau) = \frac{1}{\beta}\sum_{n=-\infty}^{\infty} e^{-i\omega_n\tau}G_{ij}^0(i\omega_n) \tag{2.16}$$

and

$$\delta(\tau) = \frac{1}{\beta}\sum_{n=-\infty}^{\infty} e^{-i\omega_n\tau}. \tag{2.17}$$

Then, we obtain

$$\frac{1}{\beta}\sum_{n=-\infty}^{\infty} G^0_{ij}(i\omega_n)\underbrace{\frac{\partial}{\partial\tau}e^{-i\omega_n\tau}}_{=-i\omega_n e^{-i\omega_n\tau}} = -\sum_k (t_{ik}-\mu\delta_{ik})\frac{1}{\beta}\sum_{n=-\infty}^{\infty} G^0_{kj}(i\omega_n)e^{-i\omega_n\tau} - \frac{1}{\beta}\sum_{n=-\infty}^{\infty}\frac{\partial}{\partial\tau}e^{-i\omega_n\tau}\delta_{ij} \tag{2.18}$$

$$\frac{1}{\beta}\sum_{n=-\infty}^{\infty} e^{-i\omega_n}\left[i\omega_n G^0_{ij}(i\omega_n) - \sum_k (t_{ik}-\mu\delta_{ik})G^0_{kj}(i\omega_n) - \delta_{ij}\right] = 0 \tag{2.19}$$

$$i\omega_n G^0_{ij}(i\omega_n) - \sum_k (t_{ik}-\mu\delta_{ik})G^0_{kj}(i\omega_n) = \delta_{ij} \tag{2.20}$$

$$\sum_k \left[(i\omega_n+\mu)\delta_{ik} - t_{ik}\right] G^0_{kj}(i\omega_n) = \delta_{ij} \tag{2.21}$$

Finally we take the Fourier transform from $\boldsymbol{R}$ to $\boldsymbol{k}$. We return to the expression with $i \to (\boldsymbol{R},\alpha)$, $j \to (\boldsymbol{R}',\alpha')$ and $k \to (\boldsymbol{R}''',\alpha''')$. Eq. (2.21) becomes

$$\sum_{\boldsymbol{R}''}\sum_{\alpha''}\left[(i\omega_n+\mu)\delta_{\alpha,\alpha''}\delta_{\boldsymbol{R},\boldsymbol{R}''} - t_{\alpha\alpha''}(\boldsymbol{R};\boldsymbol{R}'')\right] G^0_{\alpha''\alpha}(\boldsymbol{R}'';\boldsymbol{R},i\omega_n) = \delta_{\alpha,\alpha'}\delta_{\boldsymbol{R},\boldsymbol{R}'} \tag{2.22}$$

We take the Fourier transform from the lattice vectors $\boldsymbol{R}$ to the corresponding wave-vectors $\boldsymbol{k}$, which means that we substitute

$$\begin{aligned} G^0_{\alpha\alpha'}(\boldsymbol{R};\boldsymbol{R}') &= \int \frac{d\boldsymbol{k}}{(2\pi)^3} e^{i\boldsymbol{k}\cdot(\boldsymbol{R}-\boldsymbol{R}')} G^0_{\alpha\alpha'}(\boldsymbol{k}) \\ t_{\alpha\alpha''}(\boldsymbol{R};\boldsymbol{R}'') &= \int \frac{d\boldsymbol{k}}{(2\pi)^3} e^{i\boldsymbol{k}\cdot(\boldsymbol{R}-\boldsymbol{R}'')} G^0_{\alpha\alpha''}(\boldsymbol{k}) \\ \delta_{\boldsymbol{R},\boldsymbol{R}''} &= \int \frac{d\boldsymbol{k}}{(2\pi)^3} e^{i\boldsymbol{k}\cdot(\boldsymbol{R}-\boldsymbol{R}'')}. \end{aligned} \tag{2.23}$$

Then, the equation becomes

$$\sum_{\boldsymbol{R}''}\sum_{\alpha''}\int \frac{d\boldsymbol{k}}{(2\pi)^3} e^{i\boldsymbol{k}\cdot(\boldsymbol{R}-\boldsymbol{R}'')}\left[(i\omega_n+\mu)\delta_{\alpha,\alpha''} - t_{\alpha\alpha''}(\boldsymbol{k})\right]\int \frac{d\boldsymbol{k}'}{(2\pi)^3} e^{i\boldsymbol{k}'\cdot(\boldsymbol{R}''-\boldsymbol{R}')} G^0_{\alpha''\alpha'}(\boldsymbol{k}',i\omega_n) = \delta_{\alpha\alpha'}\int \frac{d\boldsymbol{k}}{(2\pi)^3} e^{i\boldsymbol{k}\cdot(\boldsymbol{R}-\boldsymbol{R}')}. \tag{2.24}$$

The left-hand side of the equation is

$$
\begin{aligned}
(LHS) = &\sum_{\alpha''} \int \frac{d\boldsymbol{k}}{(2\pi)^3} e^{i\boldsymbol{k}\cdot\boldsymbol{R}} \left[(i\omega_n + \mu)\delta_{\alpha,\alpha''} - t_{\alpha\alpha''}(\boldsymbol{k})\right] \int \frac{d\boldsymbol{k}'}{(2\pi)^3} e^{-i\boldsymbol{k}'\cdot\boldsymbol{R}'} G^0_{\alpha''\alpha'}(\boldsymbol{k}', i\omega_n) \\
&\times \underbrace{\sum_{\boldsymbol{R}''} e^{-i(\boldsymbol{k}-\boldsymbol{k}')\cdot\boldsymbol{R}''}}_{=\delta(\boldsymbol{k}-\boldsymbol{k}')} \\
&= \sum_{\alpha''} \int \frac{d\boldsymbol{k}}{(2\pi)^3} e^{i\boldsymbol{k}\cdot(\boldsymbol{R}-\boldsymbol{R}')} \left[(i\omega_n + \mu)\delta_{\alpha,\alpha''} - t_{\alpha\alpha''}(\boldsymbol{k})\right] G^0_{\alpha''\alpha'}(\boldsymbol{k}, i\omega_n)
\end{aligned}
\tag{2.25}
$$

Therefore, the equation is

$$
\int \frac{d\boldsymbol{k}}{(2\pi)^3} e^{i\boldsymbol{k}\cdot(\boldsymbol{R}-\boldsymbol{R}')} \left\{ \sum_{\alpha''} \left[(i\omega_n + \mu)\delta_{\alpha,\alpha''} - t_{\alpha\alpha''}(\boldsymbol{k})\right] G^0_{\alpha''\alpha'}(\boldsymbol{k}, i\omega_n) - \delta_{\alpha\alpha'} \right\} = 0 \tag{2.26}
$$

To make the equation true,

$$
\sum_{\alpha''} \left[(i\omega_n + \mu)\delta_{\alpha,\alpha''} - t_{\alpha\alpha''}(\boldsymbol{k})\right] G^0_{\alpha''\alpha'}(\boldsymbol{k}, i\omega_n) = \delta_{\alpha\alpha'} \tag{2.27}
$$

To solve this equation, we write it in the form

$$
\sum_{\alpha''} M_{\alpha\alpha''}(i\omega_n) G^0_{\alpha''\alpha'}(i\omega_n) = \delta_{\alpha\alpha'} \tag{2.28}
$$

where

$$
\begin{aligned}
M_{\alpha\alpha'}(i\omega_n) &= (i\omega_n + \mu)\delta_{\alpha\alpha'} - t_{\alpha\alpha'}(\boldsymbol{k}) \\
&= (i\omega_n + \mu)\delta_{\alpha\alpha'} - h_{\alpha\alpha'}(\boldsymbol{k})
\end{aligned}
\tag{2.29}
$$

.

Here we defined

$$
h_{\alpha\alpha'}(\boldsymbol{k}) = t_{\alpha\alpha'}(\boldsymbol{k}) = \sum_{\boldsymbol{R},\boldsymbol{R}'} e^{-i\boldsymbol{k}\cdot(\boldsymbol{R}-\boldsymbol{R}')} t_{\alpha\alpha'}(\boldsymbol{R};\boldsymbol{R}'), \tag{2.30}
$$

which is equivalent to the hamiltonian with $\mu = 0$. Once we define the matrix form of

the Green's functions as

$$\hat{G}^0(k) = \begin{pmatrix} G^0_{11}(k) & G^0_{12}(k) & G^0_{13}(k) & \cdots \\ G^0_{21}(k) & G^0_{22}(k) & G^0_{23}(k) & \cdots \\ G^0_{31}(k) & G^0_{32}(k) & G^0_{33}(k) & \cdots \\ \vdots & \vdots & \vdots & \ddots \end{pmatrix}$$
$$\hat{M}(k) = \begin{pmatrix} M_{11}(k) & M_{12}(k) & M_{13}(k) & \cdots \\ M_{21}(k) & M_{22}(k) & M_{23}(k) & \cdots \\ M_{31}(k) & M_{32}(k) & M_{33}(k) & \cdots \\ \vdots & \vdots & \vdots & \ddots \end{pmatrix}, \tag{2.31}$$

the equation becomes

$$\hat{M}(k)\hat{G}^0(k) = \hat{1} \tag{2.32}$$

or

$$\hat{G}^0(k) = \hat{M}^{-1}(k) \tag{2.33}$$

where $k$ is the abbreviation of $k = (\boldsymbol{k}, i\omega_n)$.

## 2.2 Dyson equation

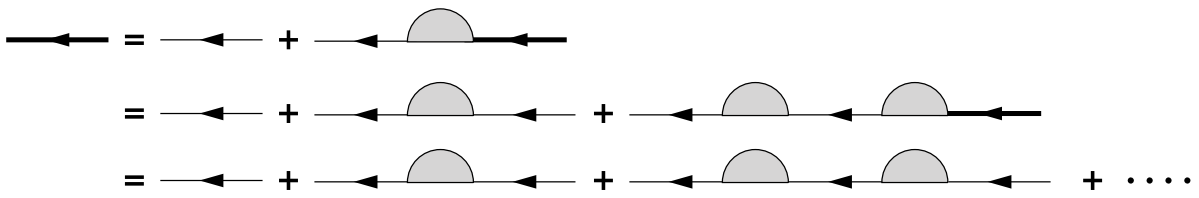

Fig.2.2: Diagrams of the Dyson equation, Eq. (2.37). The bold lines are the Green's functions, $G(k)$, and the thin lines are the non-interacting Green's functions, $G^0(k)$ as defined in Fig. 2.1.

Feynman-Dyson perturbation theory is summarized by a equation named Dyson equation [106]. The Green's function $G$ is expressed with the non-interacting Green's function

$G^0$ and the proper self-energy $\Sigma$ as

$$\begin{aligned}
G_{\alpha\alpha'}(x;x') &= G^0_{\alpha\alpha'}(x;x') \\
&+ \sum_{x_1,x_2} \sum_{\alpha_1,\alpha_2} G^0_{\alpha\alpha_1}(x;x_1)\Sigma_{\alpha_1\alpha_2}(x_1;x_2)G^0_{\alpha_2\alpha'}(x_2;x') \\
&+ \sum_{x_1,x_2,x_3,x_4} \sum_{\alpha_1,\alpha_2,\alpha_3,\alpha_4} G^0_{\alpha\alpha_1}(x;x_1)\Sigma_{\alpha_1\alpha_2}(x_1;x_2)G^0_{\alpha_2\alpha_3}(x_2;x_3)\Sigma_{\alpha_3\alpha_4}(x_3;x_4)G^0_{\alpha_4\alpha'}(x_4;x') \\
&+ \cdots \\
&= G^0_{\alpha\alpha'}(x;x') + \sum_{x_1,x_2} \sum_{\alpha_1,\alpha_2} G^0_{\alpha\alpha_1}(x;x_1)\Sigma_{\alpha_1\alpha_2}(x_1;x_2)G_{\alpha_2\alpha'}(x_2;x')
\end{aligned} \tag{2.34}$$

where $x$ and $\sum_x$ are the abbreviations of $x = (\boldsymbol{R}, \tau)$ and $\sum_x = \sum_{\boldsymbol{R}} \int_0^\beta d\tau$. The Fourier transform of Eq. (2.34) is

$$G_{\alpha\alpha'}(k) = G^0_{\alpha\alpha'}(k) + \sum_{\alpha_1,\alpha_2} G^0_{\alpha\alpha_1}(k)\Sigma_{\alpha_1\alpha_2}(k)G_{\alpha_2\alpha'}(k). \tag{2.35}$$

The corresponding diagram is shown in Fig. 2.2. Once we define the matrix form of the Green's functions and the self-energy as

$$\begin{aligned}
\hat{G}(k) &= \begin{pmatrix} G_{11}(k) & G_{12}(k) & G_{13}(k) & \cdots \\ G_{21}(k) & G_{22}(k) & G_{23}(k) & \cdots \\ G_{31}(k) & G_{32}(k) & G_{33}(k) & \cdots \\ \vdots & \vdots & \vdots & \ddots \end{pmatrix} \\
\hat{G}^0(k) &= \begin{pmatrix} G^0_{11}(k) & G^0_{12}(k) & G^0_{13}(k) & \cdots \\ G^0_{21}(k) & G^0_{22}(k) & G^0_{23}(k) & \cdots \\ G^0_{31}(k) & G^0_{32}(k) & G^0_{33}(k) & \cdots \\ \vdots & \vdots & \vdots & \ddots \end{pmatrix} \\
\hat{\Sigma}(k) &= \begin{pmatrix} \Sigma_{11}(k) & \Sigma_{12}(k) & \Sigma_{13}(k) & \cdots \\ \Sigma_{21}(k) & \Sigma_{22}(k) & \Sigma_{23}(k) & \cdots \\ \Sigma_{31}(k) & \Sigma_{32}(k) & \Sigma_{33}(k) & \cdots \\ \vdots & \vdots & \vdots & \ddots \end{pmatrix},
\end{aligned} \tag{2.36}$$

we obtain the Dyson equation,

$$\hat{G}(k) = \hat{G}^0(k) + \hat{G}^0(k)\hat{\Sigma}(k)\hat{G}(k), \tag{2.37}$$

in matrix format. The Dyson equation in matrix format is equivalent to the following two equations.

$$\left[\hat{1} - \hat{G}^0(k)\hat{\Sigma}(k)\right]\hat{G}(k) = \hat{G}^0(k) \tag{2.38}$$

$$\hat{G}(k) = \left[ [\hat{G}^0]^{-1}(k) - \hat{\Sigma}(k) \right]^{-1} \tag{2.39}$$

The Green's function is renormalized by self-energy $\Sigma$. Therefore, we arrive at the problems of obtaining $\Sigma$.

# Chapter 3

# Spin fluctuation theory

## 3.1 Formalism of fluctuation

### 3.1.1 Single-orbital case

Based on the Kubo formula in linear response theory [107], the charge susceptibility, the longitudinal spin susceptibility and the transverse spin susceptibility are given by

$$\chi^{\mathrm{c}}(\boldsymbol{q}, i\nu_n) = \int_0^\beta d\tau e^{i\nu_n\tau} \sum_{\boldsymbol{R},\boldsymbol{R}'} e^{i\boldsymbol{q}\cdot(\boldsymbol{R}-\boldsymbol{R}')}\chi^{\mathrm{c}}(\boldsymbol{R}, \boldsymbol{R}'; \tau), \tag{3.1}$$

$$\chi^{zz}(\boldsymbol{q}, i\nu_n) = \int_0^\beta d\tau e^{i\nu_n\tau} \sum_{\boldsymbol{R},\boldsymbol{R}'} e^{i\boldsymbol{q}\cdot(\boldsymbol{R}-\boldsymbol{R}')}\chi^{zz}(\boldsymbol{R}, \boldsymbol{R}'; \tau), \tag{3.2}$$

$$\chi^{\mathrm{tr.}}(\boldsymbol{q}, i\nu_n) = \int_0^\beta d\tau e^{i\nu_n\tau} \sum_{\boldsymbol{R},\boldsymbol{R}'} e^{i\boldsymbol{q}\cdot(\boldsymbol{R}-\boldsymbol{R}')}\chi^{\mathrm{tr.}}(\boldsymbol{R}, \boldsymbol{R}'; \tau), \tag{3.3}$$

where $\chi^{\mathrm{c}}(\boldsymbol{R}, \tau; \boldsymbol{R}', 0)$, $\chi^{zz}(\boldsymbol{R}, \tau; \boldsymbol{R}', 0)$ and $\chi^{\pm}(\boldsymbol{R}, \tau; \boldsymbol{R}', 0)$ are correlation functions of the charge fluctuation, the longitudinal spin fluctuation and the transverse spin fluctuation as shown below.

$$\chi^{\mathrm{c}}(x; x') = \frac{1}{2}\left\langle \rho(x); \rho(x') \right\rangle, \tag{3.4}$$

$$\chi^{zz}(x; x') = 2\left\langle S^z(x); S^z(x') \right\rangle, \tag{3.5}$$

$$\chi^{\mathrm{tr.}}(x; x') = \left\langle S^+(x); S^-(x') \right\rangle \tag{3.6}$$

$\langle A(x);B(x')\rangle = \langle T_\tau A(\boldsymbol{R},\tau)B(\boldsymbol{R}',\tau')\rangle$ is the two-point correlation function of operators $A$ and $B$. $\rho(x)$, $S^z(x)$ and $S^\pm(x)$ are a charge operator, $z$-component of a spin operator and spin ladder operators expressed as

$$\rho(x) = n_\uparrow(x) + n_\downarrow(x), \tag{3.7}$$

$$S^z(x) = \frac{1}{2}\left[n_\uparrow(x) - n_\downarrow(x)\right], \tag{3.8}$$

$$S^\pm(x) = S^x(x) \pm iS^y(x) = \begin{cases} c^\dagger_\uparrow(x)c_\downarrow(x) \\ c^\dagger_\downarrow(x)c_{i\uparrow}(x) \end{cases}, \tag{3.9}$$

where $n_\sigma(x) = c^\dagger_\sigma(x)c_\sigma(x)$ is an electron number operator.

With creation and annihilation operators, the correlation functions are written as

$$\begin{aligned}
\chi^{\mathrm{c}}(x;x') &= \frac{1}{2}\left\langle n_\uparrow(x) + n_\downarrow(x); n_\uparrow(x') + n_{j\downarrow}(x')\right\rangle \\
&= \frac{1}{2}\Big[\left\langle c^\dagger_\uparrow(x)c_\uparrow(x); c^\dagger_\uparrow(x')c_\uparrow(x')\right\rangle + \left\langle c^\dagger_\downarrow(x)c_\downarrow(x); c^\dagger_\downarrow(x')c_\downarrow(x')\right\rangle \\
&\qquad + \left\langle c^\dagger_\uparrow(x)c_\uparrow(x); c^\dagger_\downarrow(x')c_\downarrow(x')\right\rangle + \left\langle c^\dagger_\downarrow(x)c_\downarrow(x); c^\dagger_\uparrow(x')c_\uparrow(x')\right\rangle\Big] \\
&= \frac{1}{2}\left[\chi^{\uparrow\uparrow}(x;x') + \chi^{\uparrow\downarrow}(x;x') + \chi^{\downarrow\uparrow}(x;x') + \chi^{\downarrow\downarrow}(x;x')\right],
\end{aligned} \tag{3.10}$$

$$\begin{aligned}
\chi^{zz}(x;x') &= \frac{1}{2}\left\langle n_\uparrow(x) - n_\downarrow(x); n_\uparrow(x') - n_\downarrow(x')\right\rangle \\
&= \frac{1}{2}\Big[\left\langle c^\dagger_\uparrow(x)c_\uparrow(x); c^\dagger_\uparrow(x')c_\uparrow(x')\right\rangle + \left\langle c^\dagger_\downarrow(x)c_\downarrow(x); c^\dagger_\downarrow(x')c_\downarrow(x')\right\rangle \\
&\qquad - \left\langle c^\dagger_\uparrow(x)c_\uparrow(x); c^\dagger_\downarrow(x')c_\downarrow(x')\right\rangle - \left\langle c^\dagger_\downarrow(x)c_\downarrow(x); c^\dagger_\uparrow(x')c_\uparrow(x')\right\rangle\Big] \\
&= \frac{1}{2}\left[\chi^{\uparrow\uparrow}(x;x') - \chi^{\uparrow\downarrow}(x;x') - \chi^{\downarrow\uparrow}(x;x') + \chi^{\downarrow\downarrow}(x;x')\right],
\end{aligned} \tag{3.11}$$

$$\begin{aligned}
\chi^{\mathrm{tr.}}(x;x') &= \left\langle c^\dagger_\uparrow(x)c_\downarrow(x); c^\dagger_\downarrow(x')c_\uparrow(x')\right\rangle \\
&= \chi^{+-}(x;x'),
\end{aligned} \tag{3.12}$$

where $\chi^{\sigma\sigma'} = \left\langle c^\dagger_\sigma c_\sigma; c^\dagger_{\sigma'}c_{\sigma'}\right\rangle$ and $\chi^{+-} = \left\langle c^\dagger_\uparrow c_\downarrow; c^\dagger_\downarrow c_\uparrow\right\rangle$.

In the paramagnetic state, the transverse spin susceptibility becomes

$$\begin{aligned}
\chi^{\mathrm{tr.}}(x;x') &= \left\langle S^+(x);\ S^-(x')\right\rangle \\
&= \left\langle \left(S^x(x)+iS^y(x)\right);\ \left(S^x(x')-iS^y(x')\right)\right\rangle \\
&= \left[\langle S^x(x);S^x(x')\rangle + \langle S^x(y);S^y(x')\rangle\right] \\
&= 2\left\langle S^z(x);S^z(x')\right\rangle \\
&= \chi^{zz}(x;x')
\end{aligned} \tag{3.13}$$

since $\langle S^z(x);S^z(x')\rangle = \langle S^z(y);S^z(y')\rangle = \langle S^z(z);S^z(z')\rangle$. Therefore, we define the spin susceptibility as

$$\chi^{\mathrm{s}}(q) = \chi^{zz}(q) = \chi^{\mathrm{tr.}}(q) \tag{3.14}$$

in the paramagnetic state. Moreover, charge and spin susceptibility are calculated with generalized fluctuation correlation functions as

$$\begin{aligned}
\chi^{\mathrm{c}}(q) &= \chi^{\uparrow\uparrow}(q) + \chi^{\uparrow\downarrow}(q), \\
\chi^{zz}(q) &= \chi^{\uparrow\uparrow}(q) - \chi^{\uparrow\downarrow}(q), \\
\chi^{\mathrm{tr.}}(q) &= \chi^{+-}(q)
\end{aligned} \tag{3.15}$$

since $\chi^{\uparrow\uparrow} = \chi^{\downarrow\downarrow}$ and $\chi^{\uparrow\downarrow} = \chi^{\downarrow\uparrow}$.

In a system without electronic correlations, the susceptibilities are calculated as

$$\begin{aligned}
\chi^{\mathrm{c,nonint.}}(\boldsymbol{q},\tau) &= \frac{1}{2}\sum_{\sigma}\sum_{\boldsymbol{k},\boldsymbol{k}'}\Big[\left\langle c^\dagger_{\sigma,\boldsymbol{k}}(\tau)c_{\sigma,\boldsymbol{k}+\boldsymbol{q}}(\tau);\ c^\dagger_{\sigma,\boldsymbol{k}'+\boldsymbol{q}}c_{\sigma,\boldsymbol{k}'}\right\rangle_0 \\
&\qquad + \left\langle c^\dagger_{\sigma,\boldsymbol{k}}(\tau)c_{\sigma,\boldsymbol{k}+\boldsymbol{q}}(\tau);\ c^\dagger_{\bar{\sigma},\boldsymbol{k}'+\boldsymbol{q}}c_{\bar{\sigma},\boldsymbol{k}'}\right\rangle_0\Big] \\
&= -\frac{1}{2}\sum_{\sigma}\sum_{\boldsymbol{k},\boldsymbol{k}'}\Big[\underbrace{\left\langle c_{\sigma,\boldsymbol{k}+\boldsymbol{q}}(\tau)c^\dagger_{\sigma,\boldsymbol{k}'+\boldsymbol{q}}\right\rangle_0}_{=-\delta_{\boldsymbol{k},\boldsymbol{k}'}G^0_\sigma(\boldsymbol{k}+\boldsymbol{q},\tau)}\underbrace{\left\langle c_{\sigma,\boldsymbol{k}'}c^\dagger_{\sigma,\boldsymbol{k}}(\tau)\right\rangle_0}_{=-\delta_{\boldsymbol{k},\boldsymbol{k}'}G^0_\sigma(\boldsymbol{k},-\tau)} \\
&\qquad + \underbrace{\left\langle c_{\sigma,\boldsymbol{k}+\boldsymbol{q}}(\tau)c^\dagger_{\bar{\sigma},\boldsymbol{k}'+\boldsymbol{q}}\right\rangle_0}_{=0}\underbrace{\left\langle c_{\bar{\sigma},\boldsymbol{k}'}c^\dagger_{\sigma,\boldsymbol{k}}(\tau)\right\rangle_0}_{=0}\Big] \\
&= -\frac{1}{2}\sum_{\sigma}\sum_{\boldsymbol{k}} G^0_\sigma(\boldsymbol{k}+\boldsymbol{q},\tau)G^0_\sigma(\boldsymbol{k},-\tau) \\
&= -\sum_{\boldsymbol{k}} G^0(\boldsymbol{k}+\boldsymbol{q},\tau)G^0(\boldsymbol{k},-\tau),
\end{aligned} \tag{3.16}$$

$$
\begin{aligned}
\chi^{zz,\mathrm{nonint.}}(\boldsymbol{q},\tau) &= \frac{1}{2}\sum_{\sigma}\sum_{\boldsymbol{k},\boldsymbol{k}'}\Big[\Big\langle c^{\dagger}_{\sigma,\boldsymbol{k}}(\tau)c_{\sigma,\boldsymbol{k}+\boldsymbol{q}}(\tau);\ c^{\dagger}_{\sigma,\boldsymbol{k}'+\boldsymbol{q}}c_{\sigma,\boldsymbol{k}'}\Big\rangle_0 \\
&\qquad - \Big\langle c^{\dagger}_{\sigma,\boldsymbol{k}}(\tau)c_{\sigma,\boldsymbol{k}+\boldsymbol{q}}(\tau);\ c^{\dagger}_{\bar{\sigma},\boldsymbol{k}'+\boldsymbol{q}}c_{\bar{\sigma},\boldsymbol{k}'}\Big\rangle_0\Big] \\
&= -\frac{1}{2}\sum_{\sigma}\sum_{\boldsymbol{k},\boldsymbol{k}'}\Big[\underbrace{\Big\langle c_{\sigma,\boldsymbol{k}+\boldsymbol{q}}(\tau)c^{\dagger}_{\sigma,\boldsymbol{k}'+\boldsymbol{q}}\Big\rangle_0}_{=-\delta_{\boldsymbol{k},\boldsymbol{k}'}G^0_{\sigma}(\boldsymbol{k}+\boldsymbol{q},\tau)}\underbrace{\Big\langle c_{\sigma,\boldsymbol{k}'}c^{\dagger}_{\sigma,\boldsymbol{k}}(\tau)\Big\rangle_0}_{=-\delta_{\boldsymbol{k},\boldsymbol{k}'}G^0_{\sigma}(\boldsymbol{k},-\tau)} \\
&\qquad - \underbrace{\Big\langle c_{\sigma,\boldsymbol{k}+\boldsymbol{q}}(\tau)c^{\dagger}_{\bar{\sigma},\boldsymbol{k}'+\boldsymbol{q}}\Big\rangle_0}_{=0}\underbrace{\Big\langle c_{\bar{\sigma},\boldsymbol{k}'}c^{\dagger}_{\sigma,\boldsymbol{k}}(\tau)\Big\rangle_0}_{=0}\Big] \\
&= -\frac{1}{2}\sum_{\sigma}\sum_{\boldsymbol{k}} G^0_{\sigma}(\boldsymbol{k}+\boldsymbol{q},\tau)G^0_{\sigma}(\boldsymbol{k},-\tau) \\
&= -\sum_{\boldsymbol{k}} G^0(\boldsymbol{k}+\boldsymbol{q},\tau)G^0(\boldsymbol{k},-\tau),
\end{aligned}
\tag{3.17}
$$

$$
\begin{aligned}
\chi^{\mathrm{tr.,nonint.}}(\boldsymbol{q},\tau) &= \sum_{\boldsymbol{k},\boldsymbol{k}'}\Big\langle c^{\dagger}_{\uparrow,\boldsymbol{k}}(\tau)c_{\downarrow,\boldsymbol{k}+\boldsymbol{q}}(\tau);\ c^{\dagger}_{\downarrow,\boldsymbol{k}'+\boldsymbol{q}}c_{\uparrow,\boldsymbol{k}'}\Big\rangle_0 \\
&= -\sum_{\boldsymbol{k},\boldsymbol{k}'}\underbrace{\Big\langle c_{\downarrow,\boldsymbol{k}+\boldsymbol{q}}(\tau)c^{\dagger}_{\downarrow,\boldsymbol{k}'+\boldsymbol{q}}\Big\rangle_0}_{=-\delta_{\boldsymbol{k},\boldsymbol{k}'}G^0_{\downarrow}(\boldsymbol{k}+\boldsymbol{q},\tau)}\underbrace{\Big\langle c_{\uparrow,\boldsymbol{k}'}c^{\dagger}_{\uparrow,\boldsymbol{k}}(\tau)\Big\rangle_0}_{=-\delta_{\boldsymbol{k},\boldsymbol{k}'}G^0_{\uparrow}(\boldsymbol{k},-\tau)} \\
&= -\sum_{\boldsymbol{k}} G^0(\boldsymbol{k}+\boldsymbol{q},\tau)G^0(\boldsymbol{k},-\tau),
\end{aligned}
\tag{3.18}
$$

where $G^0(k) = G^0_{\uparrow}(k) = G^0_{\downarrow}(k)$ in the paramagnetic state. Therefore, in non-interacting cases, all of the susceptibilities are equivalent to

$$
\chi^0(\boldsymbol{q},\tau) = -\sum_{\boldsymbol{k}} G^0(\boldsymbol{k}+\boldsymbol{q},\tau)G^0(\boldsymbol{k},-\tau), \tag{3.19}
$$

which is called irreducible susceptibility. The Fourier transform of $\chi^0(\boldsymbol{q},\tau)$ is

$$
\begin{aligned}
\chi^0(\boldsymbol{q},i\nu_m) &= \int_0^{\beta} d\tau e^{i\nu_n\tau}\chi^0(\boldsymbol{q},i\nu_m) \\
&= -\sum_{\boldsymbol{k}}\int_0^{\beta} d\tau e^{i\nu_m\tau}G^0(\boldsymbol{k}+\boldsymbol{q},\tau)G^0(\boldsymbol{k},-\tau) \\
&= -\sum_{\boldsymbol{k}}\frac{1}{\beta}\sum_{n=-\infty}^{\infty} G^0(\boldsymbol{k}+\boldsymbol{q},i\omega_n+i\nu_n)G^0(\boldsymbol{k},i\omega_n)
\end{aligned}
\tag{3.20}
$$

With the abbreviations like $k = (\boldsymbol{k}, i\omega_n)$ and $\sum_k = \sum_{\boldsymbol{k}} \frac{1}{\beta} \sum_{n=-\infty}^{\infty}$, the irreducible susceptibility is written as

$$\chi^0(q) = -\sum_k G^0(k+q)G^0(k). \tag{3.21}$$

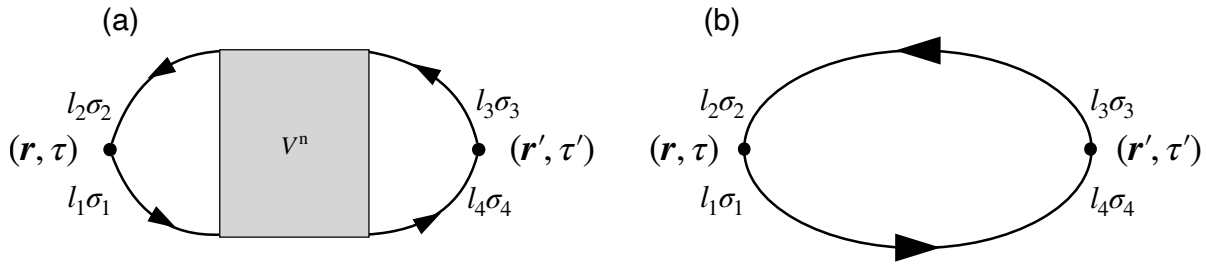


Fig.3.1: (a) Diagram of $\left\langle c^\dagger_{l_1\sigma_1} c_{l_2\sigma_2}; c^\dagger_{l_3\sigma_3} c_{l_4\sigma_4} \right\rangle$. The charge and spin susceptibilities are linear combinations of this quantity. (b) Diagram of irreducible susceptibility $\chi^0_{l_1\sigma_1, l_2\sigma_2; l_3\sigma_3, l_4\sigma_4}(q)$.

### 3.1.2 Multi-orbital case

If the system has other degrees of freedom, for example, orbitals and sites, besides the Bravais lattice vectors, $\boldsymbol{R}$, and spin, the charge and spin density operators are defined as

$$\begin{aligned} \rho(x) &= \sum_l \left[ n_{l\uparrow}(x) + n_{l\downarrow}(x) \right], \\ S^z(x) &= \frac{1}{2} \sum_l \left[ n_{l\uparrow}(x) - n_{l\downarrow}(x) \right], \\ S^\pm(x) &= \sum_l \begin{cases} c^\dagger_{l\uparrow}(x) c_{l\downarrow}(x) \\ c^\dagger_{l\downarrow}(x) c_{l\uparrow}(x) \end{cases}, \end{aligned} \tag{3.22}$$

where $l$ are the degrees of freedom like orbitals and sites. Let us call $l$ just orbital here.

In such a multi-orbital case, the notation of susceptibility is changed to

$$\begin{aligned} \chi^{\mathrm{c}}(q) &= \sum_{l,l'} \chi^{\mathrm{c}}_{ll;l'l'}(q), \\ \chi^{zz}(q) &= \sum_{l,l'} \chi^{zz}_{ll;l'l'}(q), \\ \chi^{\mathrm{tr.}}(q) &= \sum_{l,l'} \chi^{\mathrm{tr.}}_{ll;l'l'}(q), \end{aligned} \tag{3.23}$$

where

$$\begin{aligned}
\chi^{\mathrm{c}}_{l_1 l_2; l_3 l_4} &= \left\langle c^\dagger_{l_1\uparrow} c_{l_2\uparrow}; c^\dagger_{l_3\uparrow} c_{l_4\uparrow} \right\rangle + \left\langle c^\dagger_{l_1\uparrow} c_{l_2\uparrow}; c^\dagger_{l_3\downarrow} c_{l_4\downarrow} \right\rangle, \\
\chi^{zz}_{l_1 l_2; l_3 l_4} &= \left\langle c^\dagger_{l_1\uparrow} c_{l_2\uparrow}; c^\dagger_{l_3\uparrow} c_{l_4\uparrow} \right\rangle - \left\langle c^\dagger_{l_1\uparrow} c_{l_2\uparrow}; c^\dagger_{l_3\downarrow} c_{l_4\downarrow} \right\rangle, \\
\chi^{\mathrm{tr.}}_{l_1 l_2; l_3 l_4} &= \left\langle c^\dagger_{l_1\uparrow} c_{l_2\downarrow}; c^\dagger_{l_3\downarrow} c_{l_4\uparrow} \right\rangle.
\end{aligned} \tag{3.24}$$

In a non-interacting case, all of the orbital-resolved susceptibilities are equal to

$$\chi^0_{l_1 l_2; l_3 l_4}(q) = -\sum_k G^0_{l_2 l_3}(k+q) G^0_{l_4 l_1}(k). \tag{3.25}$$

## 3.2 Random phase approximation

The excited electron-hole pairs are scatterd by exchange interactions, and spin fluctuations are enhanced in general. We deal with such scattering within random phase approximation (RPA) [108–111] here.

Within RPA, we consider scattering among independent modes of electron-hole excitations. We do not consider any exchanges of momentum and frequencies among the excitations, which means that only scatterings $\chi^0(q) U \chi^0(q) U \cdots U \chi^0(q)$ are considered. Diagrammatically, bubble and ladder terms are selected as shown in Fig. 3.2.

### 3.2.1 Application of RPA to the Hubbard model

Here we apply RPA to the Hubbard model. Its interaction contribution to the Hamiltonian is

$$H_{\mathrm{int.}} = U \sum_i n_{i\uparrow} n_{i\downarrow} = U \sum_i c^\dagger_{i\uparrow} c_{i\uparrow} c^\dagger_{i\downarrow} c_{i\downarrow} \tag{3.26}$$

in the paramagnetic state. In RPA, we consider bubble and ladder diagrams. $U$ works only between different spins in the Hubbard model, and $\left\langle c_{\boldsymbol{k}\sigma}; c^\dagger_{\boldsymbol{k}\sigma'} \right\rangle_0 = \delta_{\sigma,\sigma'} G^0(\boldsymbol{k})$ in the paramagnetic state. Therefore, $\chi^{\uparrow\uparrow}$ and $\chi^{\uparrow\downarrow}$ are contributed only by the bubble diagrams, and $\chi^{+-}$ is contributed only by the ladder diagrams. Moreover, even order terms of $U$ in $\chi^{\uparrow\uparrow}$ and odd order terms of $U$ in $\chi^{\uparrow\downarrow}$ can be ignored. Finally, the considered diagrams are shown in Fig. 3.2.

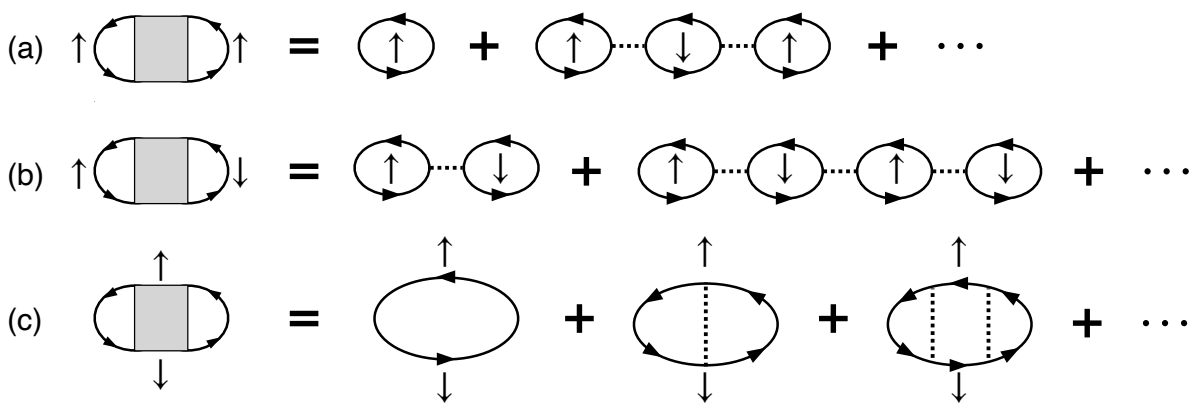


Fig.3.2: Diagrams of (a) $\chi^{\uparrow\uparrow}(q)$, (b) $\chi^{\uparrow\downarrow}(q)$ and (c) $\chi^{+-}(q)$ within the random phase approximation (RPA).

The corresponding equations are obtained with the Feynman rules as

$$
\begin{aligned}
&\chi^{\uparrow\uparrow}(q) \\
&= (-1)^1 \sum_k G(k+q)G(k) \\
&\quad + (-1)^5 \sum_{k,k',k''} G(k+q)G(k)UG(k'+q)G(k')UG(k''+q)G(k'') \\
&\quad + (-1)^9 \sum_{k_1,k_2,k_3,k_4,k_5} G(k_1+q)G(k_1)UG(k_2+q)G(k_2)UG(k_3+q)G(k_3) \\
&\qquad\qquad \times UG(k_4+q)G(k_4)UG(k_5+q)G(k_5) \\
&\quad + \cdots \\
&= \chi^0(q) + \chi^0(q)U\chi^0(q)U\chi^0(q) + \chi^0(q)U\chi^0(q)U\chi^0(q)U\chi^0(q)U\chi^0(q) + \cdots \\
&= \chi^0(q)\left\{1 + \left[U\chi^0(q)\right]^2 + \left[U\chi^0(q)\right]^4 \cdots \right\} \\
&= \frac{\chi^0(q)}{1 - \left[U\chi^0(q)\right]^2},
\end{aligned}
\tag{3.27}
$$

$$
\begin{aligned}
&\chi^{\uparrow\downarrow}(q) \\
&= (-1)^3 \sum_{k_1,k_2} G(k_1+q)G(k_1)UG(k_2+q)G(k_2) \\
&\quad + (-1)^7 \sum_{k_1,k_2,k_3,k_4} G(k_1+q)G(k_1)UG(k_2+q)G(k_2)UG(k_3+q)G(k_3)UG(k_4+q)G(k_4) \\
&\quad + \cdots \\
&= -\chi^0(q)U\chi^0(q) - \chi^0(q)U\chi^0(q)U\chi^0(q)U\chi^0(q) - \chi^0(q)U\chi^0(q)U\chi^0(q)U\chi^0(q)U\chi^0(q)U\chi^0(q) - \cdots \\
&= -\chi^0(q)U\chi^0(q)\left\{1 + \left[U\chi^0(q)\right]^2 + \left[U\chi^0(q)\right]^4 \cdots\right\} \\
&= \frac{-\chi^0(q)U\chi^0(q)}{1-\left[U\chi^0(q)\right]^2},
\end{aligned}
\tag{3.28}
$$

$$
\begin{aligned}
&\chi^{+-}(q) \\
&= (-1)^1 \sum_{k} G(k+q)G(k) + (-1)^2 \sum_{k,k'} G(k+q)G(k)UG(k'+q)G(k') \\
&\quad + (-1)^3 \sum_{k,k',k''} G(k+q)G(k)UG(k'+q)G(k')UG(k''+q)G(k'') \\
&\quad + \cdots \\
&= \chi^0(q) + \chi^0(q)U\chi^0(q) + \chi^0(q)U\chi^0(q)U\chi^0(q) + \cdots \\
&= \frac{\chi^0(q)}{1-U\chi^0(q)}.
\end{aligned}
\tag{3.29}
$$

With Eq. 3.15, the charge, longitudinal spin and transverse spin susceptibilities within RPA are obtained as follows:

$$
\begin{aligned}
\chi^{\mathrm{c}}(q) &= \chi^{\uparrow\uparrow}(q) + \chi^{\uparrow\downarrow}(q) \\
&= \frac{\chi^0(q) - \chi^0(q)U\chi^0(q)}{1-(U\chi^0(q))^2} \\
&= \frac{\chi^0(q)\left[1-U\chi^0(q)\right]}{\left[1+U\chi^0(q)\right]\left[1+U\chi^0(q)\right]} \\
&= \frac{\chi^0(q)}{1+U\chi^0(q)},
\end{aligned}
\tag{3.30}
$$

$$
\begin{aligned}
\chi^{zz}(q) &= \chi^{\uparrow\uparrow}(q) - \chi^{\uparrow\downarrow}(q) \\
&= \frac{\chi^0(q) + \chi^0(q) U \chi^0(q)}{1 - (U\chi^0(q))^2} \\
&= \frac{\chi^0(q)\left[1 + U\chi^0(q)\right]}{\left[1 + U\chi^0(q)\right]\left[1 + U\chi^0(q)\right]} \\
&= \frac{\chi^0(q)}{1 - U\chi^0(q)},
\end{aligned}
\tag{3.31}
$$

$$
\begin{aligned}
\chi^{\mathrm{tr.}}(q) &= \chi^{+-}(q) \\
&= \frac{\chi^0(q)}{1 - U\chi^0(q)}.
\end{aligned}
\tag{3.32}
$$

The obtained spin susceptibilities meet the condition $\chi^{zz}(q) = \chi^{\mathrm{tr.}}(q)$.

### 3.2.2 Application of RPA to the multi-orbital Hubbard model

We apply RPA to the multi-orbital Hubbard model with the following interaction part of the Hamiltonian:

$$
\begin{aligned}
H_{\mathrm{int.}} = &\frac{U}{2} \sum_i \sum_l \sum_\sigma n_{il\sigma} n_{il\bar{\sigma}} + \frac{V}{2} \sum_i \sum_{l \neq m} n_{il} n_{im} \\
&- \frac{J}{2} \sum_i \sum_{l \neq m} \boldsymbol{S}_{il} \cdot \boldsymbol{S}_{im} + \frac{J'}{2} \sum_i \sum_{l \neq m} \sum_\sigma c^\dagger_{il\sigma} c^\dagger_{il\bar{\sigma}} c_{im\bar{\sigma}} c_{im\sigma}
\end{aligned}
\tag{3.33}
$$

The first term, intra-orbital Coulomb interaction, is

$$
\begin{aligned}
&\frac{U}{2} \sum_i \sum_l \sum_\sigma n_{il\sigma} n_{il\bar{\sigma}} \\
&= U \sum_i \sum_l n_{il\uparrow} n_{il\downarrow} \\
&= U \sum_i \sum_l c^\dagger_{il\uparrow} c_{il\uparrow} c^\dagger_{il\downarrow} c_{il\downarrow}.
\end{aligned}
\tag{3.34}
$$

The second term, inter-orbital Coulomb interaction, is

$$\begin{aligned}
&\frac{V}{2}\sum_i\sum_{l\neq m} n_{il}n_{im} \\
&= \frac{V}{2}\sum_i\sum_{l\neq m}(n_{il\uparrow}+n_{il\downarrow})(n_{im\uparrow}+n_{im\downarrow}) \\
&= V\sum_i\sum_{l\neq m}(n_{il\uparrow}n_{im\uparrow}+n_{il\uparrow}n_{im\downarrow}) \\
&= V\sum_i\sum_{l\neq m}(c^\dagger_{il\uparrow}c_{il\uparrow}c^\dagger_{im\uparrow}c_{im\uparrow}+c^\dagger_{il\uparrow}c_{il\uparrow}c^\dagger_{im\downarrow}c_{im\downarrow}).
\end{aligned} \tag{3.35}$$

The third term, Hund's rule coupling, is

$$\begin{aligned}
&-\frac{J}{2}\sum_i\sum_{l\neq m}\boldsymbol{S}_{il}\cdot\boldsymbol{S}_{im} \\
&= -\frac{J}{4}\sum_i\sum_{l\neq m}(2c^\dagger_{il\uparrow}c_{il\downarrow}c^\dagger_{im\downarrow}c_{im\uparrow}+c^\dagger_{il\uparrow}c_{il\uparrow}c^\dagger_{im\uparrow}c_{im\uparrow}-c^\dagger_{il\uparrow}c_{il\uparrow}c^\dagger_{im\downarrow}c_{im\downarrow}) \\
&= -\frac{J}{4}\sum_i\sum_{l\neq m}(\frac{J}{2}c^\dagger_{il\uparrow}c_{im\uparrow}c^\dagger_{im\downarrow}c_{il\downarrow}-\frac{J}{4}c^\dagger_{il\uparrow}c_{il\uparrow}c^\dagger_{im\uparrow}c_{im\uparrow}+\frac{J}{4}c^\dagger_{il\uparrow}c_{il\uparrow}c^\dagger_{im\downarrow}c_{im\downarrow}).
\end{aligned} \tag{3.36}$$

The fourth term, pair hopping, is

$$\begin{aligned}
&\frac{J'}{2}\sum_i\sum_{l\neq m}\sum_\sigma c^\dagger_{il\sigma}c^\dagger_{il\bar{\sigma}}c_{im\bar{\sigma}}c_{im\sigma} \\
&= J'\sum_i\sum_{l\neq m}c^\dagger_{il\uparrow}c^\dagger_{il\downarrow}c_{im\downarrow}c_{im\uparrow} \\
&= J'\sum_i\sum_{l\neq m}c^\dagger_{il\uparrow}c_{im\uparrow}c^\dagger_{il\downarrow}c_{im\downarrow}.
\end{aligned} \tag{3.37}$$

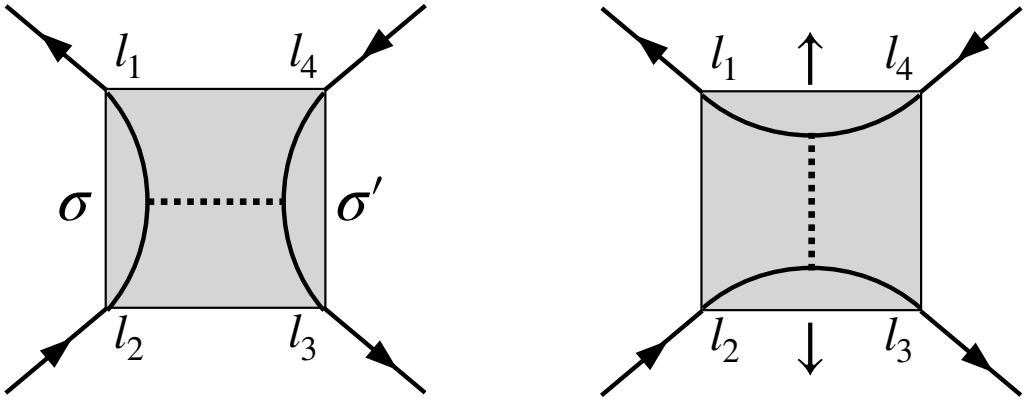


Fig.3.3: Diagrams of bare interactions, $U^{\sigma\sigma'}_{l_1 l_2; l_3 l_4}$ and $U^{+-}_{l_1 l_2; l_3 l_4}$.

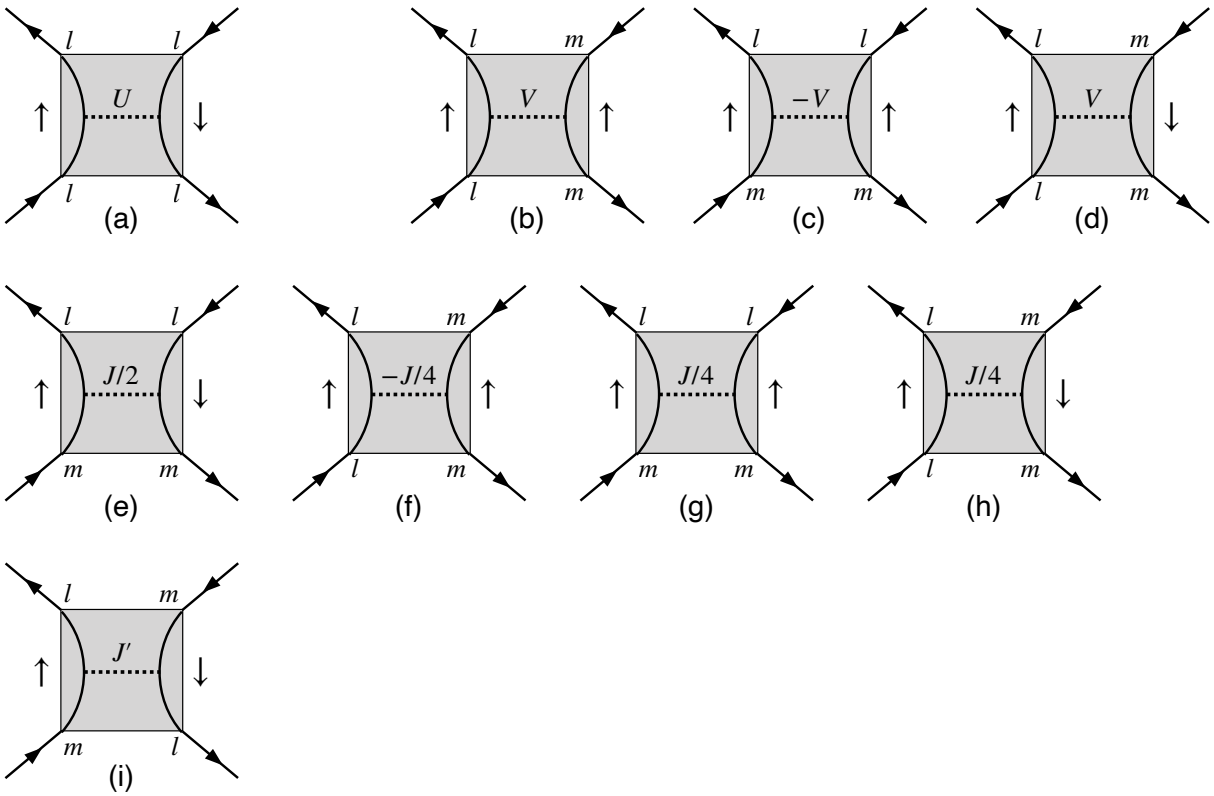


Fig.3.4: Diagrams of bare interactions, $U^{\sigma\sigma'}_{l_1 l_2; l_3 l_4}$, of the extended multi-orbital Hubbard model. (a) The intra-orbital Coulomb interaction in Eq. (3.34), (b,c) the first and (d) second terms of the inter-orbital Coulomb interaction in Eq. (3.35), (e) the first, (f,g) second and (h) third terms of the Hund's rule coupling interaction in Eq. (3.36)and (i) the pair hopping interaction in Eq. (3.37).

These interactions work between densities not only of different spins but also of same spins, unlike the case of the single-orbital Hubbard model. Moreover, the interactions depend on orbitals. We define bare interaction tensors, $U^{\sigma\sigma'}_{l_1l_2;l_3l_4}$ and $U^{+-}_{l_1l_2;l_3l_4}$, as shown in Fig. 3.3. Elements of $U_{\uparrow\uparrow}$ and $U_{\uparrow\downarrow}$ are decided by Eqs. (3.34), (3.35), (3.36) and (3.37) as

$$\begin{aligned} U^{\uparrow\downarrow}_{ll;ll} &= U, \quad U^{\uparrow\downarrow}_{ll;mm} = V + \frac{J}{4}, \quad U^{\uparrow\downarrow}_{lm;ml} = \frac{J}{2}, \qquad U^{\uparrow\downarrow}_{lm;lm} = J', \\ U^{\uparrow\uparrow}_{ll;mm} &= V - \frac{J}{4}, \quad U^{\uparrow\uparrow}_{lm;ml} = -V + \frac{J}{4}. \end{aligned} \tag{3.38}$$

Elements of $\hat{U}^{+-}$ can be obtained with

$$U^{+-}_{l_1l_2;l_3l_4} = -U^{\uparrow\downarrow}_{l_1l_4;l_3l_2}, \tag{3.39}$$

where the minus sign results from an exchange of creation and annihilation operators.

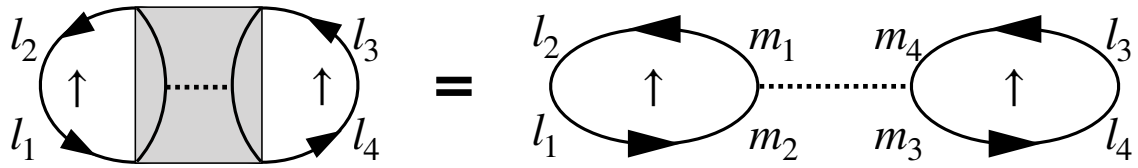


Fig.3.5: Diagrams of the second-order terms of $\chi^{\uparrow\uparrow}$. $l_1$, $l_2$, $l_3$ and $l_4$ are orbital indices of $\chi^{\uparrow\uparrow(1)}$. $m_1$, $m_2$, $m_3$ and $m_4$ are orbital indices summed in this calculation.

The bare interactions scatter $\chi^0$. As an example, let us consider the second-order terms of $\chi^{\uparrow\uparrow}$ shown in Fig. 3.5. The corresponding equation is

$$\chi^{\uparrow\uparrow(1)}_{l_1l_2;l_3l_4} = -\sum_{m_1,m_2,m_3,m_4} \chi^0_{l_1l_2;m_1m_2} U^{\uparrow\uparrow}_{m_1m_2;m_3m_4} \chi^0_{m_3m_4;l_3l_4}. \tag{3.40}$$

This equation can be written as

$$\hat{\chi}^{\uparrow\uparrow(1)} = -\hat{\chi}^0 \hat{U}^{\uparrow\uparrow} \hat{\chi}^0 \tag{3.41}$$

where the matrix multiplication is defined as

$$(\hat{A}\hat{B})_{ab;cd}(q) = \sum_{e,f} A_{ab;ef}(q) B_{ef;cd}(q) \tag{3.42}$$

for general matrices, $\hat{A}$ and $\hat{B}$ and orbital indices, $a$, $b$, $c$, $d$, $e$ and $f$. We use this notation in the following multiplications of $\chi$ and $U$.

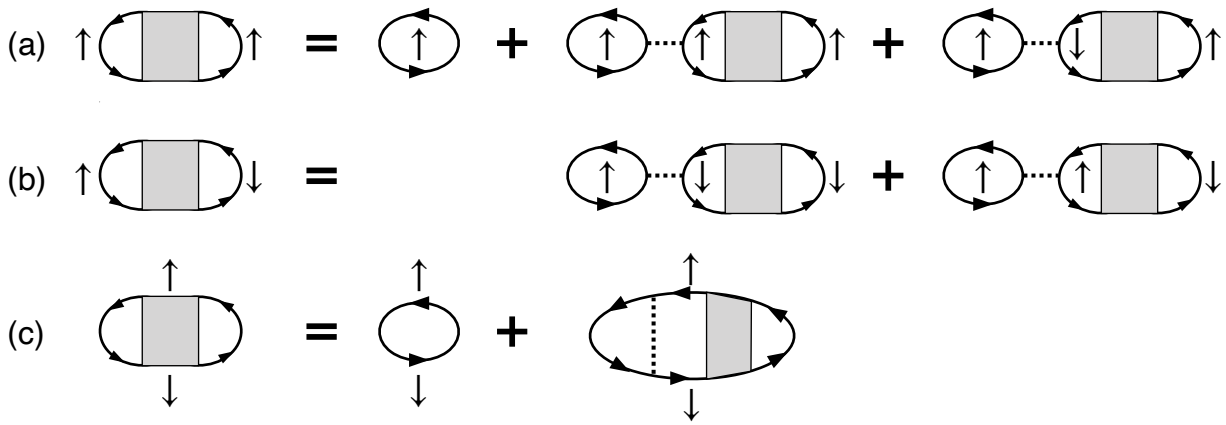


Fig.3.6: Diagrams of generalized susceptibility within random phase approximation (RPA). (a) $\hat{\chi}^{\uparrow\uparrow}(q)$, (b) $\hat{\chi}^{\uparrow\downarrow}(q)$ and (c) $\hat{\chi}^{+-}(q)$.

The susceptibilities have combinations of spins as shown in Fig. 3.6 due to the combination of spins in the bare interactions. Corresponding equations are

$$\hat{\chi}^{\uparrow\uparrow}(q) = \hat{\chi}^{0}(q) - \hat{\chi}^{0}(q)\hat{U}^{\uparrow\downarrow}\hat{\chi}^{\downarrow\uparrow}(q) - \hat{\chi}^{0}(q)\hat{U}^{\uparrow\uparrow}\hat{\chi}^{\uparrow\uparrow}(q), \tag{3.43}$$

$$\hat{\chi}^{\uparrow\downarrow}(q) = -\hat{\chi}^{0}(q)\hat{U}^{\uparrow\downarrow}\hat{\chi}^{\downarrow\downarrow}(q) - \hat{\chi}^{0}(q)\hat{U}^{\uparrow\uparrow}\hat{\chi}^{\uparrow\downarrow}(q), \tag{3.44}$$

$$\hat{\chi}^{+-}(q) = \hat{\chi}^{0}(q) - \hat{\chi}^{0}(q)\hat{U}^{+-}\hat{\chi}^{+-}(q). \tag{3.45}$$

Therefore, the charge and spin susceptibilities are

$$\begin{aligned}
\hat{\chi}^{\mathrm{c}}(q) &= \hat{\chi}^{\uparrow\uparrow}(q) + \hat{\chi}^{\uparrow\downarrow}(q) \\
&= \hat{\chi}^{0}(q) - \hat{\chi}^{0}(q)\hat{U}^{\uparrow\downarrow}[\hat{\chi}^{\downarrow\downarrow}(q) + \hat{\chi}^{\downarrow\uparrow}(q)] - \hat{\chi}^{0}(q)\hat{U}^{\uparrow\uparrow}[\hat{\chi}^{\uparrow\uparrow}(q) + \hat{\chi}^{\uparrow\downarrow}(q)] \\
&= \hat{\chi}^{0}(q) - \hat{\chi}^{0}(q)\hat{U}^{\uparrow\downarrow}\hat{\chi}^{\mathrm{c}}(q) - \hat{\chi}^{0}(q)\hat{U}^{\uparrow\uparrow}\hat{\chi}^{\mathrm{c}}(q) \\
&= \hat{\chi}^{0}(q) - \hat{\chi}^{0}(q)\left(\hat{U}^{\uparrow\downarrow} + \hat{U}^{\uparrow\uparrow}\right)\hat{\chi}^{\mathrm{c}}(q) \\
&= \hat{\chi}^{0}(q) - \hat{\chi}^{0}(q)\hat{U}^{\mathrm{c}}\hat{\chi}^{\mathrm{c}}(q),
\end{aligned} \tag{3.46}$$

$$\begin{aligned}
\hat{\chi}^{\mathrm{s}}(q) &= \hat{\chi}^{zz}(q) \\
&= \hat{\chi}^{\uparrow\uparrow}(q) - \hat{\chi}^{\uparrow\downarrow}(q) \\
&= \hat{\chi}^{0}(q) + \hat{\chi}^{0}(q)\hat{U}^{\uparrow\downarrow}[\hat{\chi}^{\downarrow\downarrow}(q) - \hat{\chi}^{\downarrow\uparrow}(q)] - \hat{\chi}^{0}(q)\hat{U}^{\uparrow\uparrow}[\hat{\chi}^{\uparrow\uparrow}(q) - \hat{\chi}^{\uparrow\downarrow}(q)] \\
&= \hat{\chi}^{0}(q) + \hat{\chi}^{0}(q)\hat{U}^{\uparrow\downarrow}\hat{\chi}^{\mathrm{s}}(q) - \hat{\chi}^{0}(q)\hat{U}^{\uparrow\uparrow}\hat{\chi}^{\mathrm{s}}(q) \\
&= \hat{\chi}^{0}(q) + \hat{\chi}^{0}(q)\left(\hat{U}^{\uparrow\downarrow} - \hat{U}^{\uparrow\uparrow}\right)\hat{\chi}^{\mathrm{s}}(q) \\
&= \hat{\chi}^{0}(q) + \hat{\chi}^{0}(q)\hat{U}^{\mathrm{s}}\hat{\chi}^{zz}(q),
\end{aligned} \tag{3.47}$$

Note that $\hat{U}^{\rm c}$ and $\hat{U}^{\rm s}$ are defined as $\hat{U}^{\rm c}_{\rm s} = \hat{U}^{\uparrow\downarrow} \pm \hat{U}^{\uparrow\uparrow}$ so that the above equations have the same form with the single-orbital case like $\hat{\chi}^{\rm c}_{\rm s}(q) = \hat{\chi}^0(q) \mp \hat{\chi}^0(q)\hat{U}^{\rm c}_{\rm s}\hat{\chi}^{\rm c}_{\rm s}(q)$.

Elements of $\hat{U}^{\rm c}_{\rm s} = \hat{U}^{\uparrow\downarrow} \pm \hat{U}^{\uparrow\uparrow}$ are

$$\begin{aligned} U^{\rm c}_{ll;ll} &= U, \quad U^{\rm c}_{ll;mm} = 2V, \quad U^{\rm c}_{lm;ml} = -V + \frac{3}{4}J, \quad U^{\rm c}_{lm;lm} = J', \\ U^{\rm s}_{ll;ll} &= U, \quad U^{\rm s}_{ll;mm} = \frac{J}{2}, \quad U^{\rm s}_{lm;ml} = V + \frac{J}{4}, \quad U^{\rm s}_{lm;lm} = J'. \end{aligned} \tag{3.48}$$

Note that the bare interaction, $\hat{U}^{+-}$, has a relation,

$$U^{+-}_{l_1l_2;l_3l_4} = -U^{\uparrow\downarrow}_{l_1l_4;l_3l_2} = -U^{\rm s}_{l_1l_2;l_3l_4}, \tag{3.49}$$

and the transverse spin susceptibility is

$$\begin{aligned} \hat{\chi}^{\rm tr.}(q) &= \hat{\chi}^{+-}(q) \\ &= \hat{\chi}^0(q) - \hat{\chi}^0(q)\hat{U}^{+-}\hat{\chi}^{+-}(q) \\ &= \hat{\chi}^0(q) + \hat{\chi}^0(q)\hat{U}^{\rm s}\hat{\chi}^{+-}(q). \end{aligned} \tag{3.50}$$

This equation is equivalent to the longitudinal spin susceptibility (Eq. (3.47)), Therefore, Eq. (3.14) is fulfilled here.

Note that the interaction parameters, $U$, $V$, $J$ and $J'$, are sometimes defined differently. Our notation can be compared as

$$\tilde{U} = U, \quad \tilde{U'} = V + \frac{J}{4}, \quad \tilde{J} = \frac{J}{2}, \quad \tilde{J'} = J', \tag{3.51}$$

where $\tilde{U}$, $\tilde{U'}$, $\tilde{J}$ and $\tilde{J'}$ are the interaction parameters denoted in Refs. [112, 113].

## 3.3 Fluctuation exchange approximation

In general, the electronic structure and thus the electron Green's function are renormalized by the electronic correlations mediated by the spin and charge fluctuations. In the fluctuation exchange (FLEX) approximation [114, 115], we replace $G^0(k)$ by $G(k)$, which is the Green's function renormalized as

$$G_{ll'}(k) = G^0_{ll'}(k) + G^0_{lm}(k)\Sigma^{\rm FLEX}_{mm'}(k)G_{m'l'}(k) \tag{3.52}$$

This equation can be written as

$$\hat{G}(k) = \hat{G}^0(k) + \hat{G}^0(k)\hat{\Sigma}^{\rm FLEX}(k)\hat{G}(k) \tag{3.53}$$

with a notation of matrix multiplications,

$$\left(\hat{A}\hat{B}\right)_{ll'}(k) = \sum_{m} \left(\hat{A}(k)\right)_{lm} \left(\hat{B}(k)\right)_{ml'}. \tag{3.54}$$

The self-energy is obtained with the four-point vertex, $V^{\mathrm{n,FLEX}}$, of the particle-hole channel as

$$\Sigma^{\mathrm{FLEX}}_{l_1 l_2}(k) = \sum_{l'_1 l'_2} \sum_{q} V^{\mathrm{n,\,FLEX}}_{l_1 l'_1; l'_2 l_2}(q) G_{l'_1 l'_2}(k-q). \tag{3.55}$$

The Green's functions are renormalized by the self-energy with the RPA-like diagrams, therefore FLEX is also called renormalized-RPA.

While RPA tends to overestimates the fluctuations and the transition temperature, FLEX shows better estimates since correlation effects on the one-particle Green's functions are taken into account. Moreover, FLEX is a conserving approximation, which is an approximation consistent with microscopic conservation laws for particle number, momentum and energy since it is generated following Baym and Kadanoff's treatments [116, 117].

### 3.3.1 Application of FLEX to the Hubbard model

We consider the diagrams in Fig. 3.7. As seen in Eq. (3.26), the Coulomb interaction $U$ works only between different spins. Therefore, the bubble terms have only contributions of even order of $U$. The self-energy is

$$\Sigma^{\mathrm{FLEX}}(k) = \Sigma^{\mathrm{b}}(k) + \Sigma^{\mathrm{l}}(k) - \Sigma^{(2)}(k) \tag{3.56}$$

with the bubble terms,

$$\Sigma^{\mathrm{b}}(k) = \sum_{q} \left\{ U\chi^0(q) + \left[U\chi^0(q)\right]^3 + \left[U\chi^0(q)\right]^5 + \cdots \right\} UG(k-q), \tag{3.57}$$

and the ladder terms,

$$\Sigma^{\mathrm{l}}(k) = \sum_{q} \left\{ U\chi^0(q) + \left[U\chi^0(q)\right]^2 + \left[U\chi^0(q)\right]^4 + \cdots \right\} UG(k-q). \tag{3.58}$$

Note that we subtract the second order terms of $U$,

$$\Sigma^{(2)}(k) = \sum_{q} U\chi^0(q) UG(k-q) \tag{3.59}$$

to avoid double counting. Note also that we ignore the Hartree term, $\Sigma^{\mathrm{H}}$, since it just shifts energy level.

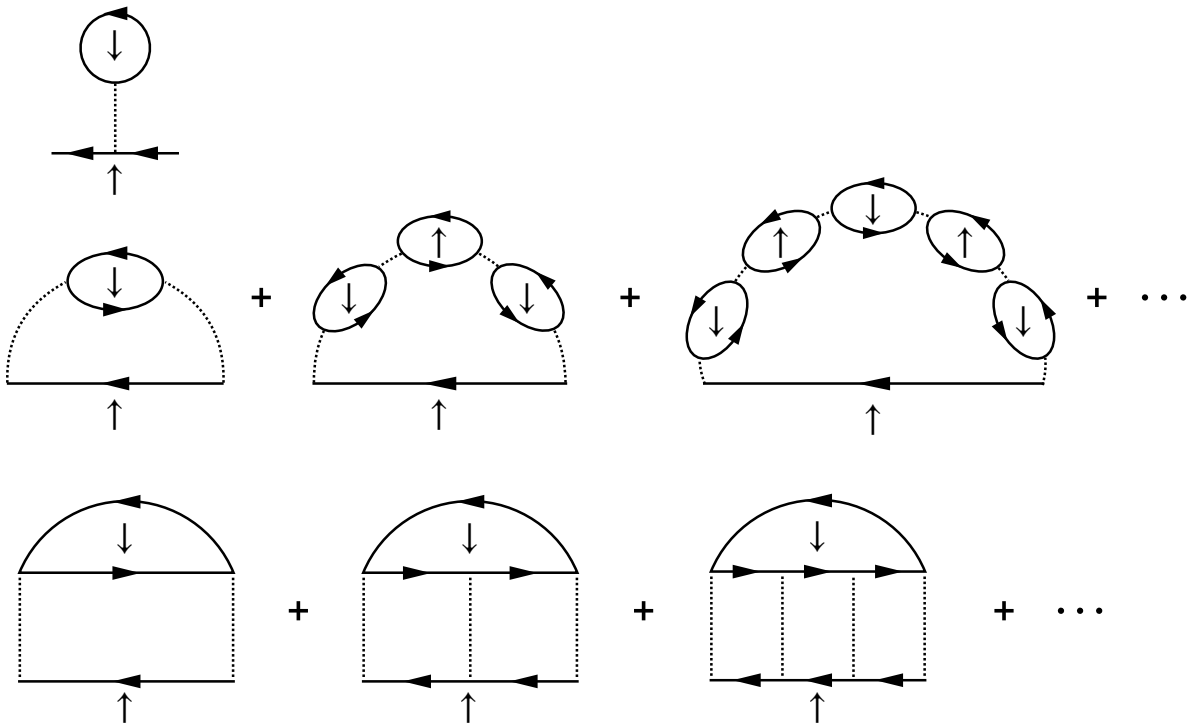

Fig.3.7: Diagrams of the self-energy considered in FLEX. Hartree term, $\Sigma^{\mathrm{H}}(k)$ (top), bubble terms, $\Sigma^{\mathrm{b}}(k)$ (middle) and ladder terms, $\Sigma^{\mathrm{l}}(k)$ (bottom).

Thus, the contributions of the four-point vertex of the particle-hole channel to the self-energy within FLEX are

$$\begin{aligned} V^{\mathrm{b}}(q) &= \left\{ U\chi^0(q) + \left[U\chi^0(q)\right]^3 + \left[U\chi^0(q)\right]^5 + \cdots \right\} U \\ &= \frac{U\chi^0(q)}{1 - \left[U\chi^0(q)\right]^2} U \\ &= \frac{1}{2} U \left[ \frac{\chi^0(q)}{1 + U\chi^0(q)} + \frac{\chi^0(q)}{1 - U\chi^0(q)} \right] U \\ &= \frac{1}{2} U\chi^{\mathrm{c}}(q) U + \frac{1}{2} U\chi^{\mathrm{s}}(q) U, \end{aligned} \tag{3.60}$$

$$
\begin{aligned}
V^{\mathrm{l}}(q) &= \left\{ U\chi^0(q) + \left[U\chi^0(q)\right]^2 + \left[U\chi^0(q)\right]^3 + \cdots \right\} U \\
&= \frac{U\chi^0(q)}{1 - U\chi^0(q)} U \\
&= U\chi^{\mathrm{s}}(q)U,
\end{aligned}
\tag{3.61}
$$

and

$$
V^{(2)}(q) = U\chi^0(q)U. \tag{3.62}
$$

The total vertex is

$$
\begin{aligned}
V^{\mathrm{n,FLEX}}(q) &= V^{\mathrm{b}}(q) + V^{\mathrm{l}}(q) - V^{(2)}(q) \\
&= \frac{1}{2}U\chi^{\mathrm{c}}(q)U + \frac{3}{2}U\chi^{\mathrm{s}}(q)U - U\chi^0(q)U.
\end{aligned}
\tag{3.63}
$$

### 3.3.2 Application of FLEX to the multi-orbital Hubbard model

In this section, we apply the FLEX approximation to the multi-orbital Hubbard model with the Hamiltonian, Eq. (3.33). We need to consider the combinations shown in Fig. 3.8 since the bare interaction also works between equal-spin densities.

$$
\hat{\Sigma}^{\mathrm{FLEX}}(k) = \hat{\Sigma}^{\mathrm{b}}(k) + \hat{\Sigma}^{\mathrm{l}}(k) - \hat{\Sigma}^{(2)}(k) \tag{3.64}
$$

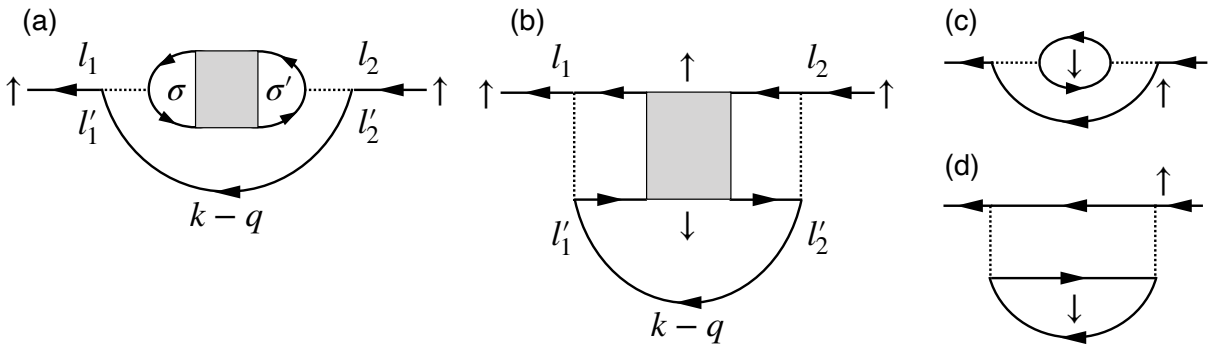


Fig.3.8: Diagrams of the self-energy. (a) bubble terms, $\hat{\Sigma}^{\mathrm{b}}(k)$, (b) ladder terms, $\hat{\Sigma}^{\mathrm{l}}(k)$, (c) the second order term of $\hat{\Sigma}^{\mathrm{b}}(k)$ and (d) the second order term of $\hat{\Sigma}^{\mathrm{l}}(k)$. Since (c) and (d) are equal, it is necessary to subtract $\hat{\Sigma}^{(2)}(k)$ to avoid double counting.

The individual terms are

$$\Sigma^{\mathrm{b}}_{l_1 l_2}(k) = \sum_{l'_1,l'_2}\sum_{q}\left[\hat{U}^{\uparrow\downarrow}\hat{\chi}^{\downarrow\downarrow}(q)\hat{U}^{\downarrow\uparrow} + \hat{U}^{\uparrow\downarrow}\hat{\chi}^{\downarrow\uparrow}(q)\hat{U}^{\uparrow\uparrow} + \hat{U}^{\uparrow\uparrow}\hat{\chi}^{\uparrow\downarrow}(q)\hat{U}^{\downarrow\uparrow} + \hat{U}^{\uparrow\uparrow}\hat{\chi}^{\uparrow\uparrow}(q)\hat{U}^{\uparrow\uparrow}\right]_{l_1 l'_1; l'_2 l_2} \times G_{l'_1 l' 2}(k-q), \tag{3.65}$$

$$\Sigma^{\mathrm{l}}_{l_1 l_2}(k) = \sum_{l'_1,l'_2}\sum_{q}\left[\hat{U}^{+-}\hat{\chi}^{+-}(q)\hat{U}^{+-}\right]_{l_1 l'_1; l'_2 l_2} G_{l'_1 l' 2}(k-q), \tag{3.66}$$

$$\Sigma^{(2)}_{l_1 l_2}(k) = \sum_{l'_1,l'_2}\sum_{q}\left[\hat{U}^{\uparrow\downarrow}\hat{\chi}^{0}(q)\hat{U}^{\downarrow\uparrow}\right]_{l_1 l'_1; l'_2 l_2} G_{l'_1 l' 2}(k-q), \tag{3.67}$$

where $\Sigma^{(2)}$ is subtracted in order to avoid double counting. The corresponding four-point vertices of the particle-hole channel to the self-energy are

$$\begin{aligned}
\hat{V}^{\mathrm{b}}(q) &= \hat{U}^{\uparrow\downarrow}\hat{\chi}^{\downarrow\downarrow}(q)\hat{U}^{\downarrow\uparrow} + \hat{U}^{\uparrow\downarrow}\hat{\chi}^{\downarrow\uparrow}(q)\hat{U}^{\uparrow\uparrow} + \hat{U}^{\uparrow\uparrow}\hat{\chi}^{\uparrow\downarrow}(q)\hat{U}^{\downarrow\uparrow} + \hat{U}^{\uparrow\uparrow}\hat{\chi}^{\uparrow\uparrow}(q)\hat{U}^{\uparrow\uparrow} \\
&= \frac{1}{2}\hat{U}^{\mathrm{c}}\hat{\chi}^{\mathrm{c}}(q)\hat{U}^{\mathrm{c}} + \frac{1}{2}\hat{U}^{\mathrm{s}}\hat{\chi}^{\mathrm{s}}(q)\hat{U}^{\mathrm{s}}, \\
\hat{V}^{\mathrm{l}}(q) &= \hat{U}^{+-}\hat{\chi}^{+-}(q)\hat{U}^{+-} \\
&= \hat{U}^{\mathrm{s}}\hat{\chi}^{\mathrm{s}}(q)\hat{U}^{\mathrm{s}}, \\
\hat{V}^{(2)}(q) &= \hat{U}^{\uparrow\downarrow}\hat{\chi}^{0}(q)\hat{U}^{\uparrow\downarrow} \\
&= \frac{1}{4}\left(\hat{U}^{\mathrm{c}} + \hat{U}^{\mathrm{s}}\right)\hat{\chi}^{0}(q)\left(\hat{U}^{\mathrm{c}} + \hat{U}^{\mathrm{s}}\right),
\end{aligned} \tag{3.68}$$

where we use the relations, $\hat{U}^{\uparrow\uparrow} = \hat{U}^{\downarrow\downarrow}$, $\hat{U}^{\uparrow\downarrow} = \hat{U}^{\downarrow\uparrow}$, $\hat{U}^{\mathrm{c}}_{\mathrm{s}} = \hat{U}^{\uparrow\downarrow} \pm \hat{U}^{\uparrow\uparrow}$ and $\hat{\chi}^{\mathrm{c}}_{\mathrm{s}} = \hat{\chi}^{\uparrow\uparrow} \pm \hat{\chi}^{\uparrow\downarrow}$. Therefore, the four-point vertex within FLEX is

$$\begin{aligned}
\hat{V}^{\mathrm{n,FLEX}}(q) &= \hat{V}^{\mathrm{b}}(q) + \hat{V}^{\mathrm{l}}(q) - \hat{V}^{(2)}(q) \\
&= \frac{1}{2}\hat{U}^{\mathrm{c}}\hat{\chi}^{\mathrm{c}}(q)\hat{U}^{\mathrm{c}} + \frac{3}{2}\hat{U}^{\mathrm{s}}\hat{\chi}^{\mathrm{s}}(q)\hat{U}^{\mathrm{s}} - \frac{1}{4}\left[\hat{U}^{\mathrm{c}} + \hat{U}^{\mathrm{s}}\right]\hat{\chi}^{0}(q)\left[\hat{U}^{\mathrm{c}} + \hat{U}^{\mathrm{s}}\right].
\end{aligned} \tag{3.69}$$

# Chapter 4

# Microscopic theory of superconductivity

## 4.1 Dyson-Gor'kov equation

In the superconducting state, not only normal Green's functions $G_{\alpha_1\alpha_2}(\boldsymbol{k}, i\omega_n)$, but also anomalous Green's functions, $F_{\alpha_1\alpha_2}(\boldsymbol{k}, i\omega_n)$, are defined [118].

$$G_{\alpha_1\alpha_2}(x;x') = -\left\langle T_\tau c_{\alpha_1}(x) c^\dagger_{\alpha_2}(x') \right\rangle \tag{4.1}$$

$$F_{\alpha_1\alpha_2}(x;x') = -\left\langle T_\tau c_{\alpha_1}(x) c_{\alpha_2}(x') \right\rangle \tag{4.2}$$

$$F^\dagger_{\alpha_1\alpha_2}(x;x') = -\left\langle T_\tau c^\dagger_{\alpha_1}(x) c^\dagger_{\alpha_2}(x') \right\rangle \tag{4.3}$$

Their Fourier transforms are

$$\begin{aligned} G_{\alpha_1\alpha_2}(\boldsymbol{k}, i\omega_n) &= \sum_{\boldsymbol{R},\boldsymbol{R}'} e^{-i\boldsymbol{k}\cdot(\boldsymbol{R}-\boldsymbol{R}')} \int_0^\beta d\tau e^{i\omega_n\tau} G_{\alpha_1\alpha_2}(x;x') \\ &= -\int_0^\beta d\tau e^{i\omega_n\tau} \left\langle T_\tau \sum_{\boldsymbol{R}} e^{-i\boldsymbol{k}\cdot\boldsymbol{R}} c_{\alpha_1}(\boldsymbol{R},\tau) \sum_{\boldsymbol{R}'} e^{-i\boldsymbol{k}\cdot\boldsymbol{R}'} c^\dagger_{\alpha_2}(\boldsymbol{R}',0) \right\rangle \\ &= -\int_0^\beta d\tau e^{i\omega_n\tau} \left\langle T_\tau c_{\boldsymbol{k}\alpha_1}(\tau) c^\dagger_{\boldsymbol{k}\alpha_2} \right\rangle \end{aligned} \tag{4.4}$$

$$
\begin{aligned}
F_{\alpha_1\alpha_2}(\boldsymbol{k}, i\omega_n) &= \sum_{\boldsymbol{R},\boldsymbol{R}'} e^{-i\boldsymbol{k}\cdot(\boldsymbol{R}-\boldsymbol{R}')} \int_0^\beta d\tau e^{i\omega_n\tau} F_{\alpha_1\alpha_2}(x;x') \\
&= -\int_0^\beta d\tau e^{i\omega_n\tau} \left\langle T_\tau \sum_{\boldsymbol{R}} e^{-i\boldsymbol{k}\cdot\boldsymbol{R}} c_{\alpha_1}(\boldsymbol{R},\tau) \sum_{\boldsymbol{R}'} e^{-i(-\boldsymbol{k})\cdot\boldsymbol{R}'} c_{\alpha_2}(\boldsymbol{R}',0) \right\rangle \\
&= -\int_0^\beta d\tau e^{i\omega_n\tau} \left\langle T_\tau c_{\boldsymbol{k}\alpha_1}(\tau) c_{-\boldsymbol{k}\alpha_2} \right\rangle
\end{aligned}
\tag{4.5}
$$

$$
\begin{aligned}
F^\dagger_{\alpha_1\alpha_2}(\boldsymbol{k}, i\omega_n) &= \sum_{\boldsymbol{R},\boldsymbol{R}'} e^{-i\boldsymbol{k}\cdot(\boldsymbol{R}-\boldsymbol{R}')} \int_0^\beta d\tau e^{i\omega_n\tau} F^\dagger_{\alpha_1\alpha_2}(x;x') \\
&= -\int_0^\beta d\tau e^{i\omega_n\tau} \left\langle T_\tau \sum_{\boldsymbol{R}} e^{i(-\boldsymbol{k})\cdot\boldsymbol{R}} c^\dagger_{\alpha_1}(\boldsymbol{R},\tau) \sum_{\boldsymbol{R}'} e^{i\boldsymbol{k}\cdot\boldsymbol{R}'} c^\dagger_{\alpha_2}(\boldsymbol{R}',0) \right\rangle \\
&= -\int_0^\beta d\tau e^{i\omega_n\tau} \left\langle T_\tau c^\dagger_{-\boldsymbol{k}\alpha_1}(\tau) c^\dagger_{\boldsymbol{k}\alpha_2} \right\rangle
\end{aligned}
\tag{4.6}
$$

where $\langle\cdots\rangle$ is the statistical average, $T_\tau$ is the time-ordered product of imaginary time $\tau$, $\alpha_i$ are quantum numbers including orbital $l$ and spin $\sigma$, and $c_{\boldsymbol{k}\alpha}$ ($c^\dagger_{\boldsymbol{k}\alpha}$) is an annihilation (creation) operator for electrons with wave vector $\boldsymbol{k}$ and quantum number $\alpha$. $c_{\boldsymbol{k}\alpha}(\tau) = e^{H\tau} c_{\boldsymbol{k}\alpha} e^{-H\tau}$ is an annihilation operator at imaginary time $\tau$ in the Heisenberg picture.

We define the matrix form of the Green's functions as

$$
\begin{aligned}
\hat{G}(k) &= \begin{pmatrix} G_{11}(k) & G_{12}(k) & G_{13}(k) & \cdots \\ G_{21}(k) & G_{22}(k) & G_{23}(k) & \cdots \\ G_{31}(k) & G_{32}(k) & G_{33}(k) & \cdots \\ \vdots & \vdots & \vdots & \ddots \end{pmatrix} \\
\hat{F}(k) &= \begin{pmatrix} F_{11}(k) & F_{12}(k) & F_{13}(k) & \cdots \\ F_{21}(k) & F_{22}(k) & F_{23}(k) & \cdots \\ F_{31}(k) & F_{32}(k) & F_{33}(k) & \cdots \\ \vdots & \vdots & \vdots & \ddots \end{pmatrix},
\end{aligned}
\tag{4.7}
$$

The Green's functions are expressed with the Dyson-Gor'kov equation [118] as

$$
\begin{pmatrix} \hat{G}(k) & \hat{F}(k) \\ \hat{F}^\dagger(k) & -\hat{G}(-k) \end{pmatrix} = \begin{pmatrix} (\hat{G}^0)^{-1}(k) - \hat{\Sigma}(k) & \hat{\Delta}(k) \\ \hat{\Delta}^*(k) & -(\hat{G}^0)^{-1}(-k) + \hat{\Sigma}(-k) \end{pmatrix}^{-1}. \tag{4.8}
$$

$\Sigma(k)$ and $\Delta(k)$ are the normal and anomalous self-energies, $\hat{G}^0(k)$ is the non-interacting Green's function. This equation corresponds to the Dyson equation in normal states, and it is expressed in diagrams as shown in Fig. 4.1.

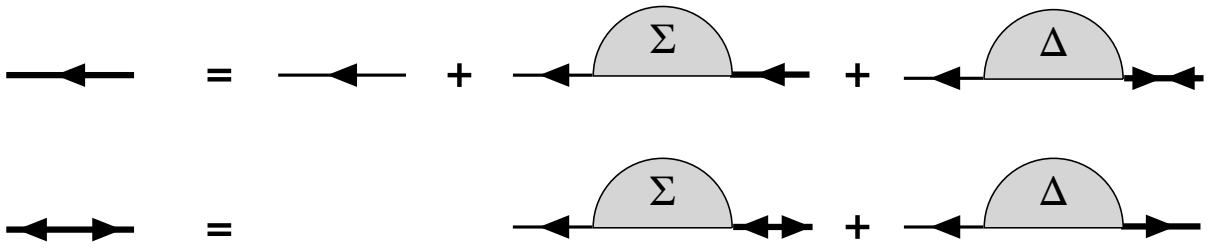


Fig.4.1: Diagrams of the Dyson-Gor'kov equation.

## 4.2 Eliashberg equation

The anomalous self-energy is given by the Eliashberg equation [119],

$$\Delta_{ll'}(k) = -\sum_{m,m'}\sum_{k'} V^{\mathrm{a}}_{lm;l'm'}(k,k')F_{mm'}(k'), \tag{4.9}$$

whose diagram is shown in Fig. 4.2 (a). This is a self-consistent equation for the anomalous self-energy $\Delta(k)$ since the anomalous Green's function $F(k')$ is related to $\Delta(k')$ by the Dyson-Gor'kov equation (4.8). The anomalous Green's function is defined as $\langle c_{\boldsymbol{k}}; c_{-\boldsymbol{k}}\rangle$, which is very similar definition to the mean field in BCS theory. In fact, the Eliashberg equation is an extension of the gap equation (1.17) in BCS theory. The anomalous self-energy $\Delta(k)$ corresponds to the superconducting order parameter $\Delta(\boldsymbol{k})$ in BCS theory, and the electron-electron channel four-point vertex (anomalous vertex) $V^{\mathrm{a}}(k,k')$ corresponds to the pairing interaction $V(\boldsymbol{k},\boldsymbol{k}')$ in BCS theory.

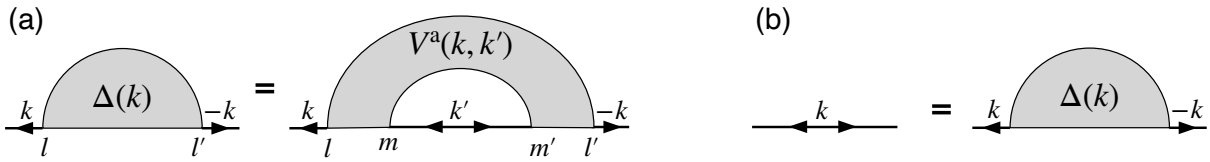


Fig.4.2: Diagrams of (a) the Eliashberg equation and (b) the linearized anomalous Green's function.

We take the limit $\Delta \to 0$ and linearize the Eliashberg equation. This is justified at

$T = T_{\mathrm{c}}$. First, the Dyson-Gor'kov equation is linearized as

$$\begin{aligned}
&\begin{pmatrix} \hat{G}(k) & \hat{F}(k) \\ \hat{F}^{\dagger}(k) & -\hat{G}(-k) \end{pmatrix} \\
&= \begin{pmatrix} \underbrace{\hat{G^0}^{-1}(k) - \hat{\Sigma}(k)}_{\equiv \tilde{G}^{-1}(k)} & \hat{\Delta}(k) \\ \hat{\Delta}^*(k) & \underbrace{-\hat{G^0}^{-1}(-k) + \hat{\Sigma}(-k)}_{\equiv -\tilde{G}^{-1}(-k)} \end{pmatrix} \\
&= \begin{pmatrix} \tilde{G}(k) + \tilde{G}(k)\hat{\Delta}(k)\hat{S}^{-1}(k)\hat{\Delta}^*(k)\tilde{G}(k) & -\tilde{G}(k)\hat{\Delta}(k)\hat{S}^{-1}(k) \\ -\hat{S}^{-1}(k)\hat{\Delta}^*(k)\tilde{G}(k) & \hat{S}^{-1}(k) \end{pmatrix} \\
&\approx \begin{pmatrix} \tilde{G}(k) & \tilde{G}(k)\hat{\Delta}(k)\tilde{G}(-k) \\ \tilde{G}(-k)\hat{\Delta}^*(k)\tilde{G}(k) & -\tilde{G}(-k) \end{pmatrix}.
\end{aligned} \tag{4.10}$$

Therefore, the Green's functions are

$$\begin{cases} \hat{G}(k) &= \tilde{G}(k) = \left[\hat{G^0}^{-1}(k) - \hat{\Sigma}(k)\right] \\ \hat{F}(k) &= \hat{G}(-k)\hat{\Delta}(k)\hat{G}(k) \end{cases}. \tag{4.11}$$

We substitute the linearized anomalous Green's function in the Eliashberg equation, and we obtain the linearized Eliashberg equation.

$$\begin{aligned}
\Delta_{ll'}(k) &= -\sum_{m,m'}\sum_{k'} V^{\mathrm{a}}_{ll';mm'}(k,k')\left[\hat{G}(-k)\hat{\Delta}(k')\hat{G}(k')\right]_{mm'} \\
&= -\sum_{m,m'}\sum_{k'} V^{\mathrm{a}}_{ll';mm'}(k,k')\sum_{n,n'} G_{mn}(-k')\Delta_{nn'}(k')G_{n'm'}(k')
\end{aligned} \tag{4.12}$$

To solve this equation, we would need to calculate $\Delta(k)$ self-consistently. However, this comes at very high calculational cost. We introduce a parameter $\lambda$ ($0 \leq \lambda \leq 1$) as

$$\begin{aligned}
\lambda\Delta_{ll'}(k) &= \sum_{n,n'}\sum_{k'}\left[-\sum_{m,m'} V^{\mathrm{a}}_{ll';mm'}(k,k')G_{mn}(-k')G_{n'm'}(k')\right]\Delta_{nn'}(k') \\
&= \sum_{n,n'}\sum_{k'} K(ll',k;nn',k')\Delta_{nn'}(k').
\end{aligned} \tag{4.13}$$

Only when $\lambda = 1$, this equation is equivalent to the linearized Eliashberg equation, and thus $T = T_{\mathrm{c}}$. By introducing a vector $\vec{\Delta}$, whose components are $\Delta_{ll'}(\boldsymbol{k})$ and a matrix $\hat{K}$, whose components are $K(ll',k;nn',k')$, the linearized Eliashberg equation becomes

$$\lambda\vec{\Delta} = \hat{K}\vec{\Delta}, \tag{4.14}$$

which is an eigenvalue equation with the huge kernel $K$. We solve the eigenvalue equation numerically and obtain some of the solutions, which belong to the largest eigenvalues. The superconducting state with the largest eigenvalue will be realized in the system. The kernel $K$ has temperature dependences, therefore $\lambda$ (and also $\Delta$) changes as temperature changes. We determine $\lambda$ and $\Delta$ starting from high temperature and proceeding to lower and lower temperatures. Then, we decide $T_{\rm c}$.

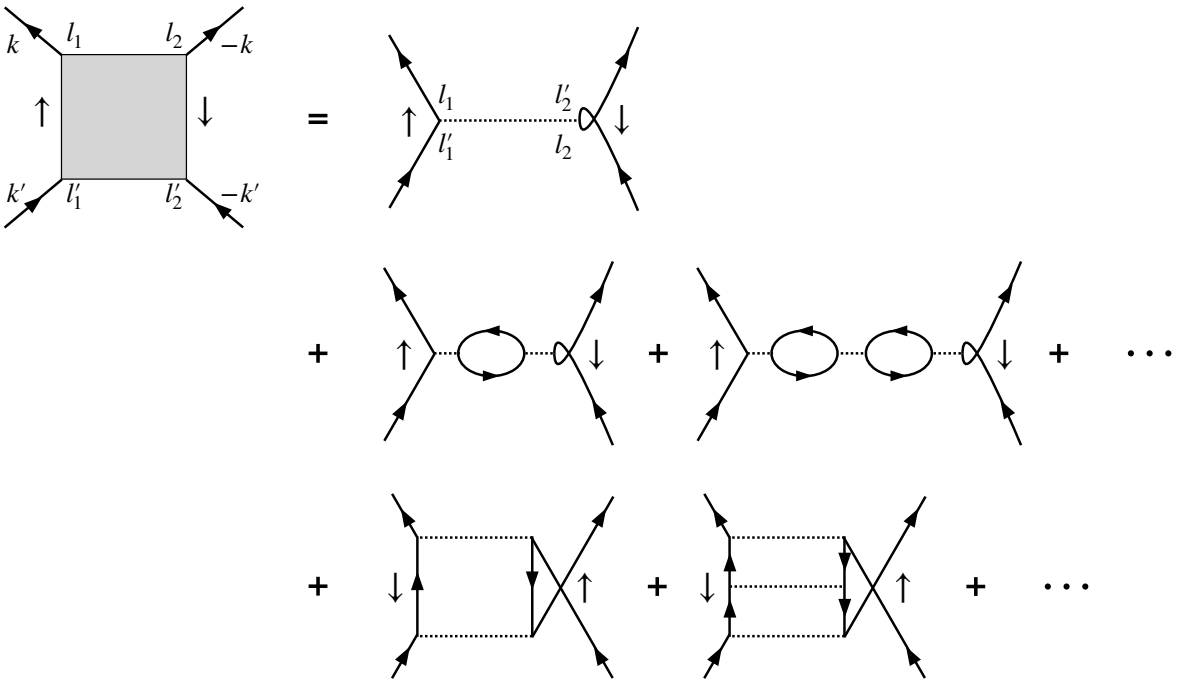


Fig.4.3: Diagrams of the anomalous vertex within RPA.

We consider superconductivity with spin-singlet pairing in this thesis. For spin-singlet superconductivity, we consider the pairing interaction, $V^{\uparrow\downarrow}$, between different spins. Diagrams of $V^{\uparrow\downarrow}$ within RPA are shown in Fig. 4.3. The corresponding equation is

$$\begin{aligned} V^{\rm a}_{ll';mm'}(k,k') = \hat{U}^{\uparrow\downarrow} + \frac{1}{2}\sum_{n_i}\Big[ & U^{\rm s}_{ll';n_1n_2}\chi^{\rm s}_{n_1n_2;n_3n_4}(k-k')U^{\rm s}_{n_3n_4;mm'} \\ & + 2U^{\rm s}_{ll'_1;n_1n_2}\chi^{\rm s}_{n_1n_2;n_3n_4}(k+k')U^{\rm s}_{n_3n_4;mm'} \\ & - U^{\rm c}_{ll'_1;n_1n_2}\chi^{\rm c}_{n_1n_2;n_3n_4}(k-k')U^{\rm c}_{n_3n_4;mm'}\Big]. \end{aligned} \tag{4.15}$$

The first term of the interaction mediated by spin fluctuations is the contribution of spin longitudinal fluctuations. The second term is the contribution of spin transverse fluctuations, and it has the factor 2. This equation can be rewritten with the matrix

multiplication introduced in Eq. (3.42).

$$\hat{V}^{\uparrow\downarrow}(k,k') = \hat{U}^{\uparrow\downarrow} + \frac{1}{2}\left[\hat{U}^{\mathrm{s}}\hat{\chi}^{\mathrm{s}}(k-k')\hat{U}^{\mathrm{s}} + 2\hat{U}^{\mathrm{s}}\hat{\chi}^{\mathrm{s}}(k+k')\hat{U}^{\mathrm{s}} - \hat{U}^{\mathrm{c}}\hat{\chi}^{\mathrm{c}}(k-k')\hat{U}^{\mathrm{c}}\right] \tag{4.16}$$

Note that $\hat{U}^{\uparrow\downarrow}$ is obtained with $\hat{U}^{\uparrow\downarrow} = (\hat{U}^{\mathrm{c}} + \hat{U}^{\mathrm{s}})/2$. For spin-singlet pairing, we also need to symmetrize the vertex in $\boldsymbol{k}$-space as

$$\hat{V}^{\mathrm{singlet}}(k,k') = \frac{1}{2}\left[\hat{V}^{\uparrow\downarrow}(k,k') + \hat{V}^{\uparrow\downarrow}(k,k')\right]. \tag{4.17}$$

We use $\hat{V}^{\mathrm{singlet}}$ for $\hat{V}^{\mathrm{a}}$ in this thesis. Within RPA, we use non-interacting Green's functions, $G^0(k)$, for all of $G(k)$ in the linearized Eliashberg equation. Within FLEX, we use the renormalized Green's function in Eq. (3.52).

# Chapter 5

# Superconducting dome in electron doped FeSe intercalates

## 5.1 Motivations

Parts of heavily electron-doped FeSe-based materials show high-$T_c$ superconductivity like $T_c = 55$ K in $Li_{0.36}(NH_3)_yFe_2Se_2$ under pressure [33], $T_c = 41$ K in $Li_x(C_6H_{16}N_2)_yFe_{2-z}Se_2$ [47] and $T_c = 30 - 46$ K in $A_xFe_2Se_2$ ($A$ = Li, Na, Ba, Sr, Ca, Yb and Eu) [120]. Superconducting mechanism of them is unclear since absence of magnetic ordering states and hole pockets around $\boldsymbol{k} = (0, 0)$ which are essential for the common spin fluctuations in iron-based superconductors is reported [52–54]. Regarding this problem, recent theoretical study [56–58] suggest that spin fluctuations mediate superconductivity with a sign-changing $s$-wave ($s_\pm$-wave hereafter) gap function even if the hole pockets are slightly below the Fermi level. Moreover, nuclear magnetic resonance (NMR) experiments [55] for FeSe intercalates suggests spin fluctuations existing and a sign-changing $s$-wave gap function in FeSe intercalates, which supports the spin fluctuations scenario. Therefore, it is reasonable to apply the spin fluctuation theory to FeSe intercalates and discuss the superconducting critical temperature and the superconducting symmetry.

In this chapter, we will focus on the lithium diaminopropane intercalated material $Li_x(C_3N_2H_{10})_{0.37}FeSe$ where charge doping has been controlled experimentally in a wide range $0.06 \leq x \leq 0.68$ [45]. $T_c$ is maximized at $x = 0.37$, and a dome in the superconducting transition temperature $T_c$ (Fig. 5.1) has been reported. This FeSe intercalate is

unique in the family of FeSe-based superconductors since superconductivity is realized in the wide range of electron-doping level from the weak coupling limit on the low doping side to the strong coupling limit on the high doping side.

## 5.2 Calculation details

We study the electronic structure of $Li_x(C_3N_2H_{10})_{0.5}FeSe$ as a function of doping by performing a series of density functional theory (DFT) calculations within the full-potential local orbital (FPLO) [121] basis, using the generalized gradient approximation (GGA) exchange correlation functional [122] and $24 \times 24 \times 24$ $k$-mesh. We construct tight-binding models including all ten Fe $3d$ orbitals using projective Wannier functions [123]. Using the glide reflection unfolding technique [10], we turn the ten-band into a five-band model. We calculate the noninteracting susceptibility $\chi_0$ on a $50 \times 50 \times 10$ $q$-mesh. We employ the random phase approximation (RPA) to calculate spin and charge susceptibilities and solve a gap equation to obtain pairing symmetry $\Delta$ and eigenvalue $\lambda$ [124, 125].

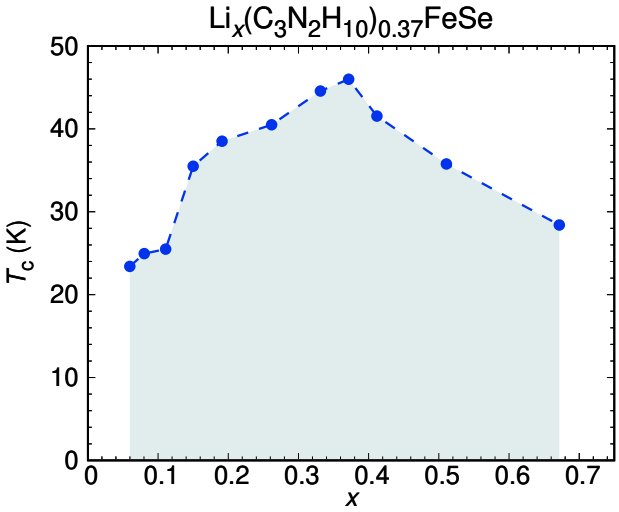


Fig.5.1: Superconducting $T_c$ of $Li_x(C_3N_2H_{10})_{0.5}FeSe$ as a function of doping, as reported in Ref. [45].

On the other hand, we use the energy mapping method to measure the exchange interactions of $Li_x(C_3N_2H_{10})_{0.5}FeSe$ [23, 126]. $2 \times 2 \times 1$ supercells with $P1$ symmetry contain eight inequivalent iron sites, allowing for 13 spin configurations with different energies.

## 5.3 Results — crystal structure —

We first generate a sequence of crystal structures for $Li_x(C_3N_2H_{10})_{0.37}FeSe$ based on the structural data determined by Sun *et al.* [45]. We smoothly interpolate the structural data for the lattice parameters and the FeSe layer and simplify the disordered

diaminopropane molecules to a single molecule per two FeSe, yielding the composition $Li_x(C_3N_2H_{10})_{0.5}FeSe$ shown in Fig. 5.2 (a). We mount the $C_3N_2H_{10}$ molecule with fixed geometry into the entire structure sequence, since bond lengths and angles of a neutral molecule should not be affected by the charging and contraction of the FeSe layer. An example of the DFT electronic structure with Fe $3d$ weights is shown in Fig. 5.2 (b). Calculations for the complete sequence of structures without diaminopropane molecule, in $P4/mnn$ symmetry, yield similar results.

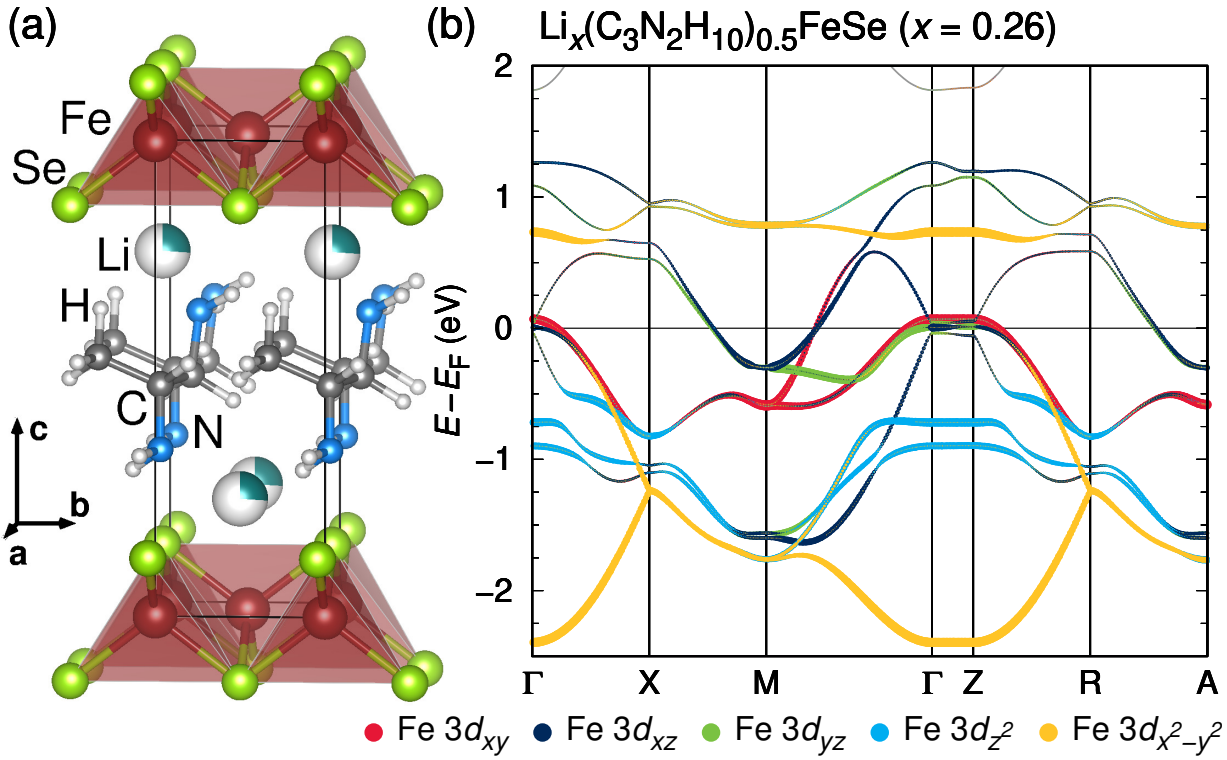


Fig.5.2: (a) Crystal structure of $Li_x(C_3N_2H_{10})_{0.5}FeSe$; the Li position is only 26% occupied, indicated by partial coloring. (b) Corresponding bands near the Fermi level $E_F$ with Fe $3d$ orbital weights.

The specific procedure is as follows. First of all, the diaminopropane molecule is placed on an $8g$ Wyckoff position of the $P42_12$ space group with partial occupancy of 0.093, leading to 0.372 $C_3N_2H_{10}$ molecules per FeSe. We simplify this structure by lowering the symmetry to $P1$ and by picking one of the eight symmetry equivalent $C_3N_2H_{10}$ molecules. This leads to the approximate stoichiometry $Li_x(C_3N_2H_{10})_{0.5}FeSe$. This structure is shown in Fig. 5.2. Note that Sun *et al.* show a very similar simplified structure [45]. The

simplification is justified because the diaminopropane molecules are important for fixing the interlayer distance; however, electronically, the highest occupied molecular orbitals are significantly below the Fermi level while the lowest unoccupied molecular orbital is slightly above the Fermi level so that the molecules are not active at the Fermi level. In order to obtain a finely spaced series of crystal structures of $Li_x(C_3N_2H_{10})_{0.5}FeSe$ as a function of doping level $x$, we interpolate the structural data provided in Ref. [45] as shown in Fig. 5.3. This guarantees that we do not incur the well-known difficulties of predicting the chalcogenide $z$ position in iron chalcogenide superconductors. Combining the diaminopropane molecule coordinates given for $x = 0.26$ with the lattice parameters of Fig. 5.3 would lead to expanded or compressed molecules as a function of doping. This would be unrealistic as the molecules remain approximately neutral over the whole doping range, and their bonds should be rigid. Therefore, we adapt the diaminopropane molecule Wyckoff positions to the changing lattice parameters, keeping all distances and angles within the molecules constant. We model the doping $x$ by using the virtual crystal approximation for Li, using a nuclear charge between neon and lithium of $Z = 2 + x$.

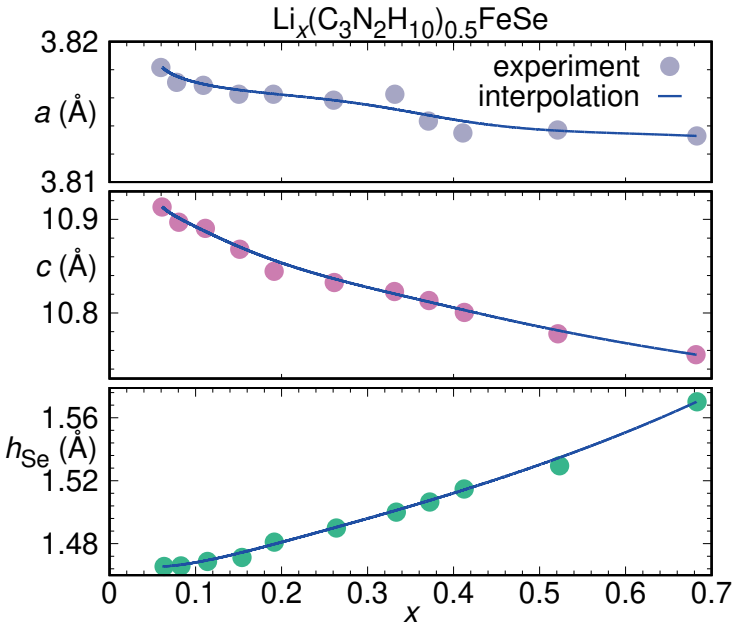


Fig.5.3: Structural parameters from Ref. [45] (symbols) and interpolation (lines). Calculations were performed for interpolated structures in steps of $\Delta x = 0.01$.

## 5.4 Results — electronic structure —

We first quantify the charge doping by integration of Fe $3d$ total and partial electron densities up to the Fermi level. We find that the charge $-xe$ provided by $Li_x^+$ is indeed fully doping the Fe plane; Fe charge evolves almost linearly from $n_{3d}^{\text{total}} = 6.06$ to 6.65 in

the interval $0.06 < x < 0.68$ (Fig. 5.4). The orbital with strongest charge increase is $d_{xy}$, followed by $d_{xz}/d_{yz}$.

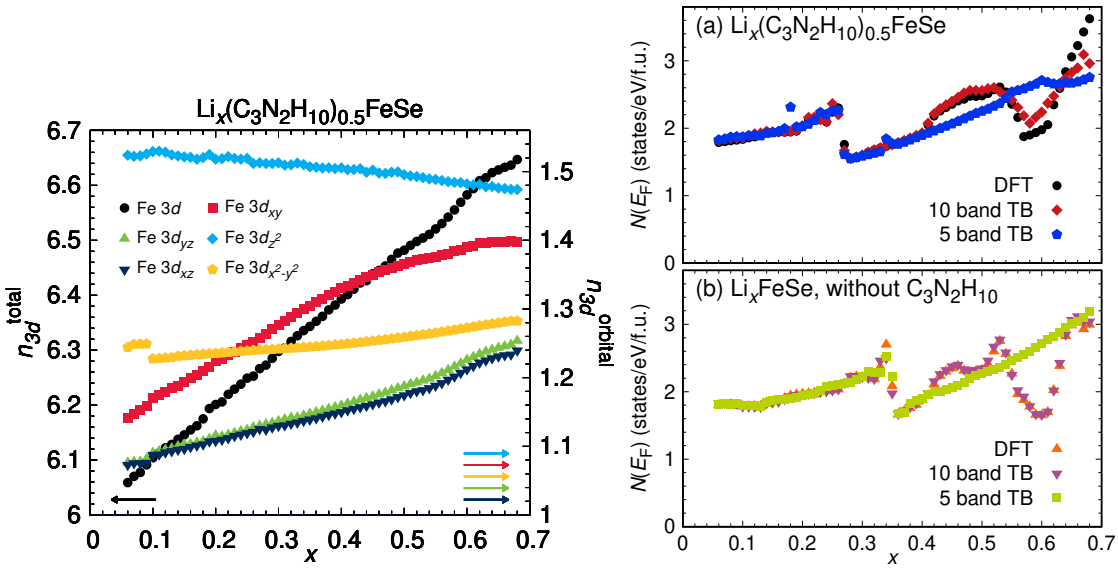


Fig.5.4: Left panel: evolution of the total and orbital resolved Fe $3d$ occupation number as a function of doping. Right panels: density of states at the Fermi level $N(E_{\rm F})$ for the two series of structures used in this study. (a) Full structure with diaminopropane molecule, (b) Li$_x$FeSe with empty van der Waals gap. $N(E_{\rm F})$ of the ten-band tight binding model faithfully represents the DFT result. On the other hand, there is some deviation for the unfolded five-band tight binding model for larger dopings, and in particular in the range $0.55 < x < 0.62$ as discussed in the main text. These deviations stem from the dopants, which lower the crystal symmetry compared to pristine FeSe, so that the unfolding to the five band model becomes only approximate.

The decisive factor in spin fluctuation theory is Fermi surfaces. We show in Fig. 5.6 the unfolded one iron Fermi surfaces of Li$_x$(C$_3$N$_2$H$_{10}$)$_{0.5}$FeSe for six doping levels. First of all, we note that the overall number and size of Fermi surface pockets are in good agreement with those observed by angle resolved photoemission in the related FeSe intercalates (Li$_{0.84}$Fe$_{0.16}$)OHFe$_{0.98}$Se and (Tl,Rb)$_x$Fe$_{2-y}$Se$_2$ (see Fig. 1 of Ref. [127]). Even though we do not know the precise doping levels of those compounds, the overall similarity in the Fermi surfaces gives us confidence that for Li$_x$(C$_3$N$_2$H$_{10}$)$_{0.5}$FeSe, we can avoid the difficulties of bulk FeSe where size and symmetry of Fermi surfaces are captured neither by DFT nor its extensions. Note, also, that DFT+DMFT, as applied in Ref. [45], has

only a small effect on the Fermi surface of $Li_x(C_3N_2H_{10})_{0.5}FeSe$. Thus, the DFT Fermi surfaces are a reasonable starting point for the description of the material.

The dominant feature in the Fermi surface evolution with doping is the strong growth of the large angular electron pockets around the $X$ and $Y$ points in the one iron Brillouin zone (BZ). They have combined $d_{xy}$ and $d_{xz}/d_{yz}$ character, respectively. The hole pocket with $d_{xy}$ character at the $M$ point in the one iron BZ is rather insensitive to doping. Finally, several Lifshitz transitions occur around Γ with doping, as expected for an iron-based superconductor and previously noted in Ref. [45]. In a doping range of $0.24 < x < 0.30$, an inner hole pocket disappears, an outer hole pocket disappears, and an electron pocket appears; all these are of $d_{xz}/d_{yz}$ character. The appearance of an electron pocket at Γ with doping has also been observed with ARPES on a potassium coated FeSe monolayer [128]. Without diaminopropane molecule, the Lifshitz transitions are spread over a range $0.17 < x < 0.38$, in reasonable agreement with the DFT calculations of Ref. [45].

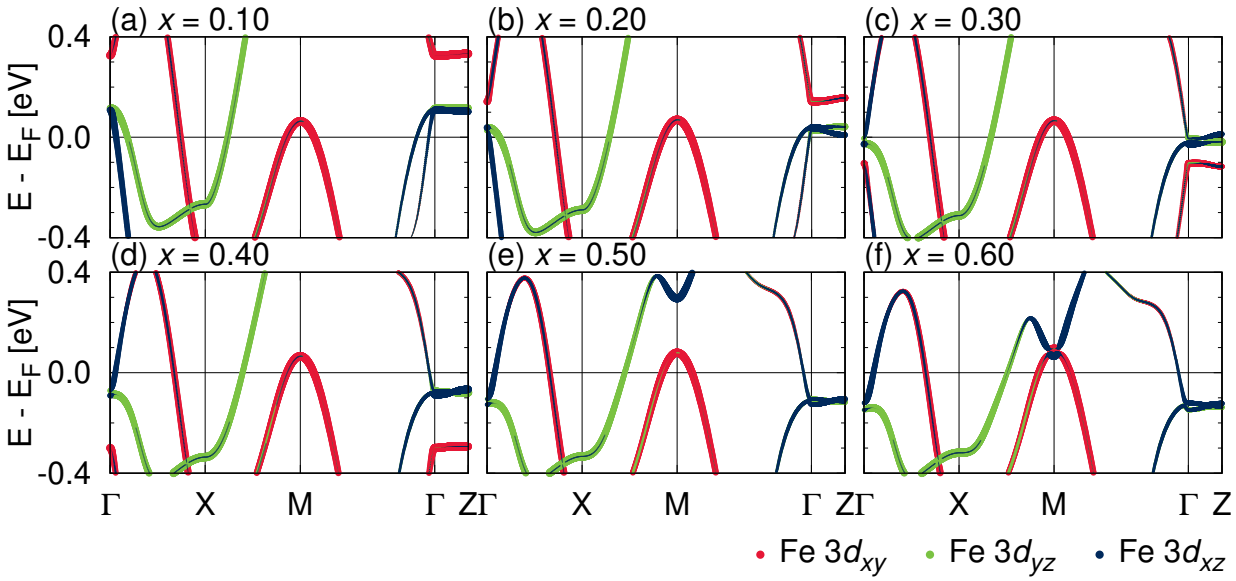


Fig.5.5: Evolution of the band structure with doping. The Fe $3d$ orbital weights are indicated by color.

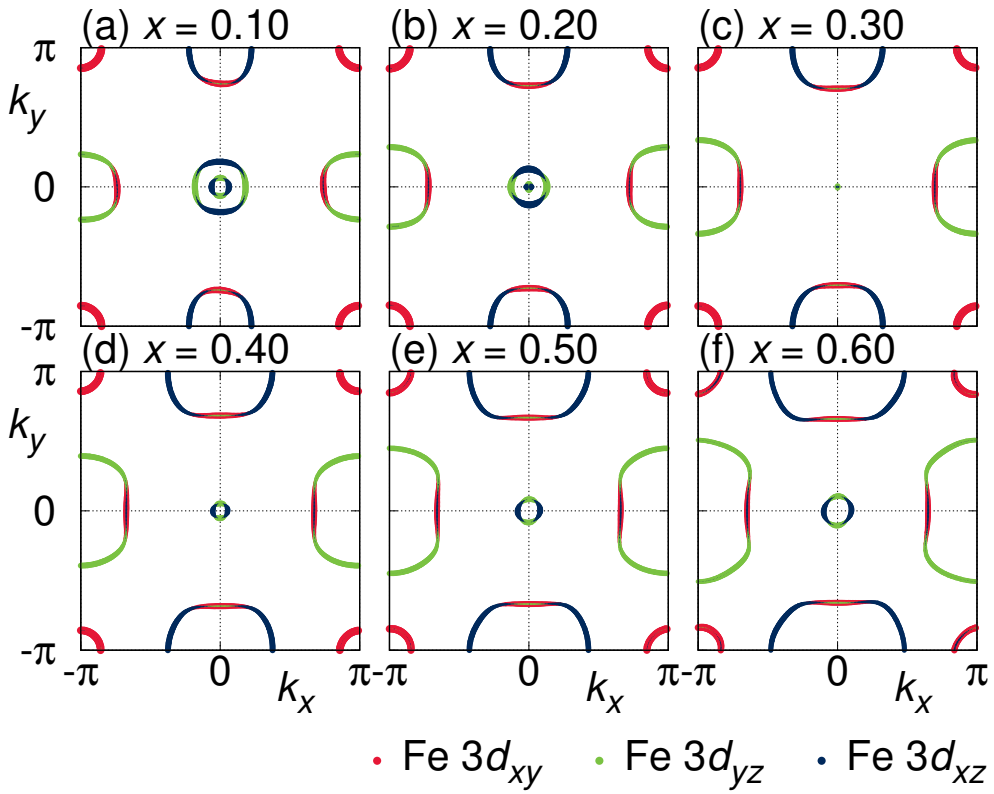


Fig.5.6: Evolution of the Fermi surface at $k_z = 0$ with doping. The Fe $3d$ orbital weights are indicated by color. Orbital weight of Fe $3d_{z^2}$ and $3d_{x^2-y^2}$ at the Fermi level is nearly negligible.

The main effect on the density of states at the Fermi level $N(E_\mathrm{F})$ (Fig. 5.4) is a 30% reduction around $x = 0.27$, which results from the disappearance of the two hole pockets; the appearance of the small electron pocket and its growth with doping helps $N(E_\mathrm{F})$ to recover.

In the series of calculations without $C_3N_2H_{10}$ molecule, we observe a doping range $0.55 < x < 0.62$, where the Fermi level is pinned to a Dirac cone. Topological properties of iron-based superconductors have recently been discussed intensively [129–132]. The presence of diaminopropane molecules in a fixed position as shown in Fig. 5.2 (a) breaks the $P4nmm$ symmetry of $Li_xFeSe$ and leads to the opening of a small gap in the Dirac cone. The high symmetry may be restored on average due to the statistical distribution of molecules in the high symmetry of the $P42_12$ space group observed experimentally. Further theory and experiments are required to determine the nature of $Li_x(C_3N_2H_{10})_{0.5}FeSe$ in the doping range $0.55 < x < 0.62$. As the unfolding does

not capture the $N(E_{\mathrm{F}})$ suppression in this doping range, we exclude it from our present discussion.

## 5.5 Results —spin susceptibility—

We now proceed to the spin fluctuation analysis by calculating the RPA spin and charge susceptibilites. As a representative example, we show in Fig. 5.6 the diagonal components $\chi^{\mathrm{s}}_{xy}$ and $\chi^{\mathrm{s}}_{yz}$ for the structures with $C_3N_2H_{10}$ molecule. At low doping, the diagonal element $\chi^{\mathrm{s}}_{xy}$ (Fig. 5.6(a)) is dominated by a peak close to $X$ and a minor peak close to $M$. These correspond to a nesting vector, $\boldsymbol{Q} = (\pi + \delta_x, 0 + \delta_y, q_z)$ connecting the electron pocket around $X/Y$ and the hole pocket around $M$ point, and a nesting vector $\boldsymbol{Q} = (\pi + \delta_x, \pi + \delta_y, q_z)$ connecting the electron pocket around $X$ and that around $Y$. Furthermore, $\chi^{\mathrm{s}}_{yz}$ has a peak around $X$, which corresponds to a nesting vector $\boldsymbol{Q} = (\pi + \delta_x, 0 + \delta_y, q_z)$ connecting the hole pocket around $\Gamma$ and the electron pocket around $X$. The nesting vectors change with $\delta_x$, $\delta_y$ because the electron pockets around $X/Y$ grow. In both cases, the susceptibility peak formerly close to $X$ progressively evolves towards $\boldsymbol{Q} = (\pi, \pi/2, q_z)$ with increasing doping. This tendency is further accentuated by the Lifshitz transition in the range $0.24 < x < 0.30$, which also rotates the orbital weights on the $d_{xz}/d_{yz}$ hole pockets around $\Gamma$ by 90 degrees.

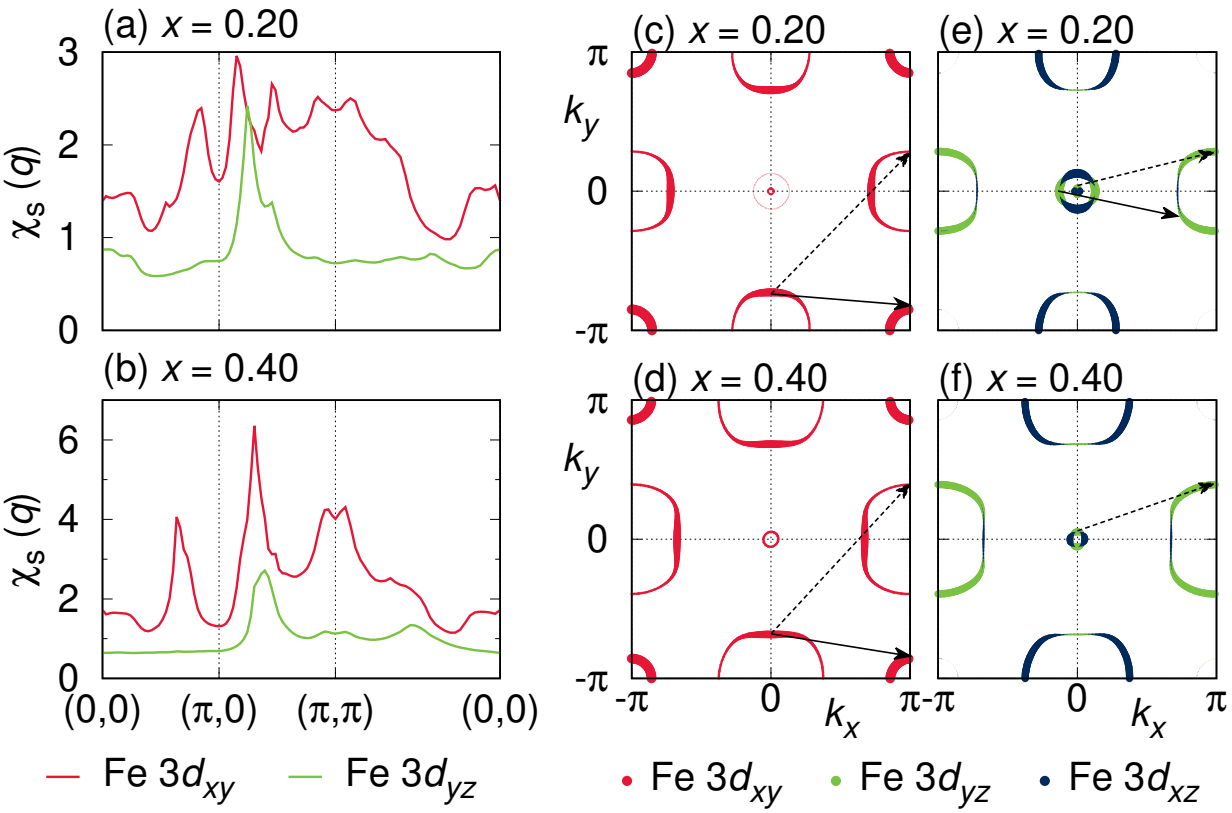


Fig.5.7: Diagonal elements of the spin susceptibility as a function of momentum vector and doping.

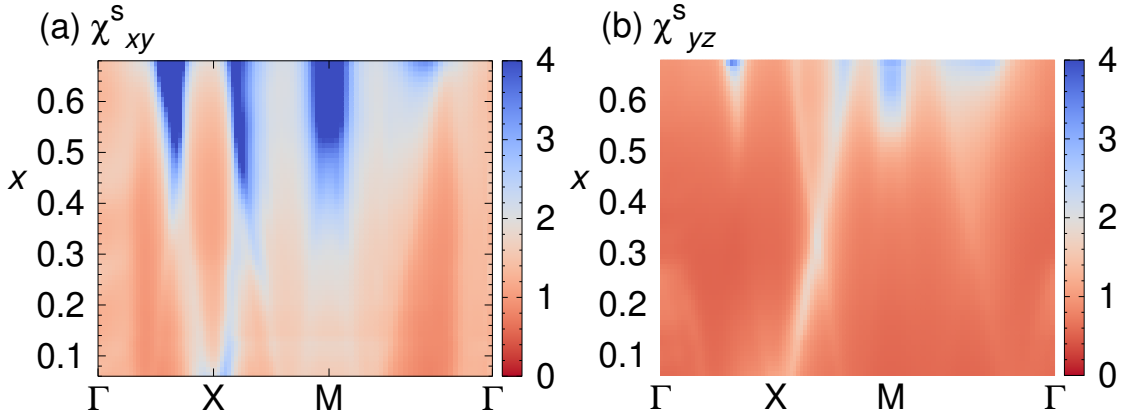


Fig.5.8: Diagonal elements of the spin susceptibility as a function of momentum vector and doping.

## 5.6 Results —Superconductivity—

Overall, we see an increase in both susceptibilities with doping. This is in line the upward trend of $N(E_F)$ which is interrupted by the loss of hole pockets around $x = 0.27$ and by the band crossing pinned to the Fermi level for $0.55 < x < 0.62$. In agreement with this observation, the trend of the eigenvalue $\lambda$ of the linearized gap equation as shown in Fig. 5.9 is an increase over the entire doping range, with the exception of $x = 0.27$ where the Lifshitz transitions cause an abrupt drop of $\lambda$. The leading instabilities are different types of sign changing $s$ wave in the whole region.

Clearly, the itinerant electron analysis of superconductivity in $Li_x(C_3N_2H_{10})_{0.5}FeSe$ presented so far can be used to explain the increasing $T_c$ up to $x = 0.37$ observed in Ref. [45] (replotted for convenience in Fig. 5.1) but not its suppression for higher doping.

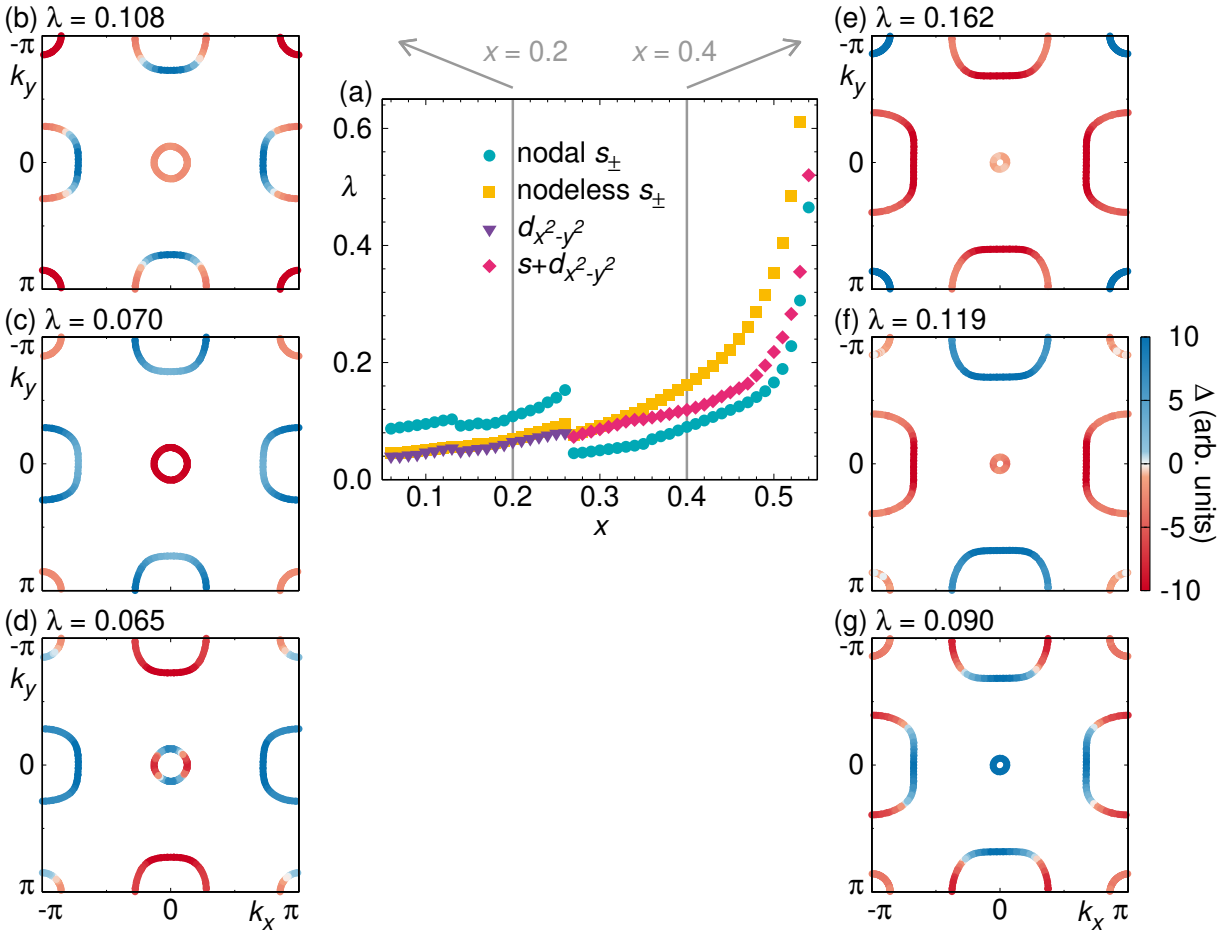


Fig.5.9: (a) Leading eigenvalues $\lambda$ of the gap equation as a function of doping level $x$ in $Li_x(C_3N_2H_{10})_{0.5}FeSe$. A jump is visible between $x = 0.26$ and $x = 0.27$, where both of the hole pockets around $\Gamma$ disappear due to a Lifshitz transition. (b)-(d) Leading gap functions on the Fermi surface at doping $x = 0.20$. (e)-(b) The same at doping $x = 0.40$.

## 5.7 Results —localized electrons analysis—

As an alternative, we now turn to the localized magnetic moment nature of the Fe $3d$ electrons to search for a mechanism to suppress superconductivity. Fig. 5.10 shows the first three in-plane exchange couplings of $Li_x(C_3N_2H_{10})_{0.5}FeSe$ determined by energy mapping. The inspection of Heisenberg Hamiltonian parameters at this point should not be confused with the assumption of a magnetic ground state; rather, the purpose here is the analysis of the nature of the spin excitations out of which superconductivity is realized. Two examples are shown in Fig. 5.11 (a) and (b). Due to the metallic

nature of the FeSe intercalate, the fit to the DFT energies is not as good as in magnetic insulatorsbut it is very reasonable as indicated by the small deviations between fitted and DFT energies and by the small error bars shown in Fig. 5.10. Note that at large doping, the bicollinear configuration takes over from stripe-type as lowest energy spin configuration (Fig. 5.11 (a) and (b)). We find a smooth evolution of exchange couplings over the entire doping range. At small doping, the system starts with all couplings antiferromagnetic, $J_2 = 0.61J_1$ and $J_3$ nearly negligible. This makes the leading magnetic instability stripe-type AFM, in perfect agreement with the weak coupling evidence of peaks at $X$ in the spin susceptibility (Fig. 5.6). As doping increases, $J_1$ decreases more rapidly than $J_2$ so that at $x = 0.33$, $J_1$ and $J_2$ coincide. This evolution strengthens the stripe-type AFM instability. However, the decrease of $J_1$ accelerates until at $x = 0.47$, $J_1$ crosses zero and becomes ferromagnetic. Meanwhile, $J_3$ is gradually increasing until at $x = 0.6$, it becomes as large as $J_2$. With FM $J_1$ and substantial AFM $J_3$, bicollinear AFM has taken over as leading magnetic instability of $Li_x(C_3N_2H_{10})_{0.5}FeSe$ (Fig. 5.11).

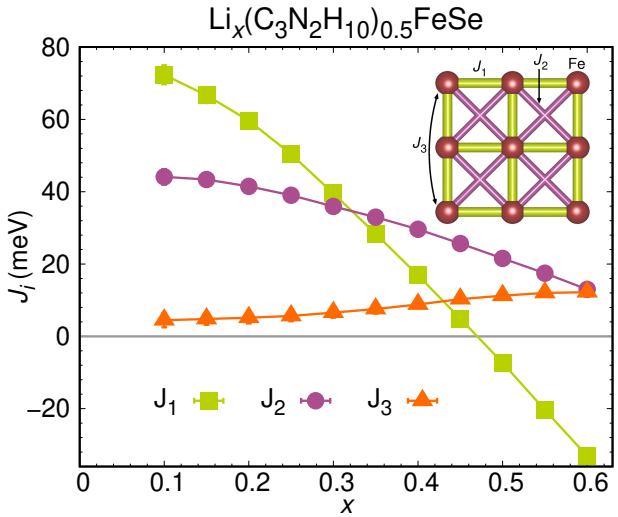


Fig.5.10: Evolution of three in-plane exchange couplings of $Li_x(C_3N_2H_{10})_{0.5}FeSe$ as a function of doping $x$, obtained from the energy mapping technique. The inset shows the three exchange paths on the iron square lattice.

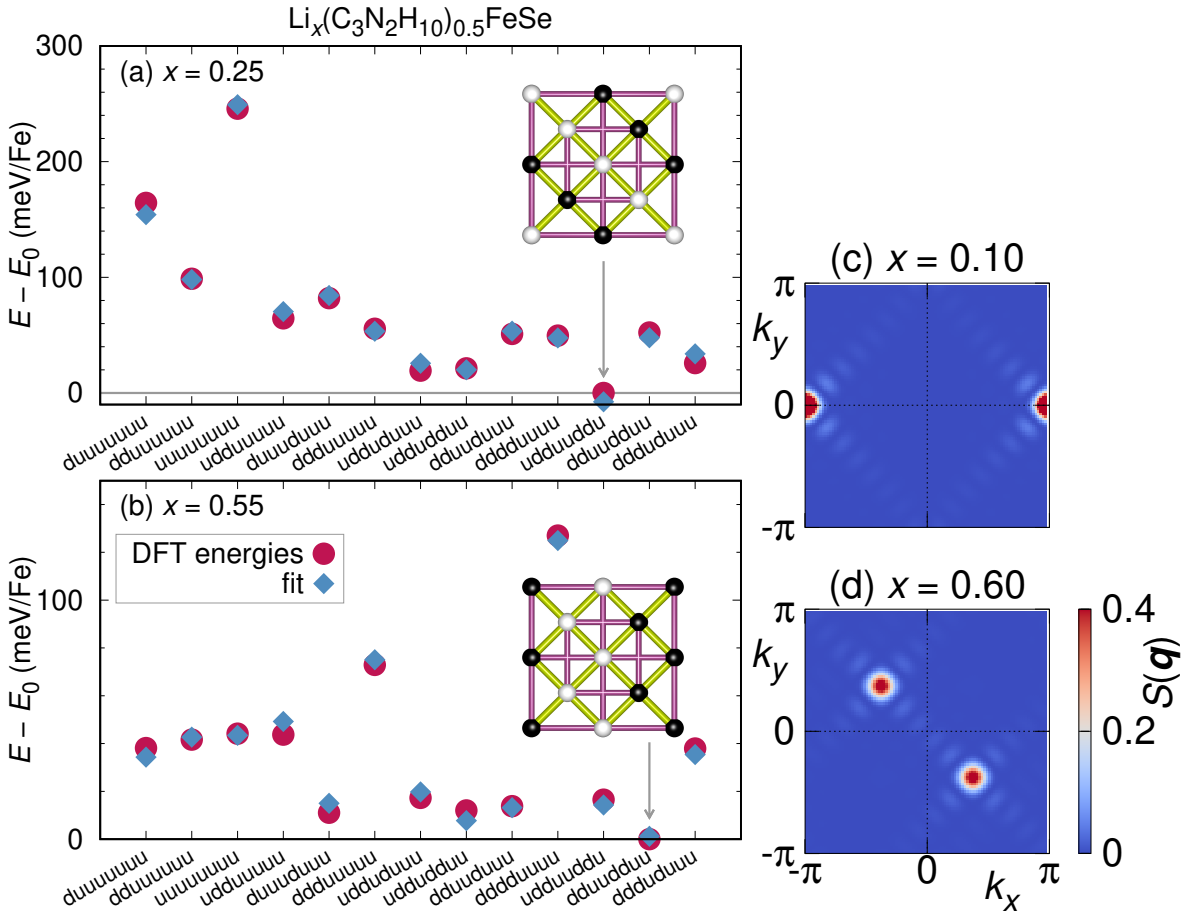


Fig.5.11: Left panels are two examples for the energy mapping of $Li_x(C_3N_2H_{10})_{0.5}FeSe$ at (a) $x = 0.25$ and (b) $x = 0.55$. In both panels the inset shows an eight iron supercell with the minimum energy spin configuration marked by white for up and black for down. Up to a doping of $x = 0.45$, the stripe-type order is lowest in energy, while from $x = 0.5$, the bicollinear order is stabilized. Right panels are spin structure factors $S(\mathbf{q})$ at $x = 0.10$ and $x = 0.60$, obtained by Fourier transforming the ground state spin configuration found with iterative minimization.

To decide and to visualize the change of magnetic tendency, we apply the iterative minimization method. The iterative minimization method allows the efficient determination of ground state spin configurations of classical spin systems.We use this method to obtain the ground states of the classical Heisenberg models with the exchange couplings in Fig. 5.10. We Fourier transform the obtained spin configurations to obtain the spin structure factor $S(\mathbf{q})$. The spin structure factors of $Li_x(C_3N_2H_{10})_{0.5}FeSe$ for doping values $x = 0.10$ and $x = 0.60$ are shown in Fig. 5.11 (c) and (d). In the doping region

of $0.10 \leq x \leq 0.45$, we find peaks at $\boldsymbol{q} = (\pi, 0)$ or $\boldsymbol{q} = (0, \pi)$, indicating stripe AFM order as ground states. On the other hand, for $0.50 \leq x \leq 0.60$, as soon as $J_1$ turns ferromagnetic, we find peaks at $\boldsymbol{Q} = (q, q)$ where $q{\sim}0.4\pi$. As it is well known that FeSe also has a substantial biquadratic coupling [22] which we do not re-determine here, the highly doped $\mathrm{Li}_x(\mathrm{C_3N_2H_{10}})_{0.5}\mathrm{FeSe}$ samples will actually be in the bicollinear phase with $\boldsymbol{q} = (\pi/2, \pi/2)$ and magnetically resemble FeTe.

The bicollinear state is the magnetic ground state of FeTe, and as optimally doped $\mathrm{FeTe}_{1-x}\mathrm{Se}_x$ has a $T_\mathrm{c}$ of only 14.5 K [133], our calculation provides a strong rationalization of the the falling $T_\mathrm{c}$ as the magnetism of $\mathrm{Li}_x(\mathrm{C_3N_2H_{10}})_{0.5}\mathrm{FeSe}$ becomes more and more like that of FeTe. We identify the ferromagnetic tendencies of the nearest neighbour exchange as the key factor for determining the $T_\mathrm{c}$ evolution on the high doping side of the superconducting dome, outplaying all weak coupling effects of growing Fermi surfaces and growing density of states at the Fermi level.

Note that a similar transition of $J_1$ from AFM to FM was found for a theoretical substitution series between iron pnictides and iron germanides [23], where superconductivity is in fact suppressed in the germanide. It is an interesting open question if the effect of ferromagnetic nearest neighbour interactions and thus a downward trend in $T_\mathrm{c}$ under electron doping could be captured in frequency dependent weak coupling methods like the fluctuation exchange approximation [18].

## 5.8 Conclusions

We have analyzed the superconductivity of $\mathrm{Li}_x(\mathrm{C_3N_2H_{10}})_{0.5}\mathrm{FeSe}$ as function of doping in the range $0.06 \leq x \leq 0.68$ both from itinerant electron and localized moment perspectives. We find that on the low doping side $x \leq 0.37$, growing Fermi surfaces and densities of states at the Fermi level are the basis for explaining growing $T_\mathrm{c}$ with spin fluctuation theory. For higher doping level, weak coupling arguments would lead to the erroneous conclusion that $T_\mathrm{c}$ should continue to grow. However, the progressive destabilization of stripe type AFM fluctuations toward bicollinear antiferromagnetism explains why $T_\mathrm{c}$ decreases for $x > 0.37$. $\mathrm{Li}_x(\mathrm{C_3N_2H_{10}})_{0.5}\mathrm{FeSe}$ turns out to be a perfect demonstration of the fact that iron-based superconductivity can only be understood by fully accounting for itinerant and localized aspects of the Fe $3d$ electrons.

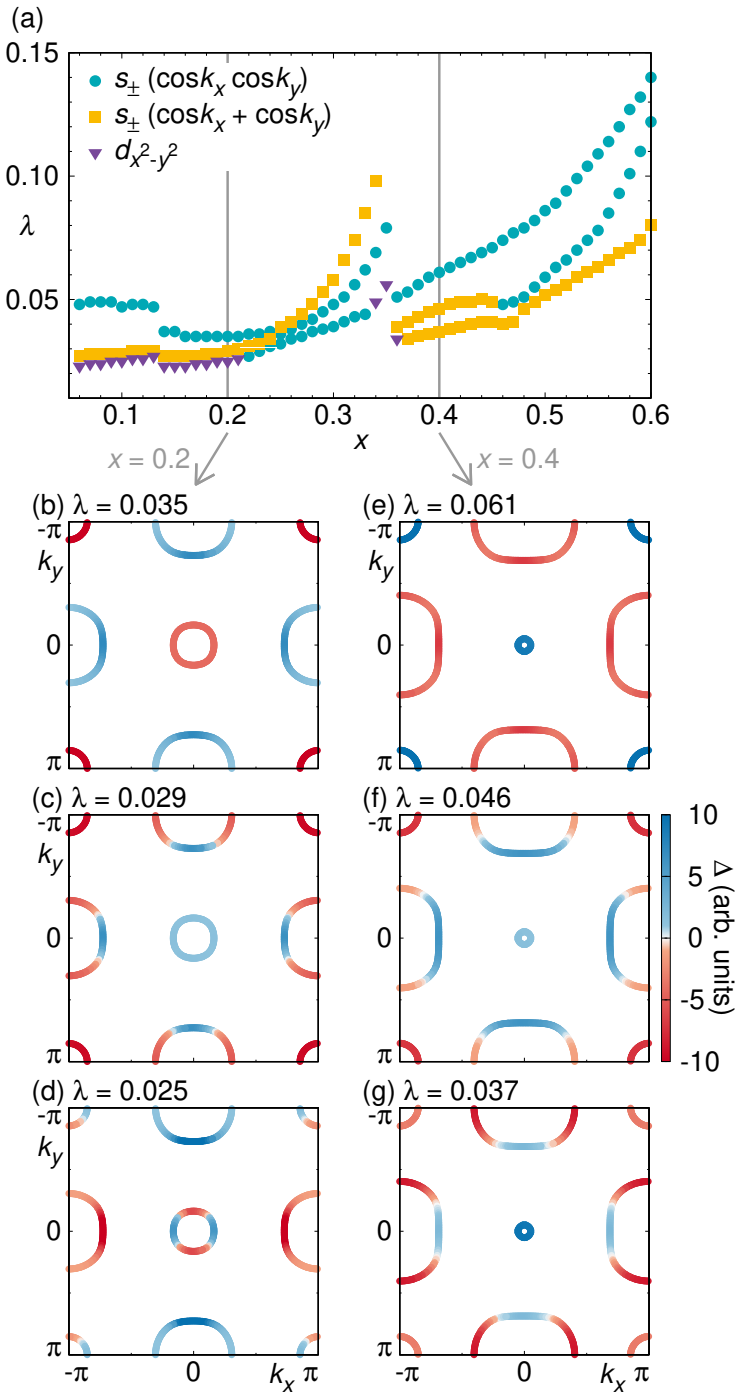


Fig.5.12: (a) Leading eigenvalues $\lambda$ of the gap equation as a function of doping level $x$ in $Li_x(C_3N_2H_{10})_{0.5}FeSe$. A jump is visible between $x = 0.35$ and $x = 0.36$, where both of the hole pockets around $\Gamma$ disappear due to a Lifshitz transition. (b)-(d) Leading gap functions on the Fermi surface at doping $x = 0.20$. (e)-(b) The same at doping $x = 0.40$. All of the results are obtained by calculations without $C_3N_2H_{10}$.

# Chapter 6

# Superconducting symmetry of $\kappa$-(BEDT-TTF) charge transfer salts

## 6.1 Motivations

The family of $\kappa$-(BEDT-TTF) charge transfer salts, abbreviated $\kappa$-$(ET)_2X$ hereafter, has the largest number of superconducting materials in organic compounds. Since the first synthesis in the 1980s, $d$-wave superconducting gap functions have been supported by experiments of nuclaer magnetic resonance (NMR) [80–83], specific heat [134], scanning tunneling spectroscopy (STS) [90], thermal conductivity [91, 135] and muon spin spectroscopy ($\mu$SR) [136]. The electronic structure of $\kappa$-$(ET)_2X$ can either be represented by a half-filled two-band model if the focus is on the $(ET)_2$ dimers (dimer model) or by a 3/4-filled four-band model if the four ET molecules are considered (molecule model). The $d$-wave gap functions have been understood by spin fluctuation theory for the dimer model [84–86] and for the molecule model [92]. However, recent experiments suggest other possibilities of gap functions like $s$-wave [94–97] and $s_\pm + d_{x^2-y^2}$-wave [97–99]. The superconducting symmetry is still controversial.

From the theoretical point of view, different symmetries of gap function in $\kappa$-$(ET)_2X$ are nearly degenerate. A FLEX study [92] for the corresponding molecule model suggests that $d_{xy}$- and $d_{x^2-y^2}$-wave gap functions are nearly degenerate related to the variation of $t_1$, which determines magnitude of the dimerization. Another RPA study [100] suggests that $d_{xy}$- and $s_\pm + d_{x^2-y^2}$-wave gap functions are nearly degenerate related to in-plane anisotropy, $t_4/t_2$ in Fig. 6.1, of the molecule model. These results give us a clue to

identify the gap function; variations of the hopping transfers $t_i$ of the molecule model have significant effects on the gap function. It is necessary to start from the specific models for every $\kappa$-$(ET)_2X$ with hopping transfers obtained by *ab initio* DFT calculations while most previous studies deal with simplified models.

Spin fluctuations affect also the electronic structure. It is possible to deal with such a self-energy mediated by spin fluctuations with FLEX. In the FLEX study [92], gap functions were calculated while assuming $d$-wave. However, there is less consensus on $d$-wave at this moment. It is necessary to fully solve a superconducting Eliashberg equation without such an assumption.

In this chapter, we identify the superconducting gap function in $\kappa$-$(ET)_2X$ with (1) starting from variations of hopping transfers obtained by *ab initio* DFT calculations for every $\kappa$-$(ET)_2X$, (2) dealing with self-energy within FLEX and (3) fully solving the linearized Eliashberg equation. We also aim to understand why $T_c$ varies from a few to a dozen Kelvins.

## 6.2 Calculation details

First, we construct eight Hubbard model with Hamiltonians,

$$H = H^0 + U \sum_{\boldsymbol{R}l} n_{\boldsymbol{R}l\uparrow} n_{\boldsymbol{R}l\downarrow} \tag{6.1}$$

where $H^0$ are tight-binding Hamiltonians,

$$H^0 = -\sum_{\boldsymbol{R},l,l'} t^{ll'}_{\boldsymbol{R}} e^{-i\boldsymbol{k}\cdot\boldsymbol{R}} + \mu \sum_{\boldsymbol{R}l\sigma} c^{\dagger}_{\boldsymbol{R}l\sigma} c_{\boldsymbol{R}l\sigma}. \tag{6.2}$$

There are four BEDT-TTF molecular sites in the unit cell. The indices, $l = 1, 2, 3, 4$, determine the sites. $t^{ll'}_{\boldsymbol{R}}$ are transfer integrals of hopping $\boldsymbol{R}$ from $l$th to $l'$th site. Combinations of the transfer integrals determine characteristics of the Hubbard models. We use the values calculated by *ab initio* density-functional-theory calculations by D. Guterding *et al.* [100]. $\mu$ are chemical potentials, which are introduced so that the models are 3/4-filled. The Coulomb interaction is fixed as $U = 400$ meV, which is positive and thus repulsive.

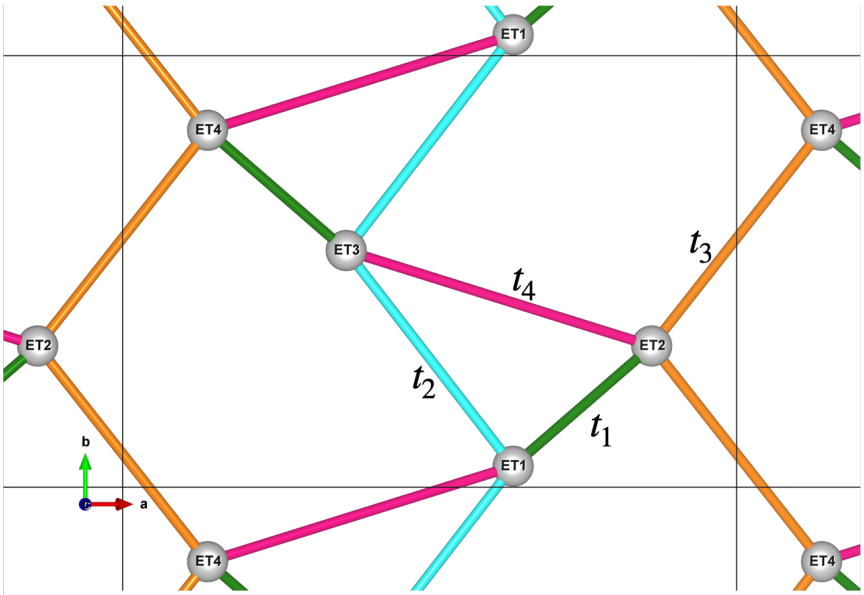


Fig.6.1: The tight-binding model of $\kappa$-$(ET)_2X$. There are four ET molecular sites in the unit cell.

| $i$ | Material | $T_c$(K) | $t_1$ | $t_2$ | $t_3$ | $t_4$ | $t_4/t_2$ |
|---|---|---|---|---|---|---|---|
| 1 | $\kappa$-$(ET)_2Ag(CF_3)_4(TCE)$ | 2.6 | 168 | 102 | 60.8 | 33.4 | 0.362 |
| 2 | $\kappa$-$(ET)_2I_3$ | 3.6 | 180 | 119 | 52.2 | 31.7 | 0.266 |
| 3 | $\kappa$-$(ET)_2Ag(CN)_2 \cdot H_2O$ | 5.0 | 185 | 104 | 60.4 | 23.6 | 0.305 |
| 4 | $\kappa$-$\alpha_1'$-$(ET)_2Ag(CF_3)_4(TCE)$ | 9.5 | 166 | 97.6 | 65.8 | 35.3 | 0.362 |
| 5 | $\kappa$-$(ET)_2Cu(NCS)_2$ | 10.4 | 190 | 102 | 82.4 | 17.5 | 0.171 |
| 6 | $\kappa$-$\alpha_2'$-$(ET)_2Ag(CF_3)_4(TCE)$ | 11.1 | 165 | 98.4 | 66.7 | 36.3 | 0.369 |
| 7 | $\kappa$-$(ET)_2Cu[N(CN)_2](CN)$ | 11.2 | 175 | 100 | 78.5 | 17.3 | 0.172 |
| 8 | $\kappa$-$(ET)_2Cu[N(CN)_2]Br$ | 11.6 | 177 | 95.6 | 60.0 | 36.2 | 0.379 |

Table. 6.1: Superconducting critical temperatures $T_c$ and the molecule model parameters $(t_1, t_2, t_3, t_4)$ in meV for $\kappa$-$(ET)_2X$ superconductors. All of the hopping integrals are from Ref. [100] and calculated by *ab initio* density-functional-theory calculations.

Second, we apply FLEX approximations to the eight Hubbard models. 4096 Matsubara frequencies and $16 \times 16$ $\boldsymbol{k}$-points are considered for the calculations. We investigate obtained spin susceptibility at $T = 40$ meV $= 464$ K, 10 meV $= 116$ K, 4 meV $= 46.4$ K and 1 meV $= 11.6$ K.

Third, we solve the linearized Eliashberg equations with four-point vertices and renormalized Green's functions within FLEX. The pairing interaction is symmetrized as

$$V(\boldsymbol{k}, \boldsymbol{k}') = \frac{1}{2}\left[V(\boldsymbol{k}, \boldsymbol{k}') + V(\boldsymbol{k}, -\boldsymbol{k}')\right] \tag{6.3}$$

with an assumption of spin-singlet superconductivity. Due to the enormous computational cost, calculations have been completed at, $T = 1$ meV $= 11.6$ K, with fewer frequencies and rough $\boldsymbol{k}$-mesh like 32 Matsubara frequencies and $16 \times 16$ $\boldsymbol{k}$-mesh.

## 6.3 Results — spin susceptibility —

$\chi^{\mathrm{s}}_{l_1 l_2; l_3 l_4}(\boldsymbol{q}, i\nu_n)$ are obtained as results of the FLEX calculations. We calculate

$$\chi^{\mathrm{s}}(\boldsymbol{q}) = \sum_{l,l'} e^{-i\boldsymbol{q}\cdot(\boldsymbol{t}_l - \boldsymbol{t}_{l'})} \chi^{\mathrm{s}}_{ll;l'l'}(\boldsymbol{q}, i\nu_0) \tag{6.4}$$

with considering the phase factor where $\boldsymbol{t}_l$ are positions of $l$th sites in the unit cell, and we plot them in Fig. 6.2, Fig. 6.3), Fig. 6.4) and Fig. 6.5) at $T = 40$ meV, 10 meV, 4 meV and 1 meV respectively.

Broad peaks of spin susceptibility at high temperature become sharper at lower temperature, which corresponds to an increase in spin susceptibility at low temperature. At low temperature, $T = 1$ meV $= 11.6$ K, main peaks are around $\boldsymbol{q}_0 = (\pm 2\pi, 0)$, $(0, \pm 2\pi)$ and $\boldsymbol{q}_1 = (0, \pm\frac{3}{4}\pi)$. In (5) and (7), additional peaks are around $\boldsymbol{q}_2 = (\frac{\pi}{2}, \pm\frac{\pi}{8})$ and $(-\frac{\pi}{2}, \pm\frac{\pi}{8})$. These additional spin susceptibility, $\chi^{\mathrm{s}}(\boldsymbol{q}_2)$, is understood with the strong in-plane anisotropy corresponding to the smaller $t_4/t_2$ as follows. The smaller $t_4/t_2$ makes the Fermi surface more one-dimensional. Therefore, a nesting, $\boldsymbol{q}_2$, between the sheet-like Fermi surfaces becomes better.

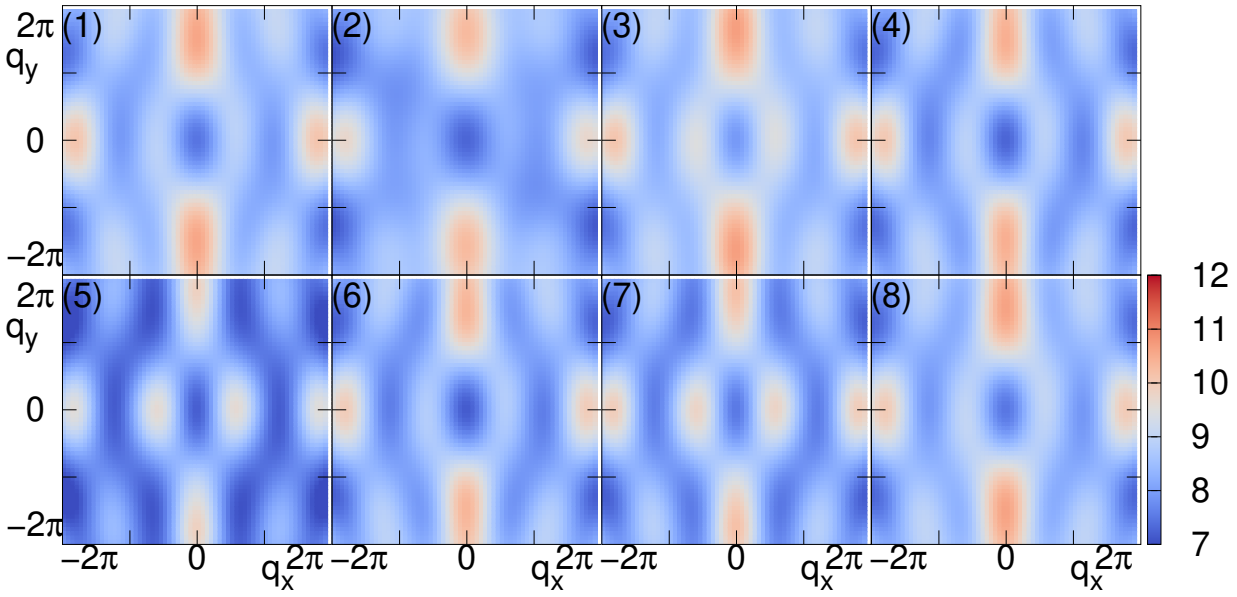


Fig.6.2: Spin susceptibility $\chi^{\mathrm{s}}(\boldsymbol{q})$ of $\kappa$-$(\mathrm{ET})_2X$ at $T = 40$ meV $= 464$ K. Indices from (1) to (8) correspond to the material indices in Table. 6.1.

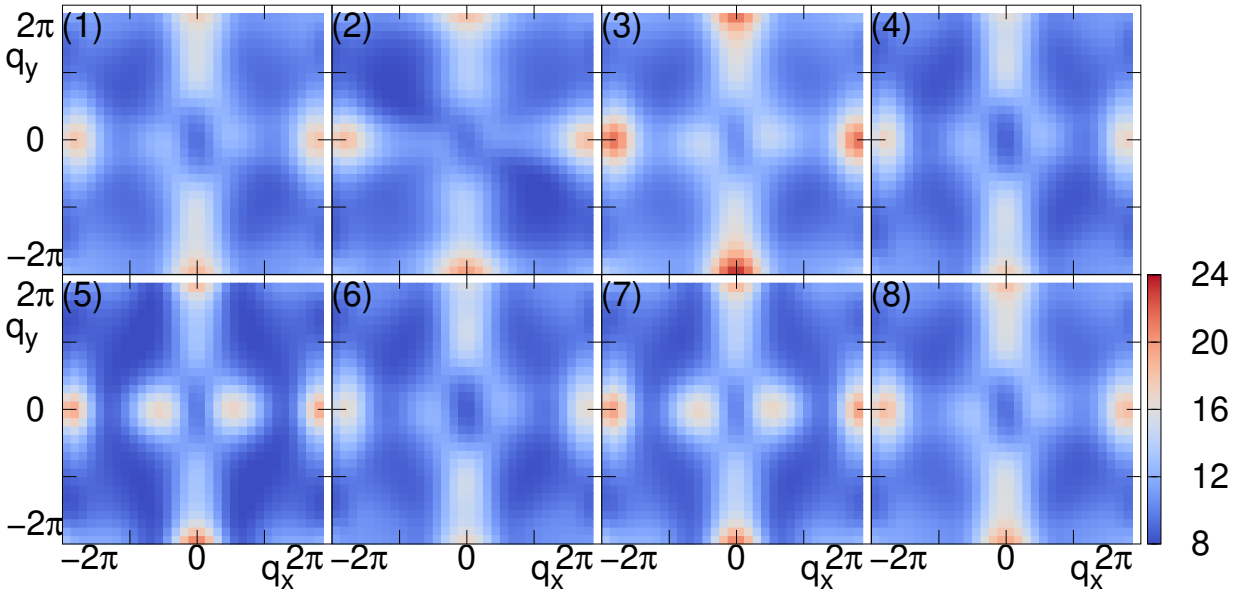


Fig.6.3: Spin susceptibility $\chi^{\mathrm{s}}(\boldsymbol{q})$ of $\kappa$-$(\mathrm{ET})_2X$ at $T = 10$ meV $= 116$ K. Indices from (1) to (8) correspond to the material indices in Table. 6.1.

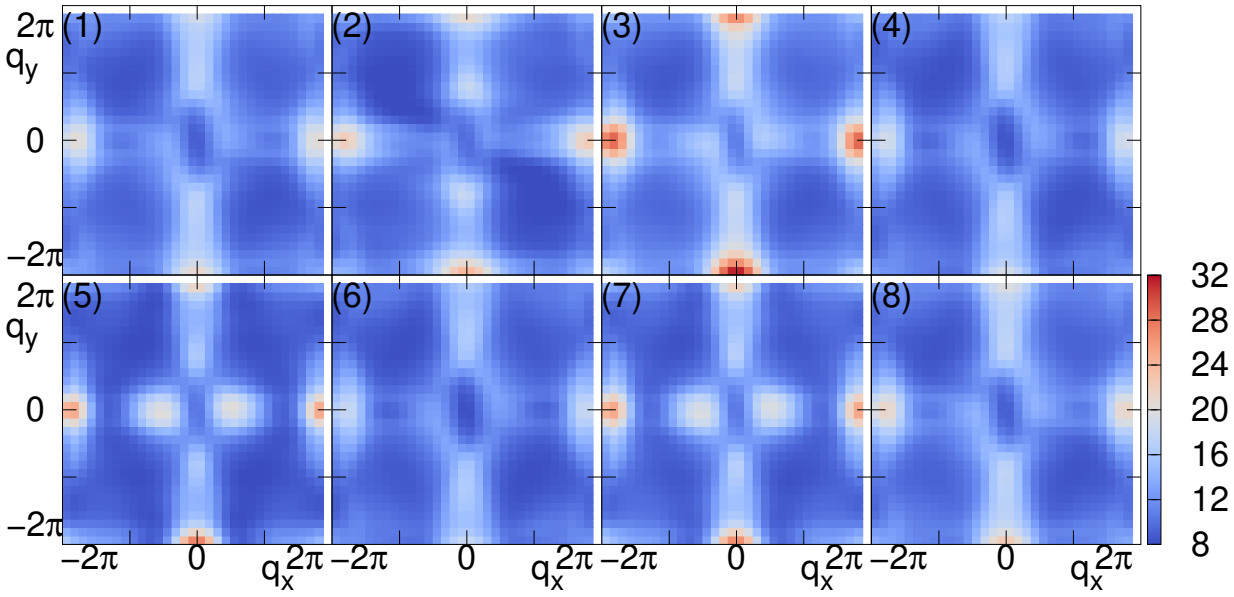


Fig.6.4: Spin susceptibility $\chi^{\mathrm{s}}(\boldsymbol{q})$ of $\kappa$-$(\mathrm{ET})_2X$ at $T = 4$ meV $= 46.4$ K. Indices from (1) to (8) correspond to the material indices in Table. 6.1.

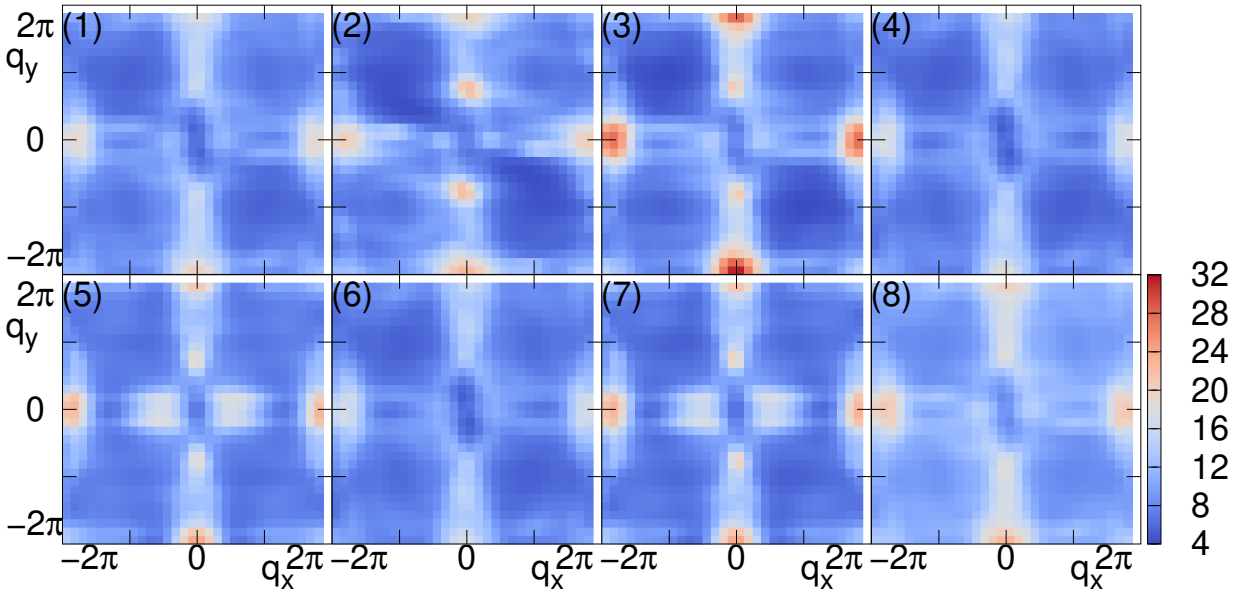


Fig.6.5: Spin susceptibility $\chi^{\mathrm{s}}(\boldsymbol{q})$ of $\kappa$-$(\mathrm{ET})_2X$ at $T = 1$ meV $= 11.6$ K. Indices from (1) to (8) correspond to the material indices in Table. 6.1.

## 6.4 Results — superconductivity —

We solve the linearized Eliashberg equation, and obtain eigenvalues $\lambda$ and corresponding eigenvectors $\Delta_{ll'}(\boldsymbol{k}, i\omega_n)$, which is the anomalous self-energy. Let us focus on the anomalous self-energy, $\Delta_{ll'}(\boldsymbol{k}, i\omega_0)$, at the lowest energy hereafter. Note that the anomalous self-energy, $\Delta_{ll'}$, is a $4 \times 4$ matrix since four-site models are considered. Symmetry of a gap function is discussed with the largest elements of the matrix.

First, we discuss the anomalous self-energy in (8) $\kappa$-Br. In the anomalous self-energy matrix, $\Delta_{ll'}$, of the first leading solution, an element of $(l, l') = (\mathrm{ET1}, \mathrm{ET3})$ is largest. The $(\mathrm{ET1}, \mathrm{ET3})$ element is also largest in the second leading solution. The imaginary parts of them are plotted in Fig. 6.6. In the first leading solution, the largest element, $\Delta_{\mathrm{ET1,ET3}}(\boldsymbol{k})$, shows no sign-changing, and its magnitude is smaller at $k_y = 0$. It is anisotropic fully gapped $s$-wave. On the other hand, the second leading solution, it shows sign-changing between the Fermi surfaces, $\alpha$ and $\beta$, like $d_{x^2-y^2}$-wave, but it is modulated from the exact $d_{x^2-y^2}$-wave. It is $s_\pm + d_{x^2-y^2}$-wave mentioned in Ref. [100].

The same tendency of the anisotropic fully gapped $s$-wave as the first leading solution and the $s_\pm + d_{x^2-y^2}$-wave as the second leading solution is obtained in other materials except (5) and (7). In the materials (5) and (7), the order of the leading solutions are reversed; the $s_\pm + d_{x^2-y^2}$-wave is the first leading, and the anisotropic fully gapped $s$-wave is the second leading.

The relation between obtained $\lambda$ and the actual $T_\mathrm{c}$ is plotted in Fig. 6.6 (c). As mentioned above, the $s_\pm + d_{x^2-y^2}$-wave is obtained as the leading solution in (5) and (7), and the anisotropic fully gapped $s$-wave is obtained in the other materials. Especially, with comparing (5) $\kappa$-NCS and (8) $\kappa$-Br where a number of experiments have been conducted, the $s_\pm + d_{x^2-y^2}$-wave is suggested in (5) $\kappa$-NCS, and the anisotropic fully gapped $s$-wave is suggested in (8) $\kappa$-Br. In fact, there is a recent study [97] of thermal-conductivity measurements, which clearly shows a difference between (5) $\kappa$-NCS and (8) $\kappa$-Br. Our results are in agreement with the experimental results where temperature dependences of the thermal conductivity suggest a full gap and a nodal gap in (5) $\kappa$-NCS and (8) $\kappa$-Br respectively.

In (4)-(8), the eigenvalues of the first leading solutions are in a narrow range of $0.094 \leq \lambda \leq 0.186$, which is in agreement with the similar $T_\mathrm{c}$ around a dozen Kelvin. On the other

hand, in (1)-(3) which are low-$T_c$ materials, the anisotropic fully gapped $s$-wave solutions are much more enhanced than the $s_{\pm} + d_{x^2-y^2}$-wave solutions. They are estimated to be larger than the first leading solutions in (4)-(8). It is natural to seem the $s$-wave solutions in the low-$T_c$ group overestimated with the following reasons. First, $\lambda$ of the $s$-wave solutions in the low-$T_c$ group deviate significantly from the true relation between $\lambda$ and $T_c$ drawn as a dashed line in Fig. 6.6 (c). Second, $d$-wave, not fully gapped $s$-wave, is suggested by a specific measurement in (3) [99]. With above reasons, it is possibly concluded that FLEX overestimates the $s$-wave solutions in the low-$T_c$ group.

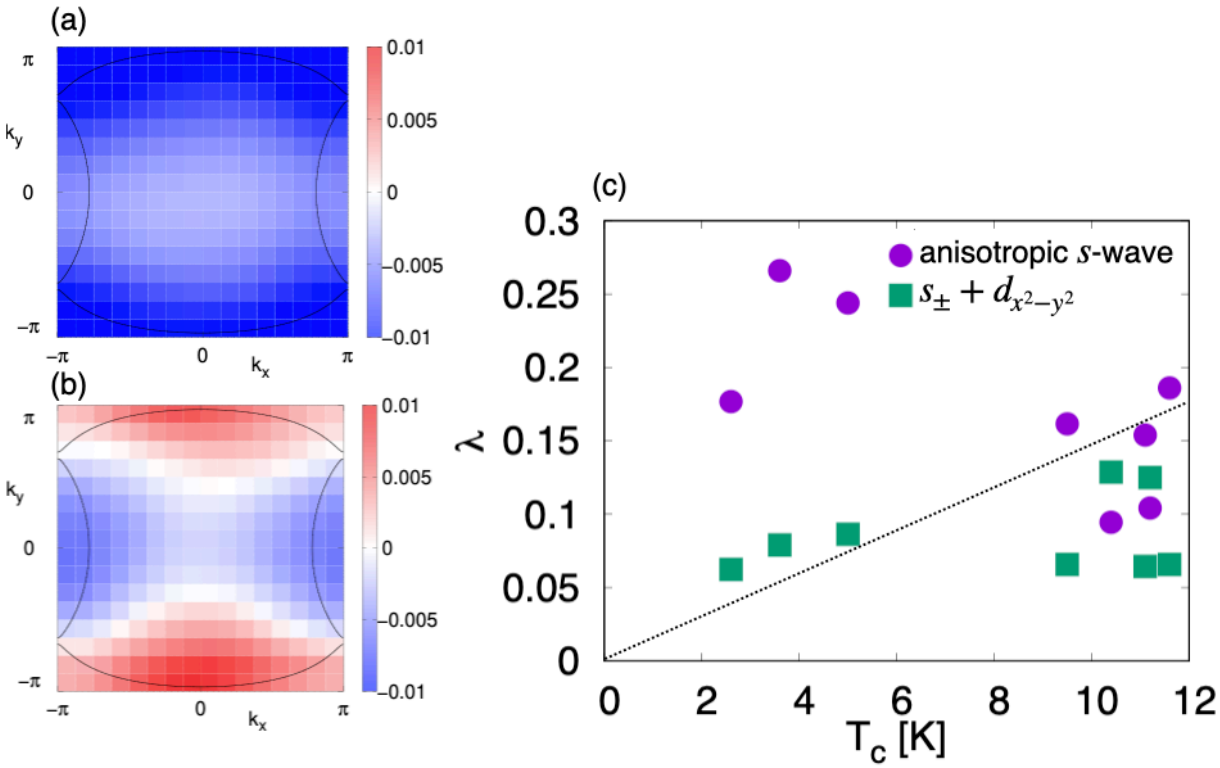


Fig.6.6: Left panels are imaginary parts of $\Delta_{\mathrm{ET1,ET3}}(\boldsymbol{k}, i\omega_0)$ of the (a) first and (b) second leading solutions with the eigenvalues $\lambda = 0.186$ and $\lambda = 0.066$ respectively in (8) $\kappa$-Br. Right panel is plots of obtained $\lambda$ against the actual $T_c$. Sixteen points are plotted since eight materials are considered, and two leading solutions (violet for the anisotropic fully gapped $s$-wave and green for the $s_{\pm} + d_{x^2-y^2}$-wave) are obtained in each of the materials.

## 6.5 Conclusions

Spin susceptibility is calculated within FLEX approximation, and the linearized Eliashberg equation is fully solved for every $\kappa$-$(ET)_2X$ ( $X$ = (1)$Ag(CF_3)_4(TCE)$, (2)$I_3$, (3)$Ag(CN)_2 \cdot H_2O$, (4)$\alpha_1'$-$(ET)_2Ag(CF_3)_4(TCE)$, (5)$(ET)_2Cu(NCS)_2$, (6)$\alpha_2'$-$(ET)_2Ag(CF_3)_4(TCE)$, (7)$(ET)_2Cu[N(CN)_2](CN)$ and (8)$(ET)_2Cu[N(CN)_2]Br$ ) which shows superconductivity at ambient pressure. We conclude an anisotropic fully gapped $s$-wave gap function in (8) $\kappa$-Br and a $s_\pm + d_{x^2-y^2}$-wave gap function in (5) $\kappa$-NCS, which are in agreement with the recent thermal-conductivity measurements [97]. The difference of gap function is understood by the in-plane anisotropy, $t_4/t_2$; the $s_\pm + d_{x^2-y^2}$-wave gap function is enhanced with a small $t_4/t_2$. Our results also suggest that the variation of $T_c$ among $\kappa$-$(ET)_2X$ is not understood within FLEX approximation since $\lambda$ of the anisotropic $s$-wave is overestimated in the low-$T_c$ group.

# Chapter 7

# Summary

We have studied the iron-based and organic superconductors using a combination of *ab initio* density functional theory (DFT) calculations and many body theory within the random phase approximation (RPA) and the fluctuation exchange (FLEX) approximation in this thesis. The original goal of understanding electronic phase diagrams in unconventional superconducting materials has been achieved for the heavily electron doped FeSe intercalate, $Li_x(C_3N_2H_{10})_{0.37}FeSe$ in Chapter 5 and the $\kappa$-type BEDT-TTF charge transfer salts in Chapter 6.

In Chapter 5, the doping effects on $Li_x(C_3N_2H_{10})_{0.37}FeSe$ have been studied using a combination of DFT calculations and RPA. We have shown that the dome in the superconducting transition temperature $T_c$ in the FeSe intercalate is understood by the spin fluctuation theory. Especially, we have shown that the enhancement of $T_c$ in the low doping side is explained by the enhancement of spin fluctuations and that the suppression of $T_c$ in the high doping side is explained by changing the spin fluctuation from stripe antiferromagnetic to bicollinear antiferromagnetic. In this chapter, the low and high doping sides have been analyzed from itinerant electron and localized moment perspectives respectively. This is a perfect demonstration of the fact that iron-based superconductivity can only be understood by fully accounting for itinerant and localized aspects of Fe $3d$ electrons.

In Chapter 6, variations of superconducting symmetry and $T_c$ in the family of $\kappa$-type BEDT-TTF charge transfer salts have been studied with FLEX calculations on specific models for the every superconducting materials in the family. We have shown the variation of the superconducting symmetry, anisotropic fully gapped $s$-wave and

$s_\pm + d_{x^2-y^2}$-wave, resulting from the in-plane anisotropy of the molecule models. Especially, our results suggesting gap functions like anisotropic fully gapped $s$-wave in $\kappa$-(BEDT-TTF)$_2$Cu[N(CN)$_2$]Br and $s_\pm + d_{x^2-y^2}$-wave in $\kappa$-(BEDT-TTF)$_{22}$Cu(NCS)$_2$ explains results of the recent thermal conductivity measurements. We have also suggested the necessity of factors not considered in the FLEX calculations for understanding the whole $T_\mathrm{c}$ tendency in the family.

As above, we have studied the FeSe intercalate and the family of $\kappa$-(BEDT-TTF) charge transfer salts based on DFT and spin fluctuation theory. We emphasize that the electronic structures calculated by the *ab initio* DFT calculations based on realistic crystal structures are necessary to understand the phase diagrams.

The effective models for the iron-based and organic superconductors have been multi-orbital and/or multi-site. We have created effective FLEX codes and analysis tools to deal with such models. They will help us when studying other materials and when developing other methods.

# Acknowledgments

First and foremost, I am extremely grateful to my supervisors, Prof. Harald O. Jeschke and Prof. Junya Otsuki for their invaluable advice, continuous support and patience during my PhD study.

I would like to thank Prof. Daniel Guterding for the excellent collaboration and his supports in developing codes.

I would like to express my gratitude to Prof. Igor I. Mazin, Prof. Seiichiro Onari and Prof. Nayuta Takemori for their great discussion.

I would like to express the deepest appreciation to Prof. Masanori Ichioka and Prof. Hiroto Adachi for their long-time teaching and supporting in the laboratory.

Finally, I thank the Japan Society for the Promotion of Science, as well as my family, for supporting my academic education. My PhD study was supported by JSPS Research Fellowship for Young Scientists.

# Appendix A

# Lattice with a basis

## A.1 Bravais lattice and reciprocal lattice with a basis

In general, crystal structure is represented with the following two concepts [*1]. First concept is the Bravais lattice, $\{\boldsymbol{R} : \boldsymbol{R} = n_1\boldsymbol{a}_1 + n_2\boldsymbol{a}_2 + n_3\boldsymbol{a}_3\}$, where $n_i$ are integers, and $\boldsymbol{a}_i$ are the primitive vectors. Second concept is the basis, which is how atoms, molecules, etc. located in the lattice.

Crystal structure is constructed by placing the basis periodically with the Bravais lattice. Here we consider a basis, which is constructed by sites located at $\boldsymbol{t}_l$ in the lattice. We call $l$ general orbitals, which includes electron orbitals, sites of atoms, and so on. Positions $\boldsymbol{r}_i$ of $i$th site in the crystal is expressed as

$$\boldsymbol{r}_i = \boldsymbol{R} + \boldsymbol{t}_l \tag{A.1}$$

where $\boldsymbol{R}$ is the lattice, which the $i$th site belongs to, and $\boldsymbol{t}_l$ is the position of the $l$th orbital. Note that the periodicity of crystal is expressed by the lattice $\{\boldsymbol{R}\}$.

Reciprocal lattice $\{\boldsymbol{K}\}$ of the Bravais lattice $\{\boldsymbol{R}\}$ is defined as a set of vectors $\boldsymbol{K}$ which satisfy

$$e^{i\boldsymbol{K}\cdot\boldsymbol{R}} = 1. \tag{A.2}$$

It is also possible to define the reciprocal lattice as a set of vectors $\boldsymbol{K} = m_1\boldsymbol{b}_1 + m_2\boldsymbol{b}_2 + m_3\boldsymbol{b}_3$ where $m_i$ are integers, and $\boldsymbol{b}_i$ are vectors which satisfy

$$\boldsymbol{a}_i \cdot \boldsymbol{b}_j = 2\pi\delta_{ij}. \tag{A.3}$$

[*1] See Chapter 4 of "Solid State Physics", N. W. Ashcroft and N. D. Mermin, for example.

The vectors $\boldsymbol{b}_i$ are called primitive reciprocal lattice vectors, which are

$$\begin{aligned}
\boldsymbol{b}_1 &= \frac{2\pi}{\boldsymbol{a}_1 \cdot (\boldsymbol{a}_2 \times \boldsymbol{a}_3)} \boldsymbol{a}_2 \times \boldsymbol{a}_3 \\
\boldsymbol{b}_2 &= \frac{2\pi}{\boldsymbol{a}_1 \cdot (\boldsymbol{a}_2 \times \boldsymbol{a}_3)} \boldsymbol{a}_3 \times \boldsymbol{a}_1. \\
\boldsymbol{b}_3 &= \frac{2\pi}{\boldsymbol{a}_1 \cdot (\boldsymbol{a}_2 \times \boldsymbol{a}_3)} \boldsymbol{a}_1 \times \boldsymbol{a}_2
\end{aligned} \tag{A.4}$$

We define the $k$-space as

$$\boldsymbol{k} = \begin{pmatrix} k_1 \\ k_2 \\ k_3 \end{pmatrix} = k_1 \boldsymbol{b}_1 + k_2 \boldsymbol{b}_2 + k_3 \boldsymbol{b}_3 \tag{A.5}$$

with the basis, $\boldsymbol{b}_1, \boldsymbol{b}_2, \boldsymbol{b}_3$.

## A.2 Correlation functions in lattice with a basis

In general, correlation functions $g(\boldsymbol{r}; \boldsymbol{r}')$ like electron Green's functions $G(\boldsymbol{r}; \boldsymbol{r}') = -\left\langle c(\boldsymbol{r}); c^\dagger(\boldsymbol{r}') \right\rangle$ and spin susceptibility $\chi^s(\boldsymbol{r}; \boldsymbol{r}') = \langle S^z(\boldsymbol{r}); S^z(\boldsymbol{r}') \rangle$ are discrete functions which connects between sites $\boldsymbol{r}$ and $\boldsymbol{r}'$. Here we assume homogeneous systems without fields and $g(\boldsymbol{r}; \boldsymbol{r}') = g(\boldsymbol{r} - \boldsymbol{r}')$. The Fourier transform of the correlation functions are

$$g(\boldsymbol{k}) = \frac{1}{N} \sum_{\boldsymbol{r}, \boldsymbol{r}'} e^{-i\boldsymbol{k} \cdot (\boldsymbol{r} - \boldsymbol{r})} g(\boldsymbol{r} - \boldsymbol{r}') \tag{A.6}$$

where we ommit $\tau$ or $i\omega_n$.

As the first example, we consider a one-dimensional one-site system, where a site located in a unit cell with the length of $a$. In this case, $r - r' = na$ for every combinatioins


of $(r, r')$. Therefore, the Fourier transform of $g(r - r')$ is

$$g(k) = \frac{1}{N} \sum_{n=-\infty}^{\infty} e^{-ikna} g(na). \tag{A.7}$$

This $g(k)$ has the period of $\frac{2\pi}{a}$ as following.

$$\begin{aligned} g\left(k+\frac{2\pi}{a}\right) &= \frac{1}{N}\sum_{n=-\infty}^{\infty} e^{-i\left(k+\frac{2\pi}{a}\right)na} g(na) \\ &= e^{-i2\pi}\frac{1}{N}\sum_{n=-\infty}^{\infty} e^{-ikna} g(na) \\ &= g(k) \end{aligned} \tag{A.8}$$

As the second example, we consider a one-dimensional two-site system, where the sites located at $t_1 = 0$ and $t_2 = a/3$.


In this system,

$$\begin{aligned} r - r' &= 0, \pm a, \pm 2a, \cdots, \frac{a}{3}, \frac{4a}{3}, \frac{7a}{3}, \cdots, \frac{-2a}{3}, \frac{-5a}{3}, \frac{-8a}{3}, \cdots \\ &= na, \left(n+\frac{1}{3}\right)a \end{aligned} \tag{A.9}$$

Therefore, the Fourier transform of $g(r-r')$ is

$$\begin{aligned} g(k) &= \frac{1}{N}\sum_{ij} e^{-ik(r-r')} g(r-r') \\ &= \frac{1}{N}\sum_{n=-\infty}^{\infty} e^{-ikna} g(na) + \frac{1}{N}\sum_{n=-\infty}^{\infty} e^{-ik\left(n+\frac{1}{3}\right)a} g\left(\left(n+\frac{1}{3}\right)a\right) \end{aligned} \tag{A.10}$$

With shift of $2\pi/a$, we obtain

$$\begin{aligned} g\left(k+\frac{2\pi}{a}\right) &= \frac{1}{N}\sum_{n=-\infty}^{\infty} e^{-i\left(k+\frac{2\pi}{a}\right)na} g(na) + \frac{1}{N}\sum_{n=-\infty}^{\infty} e^{-i\left(k+\frac{2\pi}{a}\right)\left(n+\frac{1}{3}\right)a} g\left(\left(n+\frac{1}{3}\right)a\right) \\ &= \frac{1}{N}\sum_{n=-\infty}^{\infty} e^{-i2\pi n} e^{-ikna} g(na) + \frac{1}{N}\sum_{n=-\infty}^{\infty} e^{-i2\pi n} e^{-i\frac{2\pi}{3}} e^{-ik\left(n+\frac{1}{3}\right)a} g\left(\left(n+\frac{1}{3}\right)a\right) \\ &= \frac{1}{N}\sum_{n=-\infty}^{\infty} e^{-ikna} g(na) + e^{-i\frac{2\pi}{3}}\frac{1}{N}\sum_{n=-\infty}^{\infty} e^{-ik\left(n+\frac{1}{3}\right)a} g\left(\left(n+\frac{1}{3}\right)a\right) \\ &\neq g(k) \end{aligned} \tag{A.11}$$

But

$$g\left(k+\frac{6\pi}{a}\right)=g(k), \tag{A.12}$$

which means that the period of $g(k)$ is $6\pi/a$. The phase factor because of the structure inside the unit cell enlarges the period of $g(k)$. In general, the period of $g(k)$ is infinity. Even if we classify the correlation functions like $g_{11}(\boldsymbol{r})$ which is correlation function between the first sites and $g_{12}(\boldsymbol{r})$ which is correlation function between the first and second sites, the period of $g_{12}(k)$ is $6\pi/a$.

To make the functions in $k$-space periodic, we express the site coordinate $\boldsymbol{r}$ with the Bravais lattice $\boldsymbol{R}$ and the basis (orbital or site indices) $\alpha$ as

$$g(\boldsymbol{r}-\boldsymbol{r'})=g_{\alpha\alpha'}(\boldsymbol{R};\boldsymbol{R'}) \tag{A.13}$$

where $\boldsymbol{r}=\boldsymbol{R}+\boldsymbol{t}_\alpha$ and $\boldsymbol{r'}=\boldsymbol{R'}+\boldsymbol{t}_{\alpha'}$. We make Fourier transform only for $\boldsymbol{R}-\boldsymbol{R'}$.

$$\begin{aligned}
g(\boldsymbol{k}) &= \frac{1}{N}\sum_{\boldsymbol{r},\boldsymbol{r'}} e^{-i\boldsymbol{k}\cdot(\boldsymbol{r}-\boldsymbol{r})} g(\boldsymbol{r}-\boldsymbol{r'}) \\
&= \frac{1}{N}\sum_{\boldsymbol{R},\boldsymbol{R'}}\sum_{\alpha,\alpha'} e^{-i\boldsymbol{k}\cdot(\boldsymbol{R}+\boldsymbol{t}_\alpha-\boldsymbol{R'}-\boldsymbol{t}_{\alpha'})} g_{\alpha\alpha'}(\boldsymbol{R}-\boldsymbol{R'}) \\
&= \sum_{\alpha,\alpha'} e^{-i\boldsymbol{k}\cdot(\boldsymbol{t}_\alpha-\boldsymbol{t}_{\alpha'})}\frac{1}{N}\sum_{\boldsymbol{R},\boldsymbol{R'}} e^{-i\boldsymbol{k}\cdot(\boldsymbol{R}-\boldsymbol{R'})} g_{\alpha\alpha'}(\boldsymbol{R}-\boldsymbol{R'}) \\
&= \sum_{\alpha,\alpha'} e^{-i\boldsymbol{k}\cdot(\boldsymbol{t}_\alpha-\boldsymbol{t}_{\alpha'})} g_{\alpha\alpha'}(\boldsymbol{k})
\end{aligned} \tag{A.14}$$

Then, $g_{\alpha\alpha'}(\boldsymbol{k})$ is always periodic with period of $\boldsymbol{K}=m_1\boldsymbol{b}_1+m_2\boldsymbol{b}_2+m_3\boldsymbol{b}_3$ because $\boldsymbol{R}-\boldsymbol{R'}=n_1\boldsymbol{a}_1+n_2\boldsymbol{a}_2+n_3\boldsymbol{a}_3$.

# Appendix B

# Green's functions

## B.1 Convolution theorem of Matsubara Green's functions

Fourier transform of

$$X(\boldsymbol{r}) = A(-\boldsymbol{r})B(\boldsymbol{r}) \tag{B.1}$$

is

$$\begin{aligned}
&X(\boldsymbol{q}) \\
&= \frac{1}{V}\int_V d\boldsymbol{r}^3 X(\boldsymbol{r}) \\
&= \frac{1}{V}\int_V d\boldsymbol{r}^3 A(-\boldsymbol{r})B(\boldsymbol{r}) \\
&= \frac{1}{V}\int_V d\boldsymbol{r}^3 \sum_{\boldsymbol{k}} e^{-i\boldsymbol{k}\cdot(-\boldsymbol{r})} A(\boldsymbol{k}) \sum_{\boldsymbol{k}'} e^{-i\boldsymbol{k}'\cdot\boldsymbol{r}} B(\boldsymbol{k}') \\
&= \sum_{\boldsymbol{k},\boldsymbol{k}'} A(\boldsymbol{k})B(\boldsymbol{k}') \underbrace{\frac{1}{V}\int_V d\boldsymbol{r}^3 e^{-i(\boldsymbol{k}'-\boldsymbol{k}-\boldsymbol{q})\cdot\boldsymbol{r}}}_{=\delta_{\boldsymbol{k}'-\boldsymbol{k}-\boldsymbol{q}}} \\
&= \sum_{\boldsymbol{k}} A(\boldsymbol{k})B(\boldsymbol{k}+\boldsymbol{q})
\end{aligned} \tag{B.2}$$

Convolution theorem is practical also in the Fourier transform between imaginary time and Matsubara frequency; Fourier transform of

$$X(\tau) = A(-\tau)B(\tau) \tag{B.3}$$

is

$$
\begin{aligned}
& X(i\nu_n) \\
&= \int_0^\beta e^{i\nu_n \tau} X(\tau) \\
&= \int_0^\beta e^{i\nu_n \tau} A(-\tau) B(\tau) \\
&= \int_0^\beta e^{i\nu_n \tau} \frac{1}{\beta} \sum_{m=-\infty}^{\infty} e^{-i\omega_m(-\tau)} A(i\omega_m) \frac{1}{\beta} \sum_{m'=-\infty}^{\infty} e^{-i\omega_{m'}\tau} B(i\omega_{m'}) \\
&= \frac{1}{\beta} \sum_{m=-\infty}^{\infty} \frac{1}{\beta} \sum_{m'=-\infty}^{\infty} A(i\omega_m) B(i\omega_{m'}) \underbrace{\int_0^\beta d\tau e^{-i(i\omega_{m'} - i\omega_m - i\nu_n)\tau}}_{=\beta\delta_{i\omega_{m'} - i\omega_m - i\nu_n}} \\
&= \frac{1}{\beta} \sum_{m=-\infty}^{\infty} A(i\omega_m) B(i\omega_m + i\nu_n)
\end{aligned}
\tag{B.4}
$$

# Bibliography


[1] H. K. Kamerlingh Onnes, Akad. Van Wetenschappen **14**, 113 (1911).

[2] W. B. Pearson and I. M. Templeton, "Superconducting transition of lead", Phys. Rev. **109**, 1094 (1958).

[3] J. Bardeen, L. N. Cooper, and J. R. Schrieffer, "Theory of Superconductivity", Phys. Rev. **108**, 1175 (1957).

[4] K. Takafumi, *Statistical Mechanics of Superconductivity (in Japanese)* (SAIENSU-SHA).

[5] H. Shiba, *Theory of Electrons in Solids (in Japanese)* (Morikita Publishing).

[6] Y. Kamihara, H. Hiramatsu, M. Hirano, R. Kawamura, H. Yanagi, T. Kamiya, and H. Hosono, "Iron-Based Layered Superconductor: LaOFeP", Journal of the American Chemical Society **128**, PMID: 16881620, 10012 (2006).

[7] Y. Kamihara, T. Watanabe, M. Hirano, and H. Hosono, "Iron-based layered superconductor La[$O_{1-x}F_x$]FeAs ($x$ =0.05-0.12) with $T_c$ = 26K", Journal of the American Chemical Society **130**, PMID: 18293989, 3296 (2008).

[8] I. Morozov, A. Boltalin, O. Volkova, A. Vasiliev, O. Kataeva, U. Stockert, M. Abdel-Hafiez, D. Bombor, A. Bachmann, L. Harnagea, M. Fuchs, H.-J. Grafe, G. Behr, R. Klingeler, S. Borisenko, C. Hess, S. Wurmehl, and B. Büchner, "Single Crystal Growth and Characterization of Superconducting LiFeAs", Crystal Growth & Design **10**, 4428 (2010).

[9] J. T. Greenfield, S. Kamali, K. Lee, and K. Kovnir, "A solution for solution-produced $\beta$-FeSe: elucidating and overcoming factors that prevent superconductivity", Chemistry of Materials **27**, 588 (2015).

[10] M. Tomić, H. O. Jeschke, and R. Valentí, "Unfolding of electronic structure through induced representations of space groups: Application to Fe-based superconductors", Phys. Rev. B **90**, Unfolding method, 195121 (2014).

[11] L. Boeri, O. V. Dolgov, and A. A. Golubov, "Is $LaFeAsO_{1-x}F_x$ an Electron-Phonon Superconductor?", Phys. Rev. Lett. **101**, 026403 (2008).

[12] I. I. Mazin, D. J. Singh, M. D. Johannes, and M. H. Du, "Unconventional Superconductivity with a Sign Reversal in the Order Parameter of $LaFeAsO_{1-x}F_x$", Phys. Rev. Lett. **101**, 057003 (2008).

[13] K. Kuroki, S. Onari, R. Arita, H. Usui, Y. Tanaka, H. Kontani, and H. Aoki, "Unconventional Pairing Originating from the Disconnected Fermi Surfaces of Superconducting $LaFeAsO_{1-x}F_x$", Phys. Rev. Lett. **101**, 087004 (2008).

[14] P. Hirschfeld, M. Korshunov, and I. Mazin, "Gap symmetry and structure of Fe-based superconductors", Reports on Progress in Physics **74**, 124508 (2011).

[15] P. A. Lee, N. Nagaosa, and X.-G. Wen, "Doping a Mott insulator: Physics of high-temperature superconductivity", Rev. Mod. Phys. **78**, 17 (2006).

[16] Q. Si and E. Abrahams, "Strong Correlations and Magnetic Frustration in the High $T_c$ Iron Pnictides", Phys. Rev. Lett. **101**, 076401 (2008).

[17] J. S. Davis and D.-H. Lee, "Concepts relating magnetic interactions, intertwined electronic orders, and strongly correlated superconductivity", Proceedings of the National Academy of Sciences **110**, 17623 (2013).

[18] K. Suzuki, H. Usui, S. Iimura, Y. Sato, S. Matsuishi, H. Hosono, and K. Kuroki, "Model of the Electronic Structure of Electron-Doped Iron-Based Superconductors: Evidence for Enhanced Spin Fluctuations by Diagonal Electron Hopping", Phys. Rev. Lett. **113**, 027002 (2014).

[19] D. Guterding, H. O. Jeschke, P. J. Hirschfeld, and R. Valentí, "Unified picture of the doping dependence of superconducting transition temperatures in alkali metal/ammonia intercalated FeSe", Phys. Rev. B **91**, 041112 (2015).

[20] M. Shimizu, N. Takemori, D. Guterding, and H. O. Jeschke, "Two-Dome Superconductivity in FeS Induced by a Lifshitz Transition", Phys. Rev. Lett. **121**, 137001 (2018).

[21] J. Hu and H. Ding, "Local antiferromagnetic exchange and collaborative Fermi surface as key ingredients of high temperature superconductors", Scientific reports **2**, 1 (2012).

[22] J. Glasbrenner, I. Mazin, H. O. Jeschke, P. Hirschfeld, R. Fernandes, and R. Valentí, "Effect of magnetic frustration on nematicity and superconductivity in iron chalcogenides", Nature Physics **11**, 953 (2015).

[23] D. Guterding, H. O. Jeschke, I. I. Mazin, J. K. Glasbrenner, E. Bascones, and R. Valentí, "Nontrivial role of interlayer cation states in iron-based superconductors", Phys. Rev. Lett. **118**, 017204 (2017).

[24] F.-C. Hsu, J.-Y. Luo, K.-W. Yeh, T.-K. Chen, T.-W. Huang, P. M. Wu, Y.-C. Lee, Y.-L. Huang, Y.-Y. Chu, D.-C. Yan, and M.-K. Wu, "Superconductivity in the PbO-type structure $\alpha$-FeSe", Proceedings of the National Academy of Sciences **105**, 14262 (2008).

[25] A. Böhmer, F. Hardy, F. Eilers, D. Ernst, P. Adelmann, P. Schweiss, T. Wolf, and C. Meingast, "Lack of coupling between superconductivity and orthorhombic distortion in stoichiometric single-crystalline FeSe", Physical Review B **87**, 180505 (2013).

[26] A. E. Böhmer and A. Kreisel, "Nematicity, magnetism and superconductivity in FeSe", Journal of Physics: Condensed Matter **30**, 023001 (2017).

[27] T. M. McQueen, A. J. Williams, P. W. Stephens, J. Tao, Y. Zhu, V. Ksenofontov, F. Casper, C. Felser, and R. J. Cava, "Tetragonal-to-Orthorhombic Structural Phase Transition at 90 K in the Superconductor $Fe_{1.01}Se$", Phys. Rev. Lett. **103**, 057002 (2009).

[28] A. I. Coldea and M. D. Watson, "The Key Ingredients of the Electronic Structure of FeSe", Annual Review of Condensed Matter Physics **9**, 125 (2018).

[29] M. Yi, H. Pfau, Y. Zhang, Y. He, H. Wu, T. Chen, Z. R. Ye, M. Hashimoto, R. Yu, Q. Si, D.-H. Lee, P. Dai, Z.-X. Shen, D. H. Lu, and R. J. Birgeneau, "Nematic Energy Scale and the Missing Electron Pocket in FeSe", Phys. Rev. X **9**, 041049 (2019).

[30] E. .-W. Scheidt, V. R. Hathwar, D. Schmitz, A. Dunbar, W. Scherer, F. Mayr, V. Tsurkan, J. Deisenhofer, and A. Loidl, "Superconductivity at $T_c$ = 44K in $Li_xFe_2Se_2(NH_3)_y$", The European Physical journal B **85**, 279 (2012).

[31] M. Burrard-Lucas, D. G. Free, S. J. Sedlmaier, J. D. Wright, S. J. Cassidy, Y. Hara, A. J. Corkett, T. Lancaster, P. J. Baker, S. J. Blundell, and S. J. Clarke, "Enhancement of the superconducting transition temperature of FeSe by intercalation of a molecular spacer layer", Nature Materials **12**, 15 (2013).

[32] S. J. Sedlmaier, S. J. Cassidy, R. G. Morris, M. Drakopoulos, C. Reinhard, S. J. Moorhouse, D. O' Hare, P. Manuel, D. Khalyavin, and S. J. Clarke, "Ammonia-Rich High-Temperature Superconducting Intercalates of Iron Selenide Revealed

through Time-Resolved in Situ X-ray and Neutron Diffraction", journal of the American Chemical Society **136**, PMID: 24354523, 630 (2014).

[33] P. Shahi, J. P. Sun, S. H. Wang, Y. Y. Jiao, K. Y. Chen, S. S. Sun, H. C. Lei, Y. Uwatoko, B. S. Wang, and J.-G. Cheng, "High-$T_c$ superconductivity up to 55 K under high pressure in a heavily electron doped $Li_{0.36}(NH_3)_yFe_2Se_2$ single crystal", Phys. Rev. B **97**, 020508 (2018).

[34] W. Bao, G. Li, Q. Huang, G. Chen, J. He, D. Wan, M. A. Green, Y. Qiu, J. Luo, and M. Wu, "Superconductivity Tuned by the Iron Vacancy Order in $K_xFe_{2-y}Se_2$", Chinese Physics Letters **30**, 027402 (2013).

[35] A. Krzton-Maziopa, V. Svitlyk, E. Pomjakushina, R. Puzniak, and K. Conder, "Superconductivity in alkali metal intercalated iron selenides", journal of Physics: Condensed Matter **28**, 293002 (2016).

[36] H. Sun, D. N. Woodruff, S. J. Cassidy, G. M. Allcroft, S. J. Sedlmaier, A. L. Thompson, P. A. Bingham, S. D. Forder, S. Cartenet, N. Mary, S. Ramos, F. R. Foronda, B. H. Williams, X. Li, S. J. Blundell, and S. J. Clarke, "Soft Chemical Control of Superconductivity in Lithium Iron Selenide Hydroxides $Li_{1-x}Fe_x(OH)Fe_{1-y}Se$", Inorganic Chemistry **54**, PMID: 25613347, 1958 (2015).

[37] X. F. Lu, N. Z. Wang, H. Wu, Y. P. Wu, D. Zhao, X. Z. Zeng, X. G. Luo, T. Wu, W. Bao, G. H. Zhang, F. Q. Huang, Q. Z. Huang, and X. H. Chen, "Coexistence of superconductivity and antiferromagnetism in $(Li_{0.8}Fe_{0.2})$OHFeSe", Nature Materials **14**, 325 (2015).

[38] T. Noji, T. Hatakeda, S. Hosono, T. Kawamata, M. Kato, and Y. Koike, "Synthesis and post-annealing effects of alkaline-metal-ethylenediamine-intercalated superconductors $A_x(C_2H_8N_2)_yFe_{2-z}Se_2$ ($A$ =Li, Na) with $T_c$ = 45K", Physica C: Superconductivity and its Applications **504**, 8 (2014).

[39] X. Zhou, C. Eckberg, B. Wilfong, S.-C. Liou, H. K. Vivanco, J. Paglione, and E. E. Rodriguez, "Superconductivity and magnetism in iron sulfides intercalated by metal hydroxides", Chem. Sci. **8**, 3781 (2017).

[40] L. Zheng, Y. Sakai, X. Miao, S. Nishiyama, T. Terao, R. Eguchi, H. Goto, and Y. Kubozono, "Superconductivity in $(NH_3)_yNa_xFeSe_{0.5}Te_{0.5}$", Phys. Rev. B **94**, 174505 (2016).

[41] C. Li, S. Sun, S. Wang, and H. Lei, "Enhanced superconductivity and anisotropy of $FeTe_{0.6}Se_{0.4}$ single crystals with Li-$NH_3$ intercalation", Phys. Rev. B **96**, 134503 (2017).

[42] S. Medvedev, T. M. McQueen, I. A. Troyan, T. Palasyuk, M. I. Eremets, R. J. Cava, S. Naghavi, F. Casper, V. Ksenofontov, G. Wortmann, and C. Felser, "Electronic and magnetic phase diagram of $\beta$-Fe1.01Se with superconductivity at 36.7 K under pressure", Nature Materials **8**, 630 (2009).

[43] S. Jin, X. Fan, X. Wu, R. Sun, H. Wu, Q. Huang, C. Shi, X. Xi, Z. Li, and X. Chen, "High-$T_c$ superconducting phases in organic molecular intercalated iron selenides: synthesis and crystal structures", Chem. Commun. **53**, 9729 (2017).

[44] T. Hatakeda, T. Noji, K. Sato, T. Kawamata, M. Kato, and Y. Koike, "New Alkali-Metal-and 2-Phenethylamine-Intercalated Superconductors $A_x(C_8H_{11}N)_yFe_{1-z}Se$ ($A$ = Li, Na) with the Largest Interlayer Spacings and $T_c \sim 40$K", Journal of the Physical Society of Japan **85**, 103702 (2016).

[45] R. J. Sun, Y. Quan, S. F. Jin, Q. Z. Huang, H. Wu, L. Zhao, L. Gu, Z. P. Yin, and X. L. Chen, "Realization of continuous electron doping in bulk iron selenides and identification of a new superconducting zone", Phys. Rev. B **98**, 214508 (2018).

[46] S. Hosono, T. Noji, T. Hatakeda, T. Kawamata, M. Kato, and Y. Koike, "New Intercalation Superconductor $Li_x(C_6H_{16}N_2)_yFe_{2-z}Se_2$ with a Very Large Interlayer-Spacing and $Tc = 38$K", journal of the Physical Society of Japan **83**, 113704 (2014).

[47] S. Hosono, T. Noji, T. Hatakeda, T. Kawamata, M. Kato, and Y. Koike, "New Superconducting Phase of $Li_x(C_6H_{16}N_2)_yFe_{2-z}Se_2$ with $T_c$ = 41K Obtained through the Post-Annealing", journal of the Physical Society of Japan **85**, 013702 (2016).

[48] L. Sun, X.-J. Chen, J. Guo, P. Gao, Q.-Z. Huang, H. Wang, M. Fang, X. Chen, G. Chen, Q. Wu, C. Zhang, D. Gu, X. Dong, L. Wang, K. Yang, A. Li, X. Dai, H.-k. Mao, and Z. Zhao, "Re-emerging superconductivity at 48 kelvin in iron chalcogenides", Nature **483**, 67 (2012).

[49] M. Izumi, L. Zheng, Y. Sakai, H. Goto, M. Sakata, Y. Nakamoto, H. L. T. Nguyen, T. Kagayama, K. Shimizu, S. Araki, T. C. Kobayashi, T. Kambe, D. Gu, J. Guo, J. Liu, Y. Li, L. Sun, K. Prassides, and Y. Kubozono, "Emergence of double-dome

superconductivity in ammoniated metal-doped FeSe", Scientific Reports **5**, 9477 (2015).

[50] C.-L. Song, H.-M. Zhang, Y. Zhong, X.-P. Hu, S.-H. Ji, L. Wang, K. He, X.-C. Ma, and Q.-K. Xue, "Observation of double-dome superconductivity in potassium-doped FeSe thin films", Physical review letters **116**, 157001 (2016).

[51] J. Zhang, F.-L. Liu, T.-P. Ying, N.-N. Li, Y. Xu, L.-P. He, X.-C. Hong, Y.-J. Yu, M.-X. Wang, J. Shen, W.-G. Yang, and S.-Y. Li, "Observation of two superconducting domes under pressure in tetragonal FeS", npj Quantum Materials **2**, 49 (2017).

[52] T. Qian, X.-P. Wang, W.-C. Jin, P. Zhang, P. Richard, G. Xu, X. Dai, Z. Fang, J.-G. Guo, X.-L. Chen, and H. Ding, "Absence of a Holelike Fermi Surface for the Iron-Based $K_{0.8}Fe_{1.7}Se_2$ Superconductor Revealed by Angle-Resolved Photoemission Spectroscopy", Phys. Rev. Lett. **106**, 187001 (2011).

[53] Y. Zhang, L. X. Yang, M. Xu, Z. R. Ye, F. Chen, C. He, H. C. Xu, J. Jiang, B. P. Xie, J. J. Ying, X. F. Wang, X. H. Chen, J. P. Hu, M. Matsunami, S. Kimura, and D. L. Feng, "Nodeless superconducting gap in $A_xFe_2Se_2$ ($A$ = K,Cs) revealed by angle-resolved photoemission spectroscopy", Nature Materials **10**, 273 (2011).

[54] F. Wang, F. Yang, M. Gao, Z.-Y. Lu, T. Xiang, and D.-H. Lee, "The electron pairing of $KxFe_{2-y}Se_2$", Europhysics Letters **93**, 57003 (2011).

[55] S. Nishioka, T. Kouchi, K. Suzuki, M. Yashima, H. Mukuda, M. Kodani, K. Mita, T. Kakuto, J.-H. Lee, T. Fujii, and T. Kambe, "Unconventional Superconductivity and Moderate Spin Fluctuations with Gap at Low Energies in Intercalated Iron Selenide Superconductor $Li_x(NH_3)_yFe_{2-\delta}Se_2$ Probed by $^{77}$Se NMR", Journal of the Physical Society of Japan **90**, 124709 (2021).

[56] X. Chen, S. Maiti, A. Linscheid, and P. J. Hirschfeld, "Electron pairing in the presence of incipient bands in iron-based superconductors", Phys. Rev. B **92**, 224514 (2015).

[57] Y. Bang, "Pairing mechanism of heavily electron doped FeSe systems: dynamical tuning of the pairing cutoff energy", New Journal of Physics **18**, 113054 (2016).

[58] T. A. Maier, V. Mishra, G. Balduzzi, and D. J. Scalapino, "Effective pairing interaction in a system with an incipient band", Phys. Rev. B **99**, 140504 (2019).

[59] Y. Yamakawa and H. Kontani, "Superconductivity without a hole pocket in electron-doped FeSe: Analysis beyond the Migdal-Eliashberg formalism", Phys. Rev. B **96**, 045130 (2017).

[60] Y. Yamakawa, S. Onari, and H. Kontani, "Doping effects on electronic states in electron-doped FeSe: Impact of self-energy and vertex corrections", Phys. Rev. B **102**, 081108 (2020).

[61] X. Lai, H. Zhang, Y. Wang, X. Wang, X. Zhang, J. Lin, and F. Huang, "Observation of superconductivity in tetragonal FeS", Journal of the American Chemical Society **137**, 10148 (2015).

[62] M. D. Watson, T. K. Kim, A. A. Haghighirad, S. F. Blake, N. R. Davies, M. Hoesch, T. Wolf, and A. I. Coldea, "Suppression of orbital ordering by chemical pressure in $FeSe_{1-x}S_x$", Phys. Rev. B **92**, 121108 (2015).

[63] H. Man, J. Guo, R. Zhang, R. Schönemann, Z. Yin, M. Fu, M. B. Stone, Q. Huang, Y. Song, W. Wang, et al., "Spin excitations and the Fermi surface of superconducting FeS", npj Quantum Materials **2**, 1 (2017).

[64] C. K. Borg, X. Zhou, C. Eckberg, D. J. Campbell, S. R. Saha, J. Paglione, and E. E. Rodriguez, "Strong anisotropy in nearly ideal tetrahedral superconducting FeS single crystals", Physical Review B **93**, 094522 (2016).

[65] S. Hosoi, K. Matsuura, K. Ishida, H. Wang, Y. Mizukami, T. Watashige, S. Kasahara, Y. Matsuda, and T. Shibauchi, "Nematic quantum critical point without magnetism in $FeSe_{1-x}S_x$ superconductors", Proceedings of the National Academy of Sciences **113**, 8139 (2016).

[66] K. Matsuura, Y. Mizukami, Y. Arai, Y. Sugimura, N. Maejima, A. Machida, T. Watanuki, T. Fukuda, T. Yajima, Z. Hiroi, et al., "Maximizing Tc by tuning nematicity and magnetism in $FeSe_{1-x}S_x$ superconductors", Nature communications **8**, 1 (2017).

[67] Y. Sato, S. Kasahara, T. Taniguchi, X. Xing, Y. Kasahara, Y. Tokiwa, Y. Yamakawa, H. Kontani, T. Shibauchi, and Y. Matsuda, "Abrupt change of the superconducting gap structure at the nematic critical point in $FeSe_{1-x}S_x$", Proceedings of the National Academy of Sciences **115**, 1227 (2018).

[68] T. Hanaguri, K. Iwaya, Y. Kohsaka, T. Machida, T. Watashige, S. Kasahara, T. Shibauchi, and Y. Matsuda, "Two distinct superconducting pairing states divided by the nematic end point in $FeSe_{1-x}S_x$", Science advances **4**, eaar6419 (2018).

[69] S. Kuhn, M. Kidder, D. Parker, C. dela Cruz, M. McGuire, W. Chance, L. Li, L. Debeer-Schmitt, J. Ermentrout, K. Littrell, M. Eskildsen, and A. Sefat, "Structure and property correlations in FeS", Physica C: Superconductivity and its Applications **534**, 29 (2017).

[70] X. Yang, Z. Du, G. Du, Q. Gu, H. Lin, D. Fang, H. Yang, X. Zhu, and H.-H. Wen, "Strong-coupling superconductivity revealed by scanning tunneling microscope in tetragonal FeS", Phys. Rev. B **94**, 024521 (2016).

[71] H. Lin, Y. Li, Q. Deng, J. Xing, J. Liu, X. Zhu, H. Yang, and H.-H. Wen, "Multiband superconductivity and large anisotropy in FeS crystals", Phys. Rev. B **93**, 144505 (2016).

[72] J. Xing, H. Lin, Y. Li, S. Li, X. Zhu, H. Yang, and H.-H. Wen, "Nodal superconducting gap in tetragonal FeS", Phys. Rev. B **93**, 104520 (2016).

[73] T. P. Ying, X. F. Lai, X. C. Hong, Y. Xu, L. P. He, J. Zhang, M. X. Wang, Y. J. Yu, F. Q. Huang, and S. Y. Li, "Nodal superconductivity in FeS: Evidence from quasiparticle heat transport", Phys. Rev. B **94**, 100504 (2016).

[74] S. Holenstein, U. Pachmayr, Z. Guguchia, S. Kamusella, R. Khasanov, A. Amato, C. Baines, H.-H. Klauss, E. Morenzoni, D. Johrendt, and H. Luetkens, "Coexistence of low-moment magnetism and superconductivity in tetragonal FeS and suppression of $T_c$ under pressure", Phys. Rev. B **93**, 140506 (2016).

[75] F. K. K. Kirschner, F. Lang, C. V. Topping, P. J. Baker, F. L. Pratt, S. E. Wright, D. N. Woodruff, S. J. Clarke, and S. J. Blundell, "Robustness of superconductivity to competing magnetic phases in tetragonal FeS", Phys. Rev. B **94**, 134509 (2016).

[76] X. Lai, Y. Liu, X. Lü, S. Zhang, K. Bu, C. Jin, H. Zhang, J. Lin, and F. Huang, "Suppression of superconductivity and structural phase transitions under pressure in tetragonal FeS", Scientific Reports **6**, 31077 (2016).

[77] T. Das and C. Panagopoulos, "Two types of superconducting domes in unconventional superconductors", New Journal of Physics **18**, 103033 (2016).

[78] H. Akamatsu, H. Inokuchi, and Y. Matsunaga, "Electrical Conductivity of the Perylene–Bromine Complex", Nature **173**, 168 (1954).

[79] D. Jérome, A. Mazaud, M. Ribault, and K. Bechgaard, "Superconductivity in a synthetic organic conductor $(TMTSF)_2PF_6$", Journal de Physique Lettres **41**, 95 (1980).

[80] H. Mayaffre, P. Wzietek, D. Jérome, C. Lenoir, and P. Batail, "Superconducting State of $\kappa$-$(ET)_2CU[N(CN)_2]$ Br Studied by $C^{13}$ NMR: Evidence for Vortex-Core-Induced Nuclear Relaxation and Unconventional Pairing", Phys. Rev. Lett. **75**, 4122 (1995).

[81] S. M. De Soto, C. P. Slichter, A. M. Kini, H. H. Wang, U. Geiser, and J. M. Williams, "$^{13}$C NMR studies of the normal and superconducting states of the organic superconductor $\kappa$-$(ET)_2Cu[N(CN)_2]Br$", Phys. Rev. B **52**, 10364 (1995).

[82] K. Kanoda, K. Miyagawa, A. Kawamoto, and Y. Nakazawa, "NMR relaxation rate in the superconducting state of the organic conductor $\kappa$-$(BEDT\text{-}TTF)_2Cu[N(CN)_2]Br$", Phys. Rev. B **54**, 76 (1996).

[83] K. Kanoda, "Electron correlation, metal-insulator transition and superconductivity in quasi-2D organic systems, $(ET)_2X$", Physica C: Superconductivity **282-287**, Materials and Mechanisms of Superconductivity High Temperature Superconductors V, 299 (1997).

[84] H. Kino and H. Fukuyama, "Phase Diagram of Two-Dimensional Organic Conductors:$(BEDT\text{-}TTF)_2X$", Journal of the Physical Society of Japan **65**, 2158 (1996).

[85] H. Kino and H. Kontani, "Phase diagram of superconductivity on the anisotropic triangular lattice hubbard model: An effective model of $\kappa$-(BEDT-TTF) salts", Journal of the Physical Society of Japan **67**, 3691 (1998).

[86] K. Kuroki and H. Aoki, "Superconductivity and spin correlation in organic conductors: A quantum Monte Carlo study", Phys. Rev. B **60**, 3060 (1999).

[87] J. M. Schrama, E. Rzepniewski, R. S. Edwards, J. Singleton, A. Ardavan, M. Kurmoo, and P. Day, "Millimeter-Wave Magneto-optical Determination of the Anisotropy of the Superconducting Order Parameter in the Molecular Superconductor $\kappa$-$(BEDT\text{-}TTF)_2Cu(NCS)_2$", Phys. Rev. Lett. **83**, 3041 (1999).

[88] S. Hill, N. Harrison, M. Mola, and J. Wosnitza, "Anisotropy of the Superconducting Order Parameter in $\kappa$-$(BEDT\text{-}TTF)_2Cu(NCS)_2$", Phys. Rev. Lett. **86**, 3451 (2001).

[89] T. Shibauchi, Y. Matsuda, M. B. Gaifullin, and T. Tamegai, "Comment on "Millimeter-Wave Magneto-optical Determination of the Anisotropy of the Superconducting Order Parameter in the Molecular Superconductor $\kappa$-$(BEDT\text{-}TTF)_2Cu(NCS)_2$"", Phys. Rev. Lett. **86**, 3452 (2001).

[90] T. Arai, K. Ichimura, K. Nomura, S. Takasaki, J. Yamada, S. Nakatsuji, and H. Anzai, "Tunneling spectroscopy on the organic superconductor $\kappa$-(BEDT-TTF)$_2$Cu(NCS)$_2$ using STM", Phys. Rev. B **63**, 104518 (2001).

[91] K. Izawa, H. Yamaguchi, T. Sasaki, and Y. Matsuda, "Superconducting Gap Structure of $\kappa$-(BEDT-TTF)$_2$Cu(NCS)$_2$ Probed by Thermal Conductivity Tensor", Phys. Rev. Lett. **88**, 027002 (2001).

[92] K. Kuroki, T. Kimura, R. Arita, Y. Tanaka, and Y. Matsuda, "$d_{x^2-y^2}$- versus $d_{\mathrm{xy}}$-like pairings in organic superconductors $\kappa - (\mathrm{BEDT} - \mathrm{TTF})_2X$", Phys. Rev. B **65**, 100516 (2002).

[93] H. Elsinger, J. Wosnitza, S. Wanka, J. Hagel, D. Schweitzer, and W. Strunz, "$\kappa$-(BEDT)-TTF)$_2$Cu[N(CN)$_2$]Br: A Fully Gapped Strong-Coupling Superconductor", Phys. Rev. Lett. **84**, 6098 (2000).

[94] A. E. Kovalev, T. Ishiguro, J. Yamada, S. Takasaki, and H. Anzai, "The anisotropic low-temperature specific heat of organic superconductor $\kappa$-(BEDT-TTF)$_2$Cu(NCS)$_2$ in magnetic field", Journal of Experimental and Theoretical Physics **92**, 1035 (2001).

[95] J. Müller, M. Lang, R. Helfrich, F. Steglich, and T. Sasaki, "High-resolution ac-calorimetry studies of the quasi-two-dimensional organic superconductor $\kappa$-(BEDT-TTF)$_2$Cu(NCS)$_2$", Phys. Rev. B **65**, 140509 (2002).

[96] J. Wosnitza, S. Wanka, J. Hagel, M. Reibelt, D. Schweitzer, and J. Schlueter, "Thermodynamic properties of quasi-two-dimensional organic superconductors", Synthetic Metals **133-134**, Proceedings of the Yamada Conference LVI. The Fourth International Symposium on Crystalline Organic Metals, Superconductors and Ferromagnets (ISCOM 2001)., 201 (2003).

[97] S. Kühlmorgen, R. Schönemann, E. L. Green, J. Müller, and J. Wosnitza, "Investigation of the superconducting gap structure in $\kappa$-(BEDT-TTF)$_2$Cu(NCS)$_2$ and $\kappa$-(BEDT-TTF)$_2$Cu[N(CN)$_2$]Br by means of thermal-conductivity measurements", Journal of Physics: Condensed Matter **29**, 405604 (2017).

[98] D. Guterding, S. Diehl, M. Altmeyer, T. Methfessel, U. Tutsch, H. Schubert, M. Lang, J. Müller, M. Huth, H. O. Jeschke, R. Valentí, M. Jourdan, and H.-J. Elmers, "Evidence for Eight-Node Mixed-Symmetry Superconductivity in a Correlated Organic Metal", Phys. Rev. Lett. **116**, 237001 (2016).

[99] S. Imajo, K. Kindo, and Y. Nakazawa, "Symmetry change of $d$-wave superconductivity in $\kappa$-type organic superconductors", Phys. Rev. B **103**, L060508 (2021).

[100] D. Guterding, M. Altmeyer, H. O. Jeschke, and R. Valentí, "Near-degeneracy of extended $s + d_{x^2-y^2}$ and $d_{xy}$ order parameters in quasi-two-dimensional organic superconductors", Phys. Rev. B **94**, 024515 (2016).

[101] R. Kato, H. Kobayashi, A. Kobayashi, S. Moriyama, Y. Nishio, K. Kajita, and W. Sasaki, "A new ambient-pressure superconductor, $\kappa$-(BEDT-TTF)$_2$I$_3$", Chemistry Letters **16**, 507 (1987).

[102] H. Mori, I. Hirabayashi, S. Tanaka, T. Mori, and H. Inokuchi, "A new ambient-pressure organic superonductor, $\kappa$-(BEDT-TTF)$_2$Ag(CN)$_2$H$_2$O($T_c$ = 5.0K)", Solid state communications **76**, 35 (1990).

[103] A. M. Kini, U. Geiser, H. H. Wang, K. D. Carlson, J. M. Williams, W. K. Kwok, K. G. Vandervoort, J. E. Thompson, and D. L. a. Stupka, "A new ambient-pressure organic superconductor, .kappa.-(ET)$_2$Cu[N(CN)$_2$]Br, with the highest transition temperature yet observed (inductive onset $T_c$ = 11.6 K, resistive onset = 12.5 K)", Inorganic Chemistry **29**, 2555 (1990).

[104] T. Matsubara, "A New Approach to Quantum-Statistical Mechanics", Progress of Theoretical Physics **14**, 351 (1955).

[105] A. A. Abrikosov, L. P. Gor'kov, and I. E. Dzyaloshinskii, "ON APPLICATION OF QUANTUM FIELD THEORY METHODS TO PROBLEMS OF QUANTUM STATISTICS AT FINITE TEMPERATURES", Zhur. Eksptl'. i Teoret. Fiz. **Vol: 36** (1959).

[106] F. J. Dyson, "The $S$ Matrix in Quantum Electrodynamics", Phys. Rev. **75**, 1736 (1949).

[107] R. Kubo, "Statistical-Mechanical Theory of Irreversible Processes. I. General Theory and Simple Applications to Magnetic and Conduction Problems", Journal of the Physical Society of Japan **12**, 570 (1957).

[108] D. Bohm and D. Pines, "A Collective Description of Electron Interactions. I. Magnetic Interactions", Phys. Rev. **82**, 625 (1951).

[109] D. Pines and D. Bohm, "A Collective Description of Electron Interactions: II. Collective vs Individual Particle Aspects of the Interactions", Phys. Rev. **85**, 338 (1952).

[110] D. Bohm and D. Pines, "A Collective Description of Electron Interactions: III. Coulomb Interactions in a Degenerate Electron Gas", Phys. Rev. **92**, 609 (1953).

[111] M. Gell-Mann and K. A. Brueckner, "Correlation Energy of an Electron Gas at High Density", Phys. Rev. **106**, 364 (1957).

[112] K. Kubo, "Pairing symmetry in a two-orbital hubbard model on a square lattice", Phys. Rev. B Condens. Matter **75**, 224509 (2007).

[113] H. Ikeda, R. Arita, and J. Kuneš, "Phase diagram and gap anisotropy in iron-pnictide superconductors", Phys. Rev. B Condens. Matter **81**, 054502 (2010).

[114] N. E. Bickers, D. J. Scalapino, and S. R. White, "Conserving Approximations for Strongly Correlated Electron Systems: Bethe-Salpeter Equation and Dynamics for the Two-Dimensional Hubbard Model", Phys. Rev. Lett. **62**, 961 (1989).

[115] K. Miyake, S. Schmitt-Rink, and C. M. Varma, "Spin-fluctuation-mediated even-parity pairing in heavy-fermion superconductors", Phys. Rev. B **34**, 6554 (1986).

[116] G. Baym and L. P. Kadanoff, "Conservation Laws and Correlation Functions", Phys. Rev. **124**, 287 (1961).

[117] G. Baym, "Self-Consistent Approximations in Many-Body Systems", Phys. Rev. **127**, 1391 (1962).

[118] L. P. Gor' kov, "Microscopic derivation of the Ginzburg-Landau equations in the theory of superconductivity", Sov. Phys. JETP **9**, 1364 (1959).

[119] G. Eliashberg, "Interactions between electrons and lattice vibrations in a superconductor", Sov. Phys. JETP **11**, 696 (1960).

[120] T. P. Ying, X. L. Chen, G. Wang, S. F. Jin, T. T. Zhou, X. F. Lai, H. Zhang, and W. Y. Wang, "Observation of superconductivity at 30–46K in $A_xFe_2Se_2$ ($A$ = Li, Na, Ba, Sr, Ca, Yb and Eu)", Scientific Reports **2**, 426 (2012).

[121] K. Koepernik and H. Eschrig, "Full-potential nonorthogonal local-orbital minimum-basis band-structure scheme", Phys. Rev. B **59**, FPLO paper, 1743 (1999).

[122] J. P. Perdew, K. Burke, and M. Ernzerhof, "Generalized gradient approximation made simple", Phys. Rev. Lett. **77**, GGA paper, 3865 (1996).

[123] H. Eschrig and K. Koepernik, "Tight-binding models for the iron-based superconductors", Phys. Rev. B **80**, How to make tight-binding models for the iron-based superconductors, 104503 (2009).

[124] S. Graser, T. Maier, P. Hirschfeld, and D. Scalapino, "Near-degeneracy of several pairing channels in multiorbital models for the Fe pnictides", New Journal of Physics **11**, Eigenvalue problem for a dimensionless pairing strength functional instead of linearized Eliashberg equation, 025016 (2009).

[125] D. Guterding, "Microscopic modelling of organic and iron-based superconductors", PhD thesis (Goethe-Universität Frankfurt am Main (Germany), 2017).

[126] I. I. Mazin, M. Shimizu, N. Takemori, and H. O. Jeschke, "Novel Fe-Based Superconductor $LaFe_2As_2$ in Comparison with Traditional Pnictides", Phys. Rev. Lett. **123**, 267001 (2019).

[127] L. Zhao, A. Liang, D. Yuan, Y. Hu, D. Liu, J. Huang, S. He, B. Shen, Y. Xu, X. Liu, et al., "Common electronic origin of superconductivity in (Li,Fe)OHFeSe bulk superconductor and single-layer FeSe/$SrTiO_3$ films", Nature communications **7**, 1 (2016).

[128] X. Shi, Z. Han, X. Peng, P. Richard, T. Qian, X. Wu, M. Qiu, S. Wang, J. Hu, Y. Sun, et al., "Enhanced superconductivity accompanying a Lifshitz transition in electron-doped FeSe monolayer", Nature communications **8**, 1 (2017).

[129] X. Wu, S. Qin, Y. Liang, H. Fan, and J. Hu, "Topological characters in $Fe(Te_{1-x}Se_x)$ thin films", Phys. Rev. B **93**, 115129 (2016).

[130] G. Xu, B. Lian, P. Tang, X.-L. Qi, and S.-C. Zhang, "Topological superconductivity on the surface of fe-based superconductors", Phys. Rev. Lett. **117**, 047001 (2016).

[131] P. Zhang, K. Yaji, T. Hashimoto, Y. Ota, T. Kondo, K. Okazaki, Z. Wang, J. Wen, G. Gu, H. Ding, et al., "Observation of topological superconductivity on the surface of an iron-based superconductor", Science **360**, 182 (2018).

[132] D. Wang, L. Kong, P. Fan, H. Chen, S. Zhu, W. Liu, L. Cao, Y. Sun, S. Du, J. Schneeloch, et al., "Evidence for Majorana bound states in an iron-based superconductor", Science **362**, 333 (2018).

[133] N. Katayama, S. Ji, D. Louca, S. Lee, M. Fujita, T. J. Sato, J. Wen, Z. Xu, G. Gu, G. Xu, Z. Lin, M. Enoki, S. Chang, K. Yamada, and J. M. Tranquada, "Investigation of the Spin-Glass Regime between the Antiferromagnetic and Superconducting Phases in $Fe_{1+y}Se_xTe_{1-x}$", Journal of the Physical Society of Japan **79**, 113702 (2010).

[134] Y. Nakazawa and K. Kanoda, "Low-temperature specific heat of $\kappa$-(BEDT-TTF)$_2$Cu[N(CN)$_2$]Br in the superconducting state", Phys. Rev. B **55**, R8670 (1997).

[135] S. Belin, K. Behnia, and A. Deluzet, "Heat Conduction in $\kappa$-(BEDT-TTF)$_2$Cu(NCS)$_2$", Phys. Rev. Lett. **81**, 4728 (1998).

[136] L. P. Le, G. M. Luke, B. J. Sternlieb, W. D. Wu, Y. J. Uemura, J. H. Brewer, T. M. Riseman, C. E. Stronach, G. Saito, H. Yamochi, H. H. Wang, A. M. Kini, K. D. Carlson, and J. M. Williams, "Muon-spin-relaxation measurements of magnetic penetration depth in organic superconductors (BEDT-TTF)$_2$-$X$: $X$=Cu(NCS)$_2$ and Cu[N(CN)$_2$]Br", Phys. Rev. Lett. **68**, 1923 (1992).